Shanghai Jiao Tong University
University of Michigan - Shanghai Jiao Tong University Joint Institute

---

Particle-in-cell/Monte Carlo simulation of single- and dual-frequency capacitively coupled chlorine discharges

by

Shuo Huang

A thesis submitted in partial fulfillment of the
requirements for the degree of Master of Engineering in
Electronics Science and Technology at Shanghai Jiao Tong University

---

Committee in charge:
Professor Jon Tomas Gudmundsson, Chair
Professor Yaping Dan
Professor Hua Bao

Shanghai
March, 2014

Abstract

Chlorine is widely used in plasma etching of both semiconductors and metals. In this study, we first demonstrate the oopd1 (object oriented plasma device for one dimension) particle-in-cell/Monte Carlo simulation tool for the capacitively coupled chlorine discharge with a comprehensive reaction set. Then we use this code to explore typical capacitively coupled chlorine discharges. Actually, we apply a hybrid approach consisting of a particle-in-cell/Monte Carlo simulation and a volume averaged global model. The simulation results are compared with available experimental measurements and good agreement is achieved. We explore typical single-frequency capacitively coupled chlorine discharges driven by a voltage source and a current source, respectively. The effect of gas pressure, driving current, driving frequency and secondary electrons on the discharge is systematically investigated. The feedstock gas pressure is varied from 5 to 100 mTorr, the driving current is varied from 20 to 80 A/m^2, the driving frequency is varied from 13.56 to 60 MHz and the secondary electron emission coefficient is varied from 0.0 to 0.4. Key plasma parameters including the particle density, the electron heating rate, the effective electron temperature, the electron energy probability function, the ion energy distribution (IED) and ion angular distribution (IAD) of both Cl^+ and Cl_2^+ ions are explored and their variations with control parameters are analyzed and compared with other discharges. Furthermore, we extend our study to dual-frequency capacitively coupled chlorine discharge by adding a low-frequency current source and explore the effect of the low-frequency source on the discharge. The low-frequency current density is increased from 0 to 4 A/m^2. The effect of secondary electron emission in the dual-frequency discharge is also explored. In addition, the IEDs and IADs of Cl_2^+ and Cl^+ ions in the dual-frequency capacitively coupled chlorine discharge are explored in detail due to their significance in materials processing at the surface.

上海交通大学

交大密西根学院

基于质点网格/蒙特卡洛算法的单频与双频电容耦合氯气放电分析

黄朔

上海交通大学密西根学院硕士学位论文

电子科学与技术专业

委员会成员：

Jon Tomas Gudmundsson（主席）

但亚平

鲍华

上海

2014 年 **3** 月

上海交通大学

学位论文原创性声明

本人郑重声明：所呈交的学位论文，是本人在导师的指导下，独立进行研究工作所取得的成果。除文中已经注明引用的内容外，本论文不包含任何其他个人或集体已经发表或撰写过的作品成果。对本文的研究做出重要贡献的个人和集体，均已在文中以明确方式标明。本人完全意识到本声明的法律结果由本人承担。

学位论文作者签名：黄朔

日期：2014 年 3 月 1 日

上海交通大学

学位论文版权使用授权书

本学位论文作者完全了解学校有关保留、使用学位论文的规定，同意学校保留并向国家有关部门或机构送交论文的复印件和电子版，允许论文被查阅和借阅。本人授权上海交通大学可以将本学位论文的全部或部分内容编入有关数据库进行检索，可以采用影印、缩印或扫描等复制手段保存和汇编本学位论文。

保密□，在___年解密后适用本授权书。

本学位论文属于

不保密☑。

（请在以上方框内打“√”）

学位论文作者签名：黄朔　　指导教师签名：Jón Tómas Guðmundsson

日期：2014年3月1日　　日期：2014年3月1日

摘要

氯气放电被广泛应用于刻蚀半导体和金属材料。在本课题中，我们首先开发并验证了针对电容耦合氯气放电的一维仿真程序 oopd1。该仿真程序基于质点网格/蒙特卡洛算法，并且包含了目前为止最为全面的反应组及相关碰撞截面参数。然后，该程序被用于研究典型的电容耦合氯气放电。准确地说，我们在这里采用了一种混合方法来研究氯气放电，该混合方法包括本研究中开发的质点网格/蒙特卡洛仿真程序以及之前已经开发的氯气放电全局模型程序。我们对单频放电和双频放电两种模式都进行了较为系统地研究。在研究单频放电时，我们对两种驱动方式（电流驱动和电压驱动）都进行了研究。我们重点研究了控制参数，包括气体气压、驱动电流、电源频率和二次电子发射系数等，对放电的影响。气体气压的变化范围为 5 到 100 mTorr，驱动电流的变化范围为 20 到 80 A/m^2, 电源频率的变化范围为 13.56 到 60 MHz，二次电子发射系数的变化范围为 0.0 到 0.4。我们对放电的关键参数，包括离子浓度、电子加热速率、等效电子温度、电子能量概率函数、Cl_2^+和 Cl^+离子的离子能量分布（IED）和离子角分布（IAD）等，随控制参数的变化进行了详细地研究。在研究单频放电的基础上，我们通过增加一个低频电源从而使单频放电模式变为复杂的双频放电模式。低频电流的变化范围为 0 到 4 A/m^2。我们发现二次电子发射在双频放电中产生的影响要大于在单频放电中产生的影响。由于离子的 IEDs 和 IADs 在材料处理过程中非常重要，我们对双频放电中 Cl_2^+和 Cl^+离子的 IEDs 和 IADs 进行了深入分析。

Acknowledgements

First, I would like to thank my advisor, Professor Jon Tomas Gudmundsson. He introduced this interesting and important project to me. Frankly speaking, it has practised my research ability and attracted me to the field of engineering. To me, my advisor is a constant source of knowledge and his endless passion and interest on investigations always inspire me to move forward. I still remember the words he told me in the first semester I came that life is to explore the uncertainties. After two and a half years' study, I become more and more convinced by his words of wisdom, which can be applicable in both my study and my life. Apart from this, I have always been benefiting from his teaching method. He let me begin writing proposal and analyzing data from the first semester of my graduate study. Furthermore, he constantly spent time revising my drafts again and again in great detail. Owing to his guidance and instruction, I gradually change from somewhat a "garbage maker" to someone who can really write and publish something. The time I have spent here being his student is such a huge treasure for me. I will always keep his invaluable advice that "aim high and be proud of yourself" in my mind. I will faithfully head forward and explore more uncertainties in both the scientific world and my life in the future.

Second, I would like to thank my thesis committee members, Professors Yaping Dan and Hua Bao. They taught me courses on Electronic and Optical Properties of Semiconductors and Solid State Physics for Engineering, respectively. These two courses are highly related to my study and have equipped me with a better understanding of the electrical devices from the microscopic view. Also, they shared with me their memorable experience when they were in America and wrote recommendation letters for me to provide their strong support when I applied for the Ph.D. programs in American universities. With their support and expectations, I wish that one day I can follow their steps and also gain fantastic experience in my Ph.D. study.

Third, I would like to thank Wen-Cong Chen (Tsinghua University), Trevor Lafleur (Ecole Polytechnique) and Professors John P. Verboncoeur (Michigan State University), Michael A. Lieberman (UC Berkeley) and Allan J. Lichtenberg (UC Berkeley). Although I have never

met anyone of them, I have received helpful and instructive emails from them answering my questions about my study. Dr. Chen has pointed out my mistake in estimating the cross section for fragmentation reaction. Dr. Lafleur has explained the effect of secondary electrons on the effective electron temperature and the ion flux in the discharge to me. Professors Verboncoeur, Lieberman and Lichtenberg have explained the algorithm and structure of the oopd1 code to me and taught me how the reference frame is chosen in the code and how to inherit proper features from the trunk files of the code. Moreover, Professor Lieberman has double checked the code I wrote and made sure that every programming sentence and every numerical value I wrote in the code are right and reasonable. I gratefully acknowledge their generous help.

Last but not least, I would like to thank my parents. They are always cultivating me to be with a positive and optimistic view of the world. They are always reminding me to be of confidence, patience and humility. They are always supporting me and sharing my laughs and tears.... All in all, I cannot be more grateful to them. They are my priceless treasure and I will always be proud of them.

This study was partially supported by the Icelandic Research Fund Grant No. 130029-051.

Contents

Chapter 1

Introduction

The electronegative molecular chlorine discharge is widely used in plasma etching of semiconductors and metals (Flamm, 1990). More recently, chlorine-containing plasmas have been found to achieve selective etching of high-k materials over silicon-based substrates (Bodart et al., 2012) and TiN over TaN and vice versa (Shin et al., 2013). The application of chlorine plasmas in manufacturing integrated circuits has been comprehensively reviewed recently by Donnelly and Kornblit (2013). The quality of etching such as etch rate, selectivity and anisotropy is highly dependent on the relative fluxes of Cl_2, Cl, Cl_2^+ and Cl^+ particles to the substrate. Among these species, Cl atoms, mainly created by electron impact dissociation of Cl_2 molecules, are generally considered to be the primary reactant in plasma etching with the etch yield for Cl atoms two to three times higher than for Cl_2 molecules for high neutral-to-ion flux ratios (Chang and Sawin, 1997). Meanwhile, the bombardment of positive ions towards the substrate can further enhance the etching process and lead to totally anisotropic etching (Flamm and Donnelly, 1981). Owing to the anisotropic etching achieved by the bombardment of positive ions, it has been possible to shrink the feature sizes in integrated circuits continuously during the past decades.

In the discharge process, the electrons play a key role. They sustain the plasma by ionizing neutral molecules and atoms and create the reactive Cl radicals by electron impact

dissociation of Cl_2 molecules. Better understanding of the particle balance process and the creation of radicals and ions in the discharge requires detailed analysis of parameters such as the effective electron temperature, the electron energy distribution function (EEDF), the ion energy distribution (IED) and the ion angular distribution (IAD). As for chlorine plasma which is widely used in processing of metals and semiconductors, the etching process is significantly enhanced by the bombardment of Cl_2^+ and Cl^+ ions (Donnelly and Kornblit, 2013). The effect of different combinations of bombarding ions and reactive neutrals on the etch rate has been investigated and the etching yield is found to scale with the square root of the incident ion energy and depend strongly on ion-to-neutral flux ratio (Levinson et al., 1997; Vitale et al., 2001). However, ions with very high energy can cause undesirable damage to the substrates and lead to loss of linewidth control (Lieberman and Lichtenberg, 2005). Meanwhile, the etching yield will saturate at low ion-to-neutral flux ratio (Levinson et al., 1997). Thus, the range of the ion energy and ion-to-neutral flux ratio has to be meticulously controlled for both high quality and high productivity in industrial production.

Capacitively coupled plasma (CCP) discharge, sustained by the rf (radio frequency) currents or voltages applied directly to the electrodes, is extensively used in the microelectronic industry and its application is further enhanced by the dual-frequency (DF) CCP regime which can possibly achieve the separate control of the flux and energy of the bombarding ions (Lee et al., 2004; Lieberman and Lichtenberg, 2005). Due to the merits of CCP and chlorine plasma, several attempts have been made for a comprehensive understanding of the capacitively coupled chlorine discharge, including modeling, experiments and simulations. Fluid models, global models and two-region models have been developed for a quick estimation of the plasma parameters. Experiments have been conducted to explore the properties of capacitively coupled chlorine discharge and the etching process. Meanwhile, numerical simulations, which usually adopt the particle-in-cell/Monte Carlo collision (PIC/MCC) method (Birdsall, 1991), are applied to simulate capacitively coupled chlorine discharge since PIC/MCC simulations

incorporate fewer assumptions compared with the models and gain deeper insights into the non-local and non-equilibrium phenomena of the plasma discharge compared with the experiments (Vahedi and Surendra, 1995). Nevertheless, these simulations were restrained by limited number of species included and limited reaction sets as they neglected the Cl^+ ions, Cl atoms, Cl^+ and Cl involved reactions and electron impact dissociation processes, which can play a significant role in the discharge and etching process.

In the conventional single-frequency (SF) CCP discharge, the positive ions are created in the bulk plasma and then accelerated to the substrate by a sheath potential developed near the surface. When transiting the sheath region, ions can gain enough energy so as to assist material processing at the surface. However, the ion flux in SF CCP is lower than in inductively coupled plasma (ICP) and electron cyclotron resonance (ECR) discharges, which limits the throughput. Furthermore, the ion flux is coupled with ion energy, so the energy of ions reaching the surface will inevitably increase when the ion flux is increased, leading to undesirable surface damage and loss of process control. Therefore, DF CCP discharge, usually operated by two sources with different frequencies, has been proposed in order to achieve separate control of ion flux and energy (Goto et al., 1992, 1993) and is the state-of-the art technique for manufacturing integrated circuits of extraordinary small size. Ideally, in DF CCP discharge, the low-frequency source mainly controls the ion energy and angular distributions while the high-frequency source determines the plasma density and the ion flux to the substrate. In the DF CCP discharge, a separate control of the flux and energy of the ions reaching the surface within certain range of parameter space can be achieved (Boyle et al., 2004). The plasma density is found to be mainly proportional to the square of the high frequency while the energy of the ions is found to be proportional to the low-frequency voltage (Lieberman and Lichtenberg, 2005). Nevertheless, the two sources inevitably have coupling (Gans et al., 2006; Ahn and Chang, 2009), which consequently leads to nonlinear dynamics of the discharge (Rauf and Kushner, 1999). Furthermore, in DF CCP discharge, the ions respond to the instantaneous electric field

in the sheath region, which may modify the energy and angular distributions of ions reaching the surface and influence the surface process.

Most of the previous investigations on DF CCP have been focused on electropositive gases such as Ar and He, electronegative gases such as CF_4 and SF_6, and their mixtures. The strongly electronegative chlorine discharge in the DF CCP regime has not been explored, though it is important in plasma processing, especially in the etching process. In this study, we will first explore the SF capacitively coupled chlorine discharge, and then extend our study to the DF capacitively coupled chlorine discharge. Both voltage driven and current driven discharges will be explored for the SF capacitively coupled chlorine discharge, while the two sources applied in the DF capacitively coupled chlorine discharge are both current sources.

In discharge analysis, the central problem is to explore the variation of plasma parameters under different control parameters so as to meet with the requirements for industrial application. In an earlier study, the oopd1 (object oriented plasma device for one dimension) simulation code using the PIC/MCC method has been benchmarked against the well established xpdp1 code for oxygen discharge (Gudmundsson et al., 2013). Here, we apply a hybrid approach of a volume averaged global model (Thorsteinsson and Gudmundsson, 2010a) and the oopd1 code to explore the capacitively coupled chlorine discharge with a more comprehensive reaction set and more species considered than in the earlier studies. The global model is used to find the dissociation fraction in the chlorine discharge and the oopd1 determines the kinetics of the discharge by PIC/MCC simulation. In section 2.1, we review the previous investigations on capacitively coupled chlorine discharges and dual-frequency capacitively coupled discharges. In section 2.2, the PIC/MCC method used in our simulation is briefly introduced. In section 2.3, we give a brief description of the simulation method and setup in our study. The role of the global model in the simulation, i.e., how the global model assists the PIC/MCC simulation, is also discussed therein. The reaction set and the cross sections used for the reactions in the PIC/MCC simulation are discussed in chapter 3. In section 4.1, the simulation results are compared with measured

experimental data and the validity of the code is demonstrated. In section 4.2, we simulate a typical capacitively coupled chlorine discharge driven by a voltage source in the pressure range 5 – 100 mTorr and study key plasma parameters such as the ion energy and angular distributions of both Cl^+ and Cl_2^+ ions, the electron energy probability function (EEPF) and the effective electron temperature, which heavily affect the discharge process and the plasma properties. In section 4.3, we analyze the effect of driving current, driving frequency and secondary electrons on key plasma parameters in a current driven capacitively coupled chlorine discharge, respectively. In chapter 5, we add another source, a low-frequency source, to extend the SF CCP discharge to a typical DF CCP discharge. We investigate how the discharge evolves with the addition of a low-frequency source. We especially analyze the effect of adding a low-frequency source with a non-zero secondary electron emission coefficient on the discharge and the ion energy and angular distributions of Cl^+ and Cl_2^+ ions.

Chapter 2

Overview

2.1 Background

This project aims to establish a simulation code for the capacitively coupled chlorine discharge and then explore both the SF and DF capacitively coupled chlorine discharges. Thus, the background information below generally consists of two parts. Section 2.1.1 gives a review of the previous investigations on SF capacitively coupled chlorine discharge, including analytical models, experimental measurements and numerical simulations. Section 2.1.2 states the motivation for the transition from SF CCP to DF CCP and gives a review of the previous investigations on DF CCP discharges. Since DF CCP for chlorine discharge has not been explored before, section 2.1.2 reviews investigations which are focused on DF CCP in other basic gases such as argon, oxygen and their mixtures. The previous studies provide guidance and are important references for subsequent studies in chapters 4 and 5.

2.1.1 Capacitively coupled chlorine discharge

Due to the electronegative property and good performance in semiconductor etching for chlorine plasma, researches on capacitively coupled chlorine discharge have been conducted by modeling,

experiments and simulations during the past decades and are reviewed as follows.

Fluid models (Park and Economou, 1990; Meyyappan and Govindan, 1991; Chung et al., 1997), global models (Rogoff et al., 1986; Lee et al., 1997; Lichtenberg et al., 1997) and two-region models (Aydil and Economou, 1992a, 1993; Lymberopoulos and Economou, 1994) have been developed to model the capacitively coupled chlorine discharge. The density profile for charged particles has been obtained and the chlorine discharge is found to be strongly electronegative, consisting of an electronegative core connected to an electropositive edge region (Lichtenberg et al., 1997). In addition, the transport of the charged species (Park and Economou, 1990), the excitation and ionization waveforms (Meyyappan and Govindan, 1991), the influence of the operating parameters on the characteristics of the discharge (Chung et al., 1997) and the scaling laws for the dependence of discharge parameters on gas pressure and absorbed power (Lee et al., 1997) have been analyzed. Besides, the etching of polysilicon by chlorine in the capacitively driven plasma reactor has been modeled (Aydil and Economou, 1992a, 1993).

Generally, these models are based on the continuity equations, Poisson equation and energy and particle balance equations. Although these models can give a quick estimation of the discharge, the quality of the estimation is restrained by the assumptions and approximations made in these models. For instance, the electron energy distribution function, which is demonstrated to affect the accuracy of calculated plasma parameters (Gudmundsson, 2001; Gudmundsson et al., 2012), has to be assumed in these models so as to calculate the electron temperature and other related parameters, rather than obtain those self-consistently.

Experiments have also been conducted and the properties of capacitively coupled chlorine discharge were characterized extensively, including the optical properties such as the opto-galvanic effect to determine the electronegativity (Kramer, 1986), the optical emission from ions and neutrals (Flamm and Donnelly, 1986) and its dependence on the driving frequency (Donnelly et al., 1985), the electrical properties such as the conductivity (Franz, 2005),

impedance and phase angle (Bose et al., 1994; Bose, 1995) and the particle properties such as the flux and energy distribution of ions bombarding the electrodes (Aydil and Economou, 1991), the electron heating mechanism (Franz and Klick, 2005; Franz, 2006), the density and/or temperature of electrons (Aydil and Economou, 1992b), ions (Donnelly et al., 1982) and neutrals (Ono et al., 1990, 1992; Franz, 2006). Among the above experiments, the etching of semiconductors with chlorine plasmas has also been studied (Ono et al., 1990, 1992; Aydil and Economou, 1991; Bose, 1995).

However, these experiments cannot fully describe the non-local and non-equilibrium phenomena owing to the limitations of the experimental setup. Also, the cost for experiments is high and sometimes the experiments are dangerous since chlorine is deleterious. Furthermore, when in DF CCP discharge, the strong coupling between the two rf sources makes it more difficult for the experimental measurements. Due to the inherent complexity of the plasma discharge and plenty of control parameters, only through the joint efforts of analytical analysis, experimental diagnostics and computational simulations can we have a deeper understanding of intricate physical and chemical processes in the discharge and the role of simulation is irreplaceable. Simulations can assist in parameter optimization for the physical design of the chamber. Besides, simulations can predict processing results. Although the simulation results are not strictly quantitatively reliable, they can give the general trend for the transitions in the discharge according to the variations of control parameters and reveal the intrinsic reasons, which can shorten the cycle for product development.

For the above reasons, numerical simulations, along with models and experiments, act as an indispensable tool since they adopt the PIC/MCC method (Birdsall, 1991) to self-consistently calculate the kinetics of every particle including the energy distribution functions, with fewer assumptions compared to the models and deeper insights into the non-local and non-equilibrium phenomena of the plasma discharge compared to the experiments (Vahedi and Surendra, 1995). PIC/MCC simulation has been used to simulate the capacitively coupled chlorine discharge and

the temporal behavior of the plasma parameters (Nanbu et al., 1999) and the dependence of the plasma structure on the discharge parameters (Kawano et al., 2000) have been explored and analyzed. Additionally, particle-in-cell/dynamic Monte Carlo (PIC/DMC) approach has been used to study the spatiotemporal electron dynamics (Lymberopoulos and Economou, 1995). Another particle based kinetic simulation, direct simulation Monte Carlo (DSMC) has been combined with PIC/MCC method to simulate the etching of silicon wafer and investigate the flow of radicals and the generation of etch products (Nanbu et al., 1999).

Nevertheless, these simulations were restrained by limited number of species included and limited reaction sets as they neglected the Cl^+ ions, Cl atoms, Cl^+ and Cl involved reactions and electron impact dissociation processes. Cl^+ ions, toghther with Cl_2^+ ions, can enhance the etching process and contribute to anisotropic etching. Besides, secondary electron emission from the electrodes can be caused by the bombardment of Cl^+ and Cl_2^+ ions to the electrodes, which can lead to the mode transition of the heating mechanism in the discharge and has not been explored yet. In our study, the Cl^+ ions, Cl atoms, Cl^+ and Cl involved reactions and the secondary electrons will be considered in order for a comprehensive understanding of the capacitively coupled chlorine discharge.

2.1.2 Dual-frequency capacitively coupled discharge

All the investigations reviewed in section 2.1.1 are focused on SF capacitively coupled chlorine discharge. The advantages of SF CCP mainly lie in its high uniformity, low complexity and low cost, which are all beneficial for industrial applications compared with other excitation regimes such as ICP and ECR (Lieberman and Lichtenberg, 2005). Although the advantages of SF CCP are obvious, the drawbacks are also apparent. One problem is that the plasma density in CCP is lower than in ICP and ECR by one or two orders of magnitude, which limits the throughput and diminishes the efficiency for the manufacturing process. The other problem, which is the crucial limiting feature for SF CCP, is that the ion energy and flux to the wafer cannot be

Table 2.1: Comparison of different excitation methods for plasma discharge.

	ICP	ECR	SF CCP	DF CCP
gas pressure [mTorr]	1 – 100	0.5 – 10	1 – 300	1 – 300
driving frequency [MHz]	13.56	2450	1 – 160	1 – 160
plasma density [m^{-3}]	10^{16} – 10^{18}	10^{16} – 10^{18}	10^{15} – 10^{17}	10^{15} – 10^{17}
ion flux and energy	decoupled	decoupled	coupled	decoupled
plasma uniformity	high	low	higher	highest
oxide etching	not very fit	no	yes	yes
cost and complexity	high	highest	lowest	low

varied independently. This situation is analogous to the semiconductor p-n junctions and diode vacuum tubes where the voltage and current cannot be controlled separately. To be specific, if the ion flux to the wafer is increased so as to satisfy the requirement for efficiency in processing or throughput in fabrication, the ion energy will be increased inevitably, and the energetic ions will lead to undesirable damage to the wafer and defect in the product. Moreover, the combinations of ion flux and energy cannot be modulated, which leads to a relatively narrow process window for many applications.

Confronted with the above problems in SF CCP, a new regime, DF CCP, which can solve the problems mentioned above while maintaining most advantages of SF CCP, has been proposed by Goto et al. (1992, 1993) and the superiority of DF CCP in etching has been demonstrated. The merits and demerits of ICP, ECR, SF CCP and DF CCP are generally compared in table 2.1. Ideally, in DF CCP discharge, the plasma density scales with the square of the high frequency, f_{hf}^2, and the ion energy to the wafer scales with the low-frequency voltage, V_{lf}, (Lieberman and Lichtenberg, 2005), which reveals that the high frequency mainly controls the ion flux and the low frequency controls the ion bombarding energy. So we can set $f_{\mathrm{hf}} \gg f_{\mathrm{lf}}$ (f_{lf} is the low driving frequency) and $V_{\mathrm{hf}} \ll V_{\mathrm{lf}}$ (V_{hf} is the high-frequency voltage) to try to increase the plasma density and decouple the power sources so as to control the ion flux and ion energy to the wafer surface independently.

In recent years, investigations on DF CCP are mainly focused on two issues. One is the investigation in the electron heating mechanism (Kim and Lee, 2004; Kawamura et al., 2006;

Turner and Chabert, 2006, 2007a; Turner, 2009; Lieberman and Lichtenberg, 2010). The electron heating in the discharge mainly consists of Ohmic heating in the bulk region and stochastic heating in the sheath region (Turner, 2009), while the secondary electrons emitted from the electrode due to the bombardment of energetic ions can also play significant role in the heating mechanism (Kim and Lee, 2004; Ahn and Chang, 2009). As the low-frequency current increases for the fixed high-frequency current, the EEPF changes from Druyvesteyn like to bi-Maxwellian like or Maxwellian, which is attributed to the transition from collisional to collisionless property of the low-energy electrons (when the secondary electron emission is negligible) or the transition from the low-voltage to high-voltage mode (when the secondary electron emission is dominant) (Kim and Lee, 2004). The other issue is the study of the ion properties including the IED and IAD at the electrode surface (Wakayama and Nanbu, 2003; Wang et al., 2007; Bi et al., 2009; Wang et al., 2012). The IED in DF CCP is broad and bimodal and is found to shift towards the low-energy region with increasing gas pressure or decreasing applied voltage (Georgieva et al., 2004). The IAD is found to spread to large-angle region with increasing pressure while be more concentrated in small-angle region with increasing applied voltage (Wang et al., 2007, 2012).

Hitherto, most investigations on DF CCP have been focused on electropositive gases, e.g., Ar (Wakayama and Nanbu, 2003; Boyle et al., 2004; Kim and Lee, 2004, 2005a,b; Turner and Chabert, 2006, 2007a,b; Ahn and Chang, 2009; Sharma and Turner, 2013) and He (Gans et al., 2006), electronegative gases, e.g., CF_4 (Donkó and Petrović, 2006; Wang et al., 2012) and SF_6 (Tong and Nanbu, 2006), and their mixtures, e.g., Ar/CF_4 (Rauf and Kushner, 1999; Bi et al., 2009), $Ar/CF_4/N_2$ (Georgieva et al., 2003) and Ar/O_2 (Zhang et al., 2013). The strongly electronegative chlorine discharge in the DF CCP regime has not been explored, though it is important in plasma processing, especially in the etching process. Therefore, we will explore the DF capacitively coupled chlorine discharge in our study and primarily investigate the effect of varying the low-frequency current on the discharge.

2.2 PIC/MCC simulation

The oopd1 code used for simulating the capacitively coupled chlorine discharge generally adopts the particle-in-cell/Monte Carlo collision (PIC/MCC) method (Birdsall, 1991). PIC/MCC method mainly consists of two modules, which are the motion of particles, i.e., the PIC module, and the collision of particles, i.e., the MCC module.

In the PIC module, the particles are followed in their own and applied electric and magnetic field using first principles calculations. The kinetics of the particles are calculated self-consistently and the particles are advanced according to the equations of motion. Since the number of physical particles is so large that the computer can hardly track the trajectory and monitor the velocity for every physical particle due to the limited capacity, we use computer particle, also called superparticle, in the simulation. Each superparticle represents 10^7 – 10^8 real particles in the real discharge. By this means, the amount of calculation is substantially reduced while the validity of the simulation can still be guaranteed since the particles are all subject to the equations of motion from first principles and most cross sections used in the code have been determined experimentally.

In the MCC module, collisions which occur in one time step are determined. First, the colliding particles are sampled. Second, a random number is generated by the computer to determine the collision type for the particles. Then the particles are frozen at their position and the velocity of the particles after the collision is calculated according to the conservation of momentum and energy. In this step, only the velocity of the particle is changed and the position is not changed.

The PIC/MCC method is an iterative process consisting of six steps. The simulation must run for a sufficient period of time in order to search for a steady-state solution. Besides, the simulation must run with a sufficient number of particles in order to minimize the discrete particle noise. The flow chart for the PIC/MCC method is shown in figure 2.1 and the six steps are described as follows.

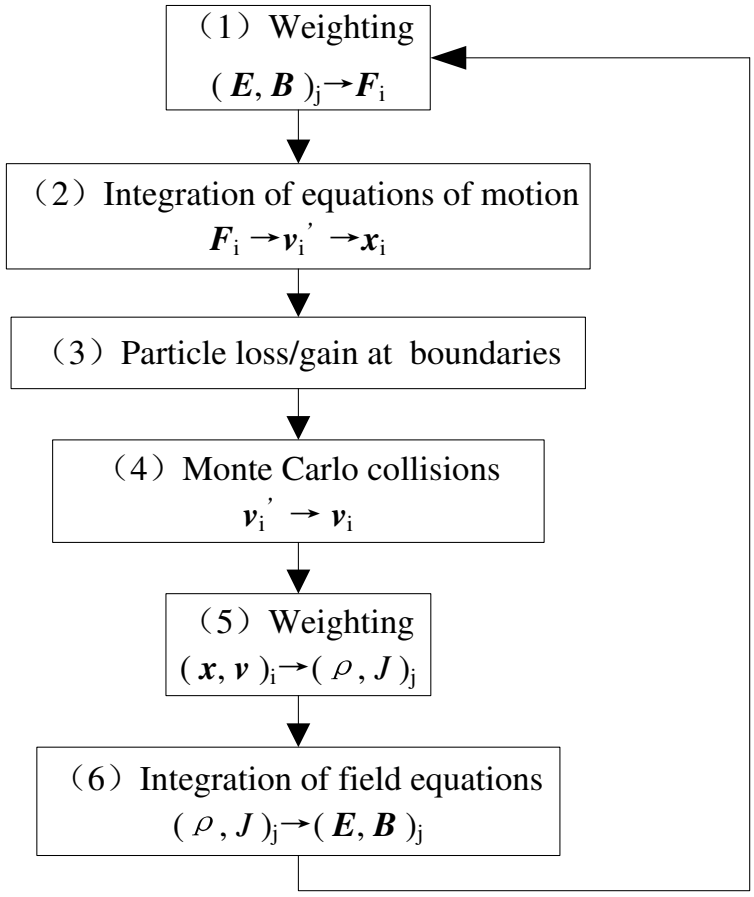

Figure 2.1: The flow chart for the oopd1 simulation code adopting the PIC/MCC method used to simulate the discharge.

In step 1, the discharge is initialized with the discharge area divided into certain number of cells and the superparticles are uniformly distributed into these cells with a Maxwellian velocity distribution. The electromagnetic field ($\boldsymbol{E}$, $\boldsymbol{B}$) distributed on each cell is numerically calculated using interpolation from the velocity ($\boldsymbol{v}$) and position ($\boldsymbol{x}$) of each particle and consequently the force ($\boldsymbol{F}$) operating on each particle at time t is obtained though

$$\boldsymbol{F}(\boldsymbol{x}^t, \boldsymbol{v}^t) = m\frac{d\boldsymbol{v}^t}{dt} = q(\boldsymbol{E}^t + \boldsymbol{v}^t \times \boldsymbol{B}^t). \tag{2.1}$$

In step 2, the velocity and position of each particle are advanced according to the equations

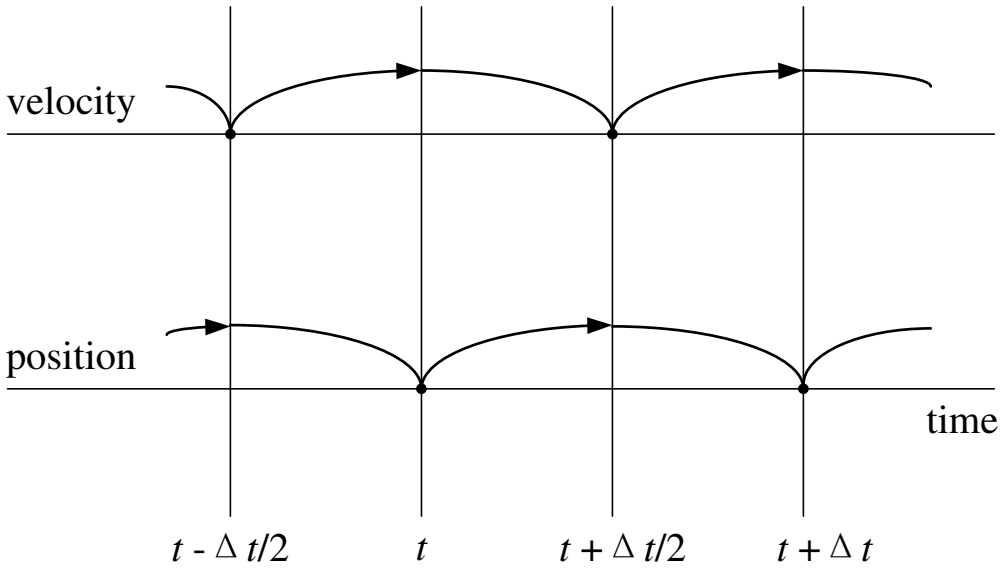

Figure 2.2: Schematic leapfrog method used in the PIC/MCC method to advance the velocity and position of each particle.

of motion

$$m\frac{\boldsymbol{v}^{t+\Delta t/2} - \boldsymbol{v}^{t-\Delta t/2}}{\Delta t} = \boldsymbol{F}(\boldsymbol{x}^t, \boldsymbol{v}^t) \tag{2.2}$$

$$\frac{\boldsymbol{x}^{t+\Delta t} - \boldsymbol{x}^t}{\Delta t} = \boldsymbol{v}^{t+\Delta t/2} \tag{2.3}$$

where Δt is the timestep for the simulation. The integration starts from known $\boldsymbol{x}^t$ and $\boldsymbol{v}^{t-\Delta t/2}$ and produces $\boldsymbol{x}^{t+\Delta t}$ and $\boldsymbol{v}^{t+\Delta t/2}$ later. This is called the leapfrog method and is graphically shown in figure 2.2. These two first-order difference equations are time centered, so that the integration of both together is second-order accurate (Δt^2 error).

In step 3, after each particle position is advanced in time, the new location is tested to find whether some particles reach the boundaries. If so, some boundary adjustments would occur such as the recombination of particles (particle loss and gain process) and secondary electron emission (particle gain process).

In step 4, the Monte Carlo method (Vahedi, 1993) is used to determine which reaction should take place for a specific particle. The possibility for the occurrence of each reaction is generally assumed to be proportional to the cross section of each reaction. The velocity of each

particle is calculated after the collision. The process of Monte Carlo collision is described in detail as follows.

In the simulation, we define background species (usually the neutral species) as a species whose density is constant and uniform. Particle species (usually the charged species), on the other hand, are characterized by superparticles whose distribution functions evolve temporally and spatially as the simulation advances. Assume that the incident particle species s has N types of collisions with a target species. The target species could be a background species (neutral) or another particle species. The kinetic energy of the i-th particle of the incident s species is $\mathcal{E}_i$. The cross section for the j-th type of collision between the s species and the target species is $\sigma_j(\mathcal{E}_i)$, $1 \leq j \leq N$. The total cross section

$$\sigma_T(\mathcal{E}_i) = \sigma_1(\mathcal{E}_i) + \sigma_2(\mathcal{E}_i) + ... + \sigma_N(\mathcal{E}_i). \tag{2.4}$$

The collision frequency for the j-th type of collision is given by

$$\nu_j = n_t \sigma_j v \tag{2.5}$$

where n_t is the local density of the target species at the position of the i-th particle and v is the velocity of the i-th particle. Note that typically the target particles are assumed to be uniformly distributed in the system as a background species with a constant n_t, in which case the collision frequency for each reaction is proportional to the corresponding cross section.

Since the collision frequency for a specific reaction varies as the kinetic energy of the incident particle varies, a constant collision frequency $\nu^{'}$ is chosen to be

$$\nu^{'} = \max_{\boldsymbol{x},\mathcal{E}}(n_t \sigma_T v) \tag{2.6}$$

In a sense what we have done is to introduce another collisional process with a collision frequency

which, when it is added to the total collision frequency $n_t \sigma_T v$, gives a constant value over all $\boldsymbol{x}$ and $\mathcal{E}$ as shown in figure 2.3. This collision process is called the null collision since no real collision occurs. Therefore, after the addition of null collision, the maximum fraction of the total number of particles in the simulation which experience collisions is given by

$$P_{\text{null}} = 1 - \exp(-\nu' \Delta t) \tag{2.7}$$

The colliding particles are chosen randomly and each particle is checked for type of collision, see figure 2.3, using

$$\begin{array}{rcccll} & R & \leq & \nu_1(\mathcal{E}_i)/\nu' & \text{(collision type 1)} \\ \nu_1(\mathcal{E}_i)/\nu' & \leq & R & \leq & (\nu_1(\mathcal{E}_i) + \nu_2(\mathcal{E}_i))/\nu' & \text{(collision type 2)} \\ & & \cdot & & & \\ & & \cdot & & & \\ & & \cdot & & & \\ \sum_{j=1}^{N} \nu_j(\mathcal{E}_i)/\nu' & \leq & R & & & \text{(null collision)} \end{array}$$

where R $(0 \leq R \leq 1)$ is a random number generated by the computer.

In steps 5 and 6, the locations and velocities of the particles are used to determine the charge and current density (ρ, J) on the grid. These quantities are then used as source terms in Maxwell's equations, along with the applied boundary conditions, to advance the electromagnetic field.

In order for stability in running the simulation, the time step Δt and grid spacing Δx are chosen to resolve the electron plasma frequency, ω_{pe}, and the electron Debye length, λ_{De}, of the low-energy electrons or

$$\omega_{\text{pe}} \Delta t < 0.2 \tag{2.8}$$

and

$$\Delta x < \lambda_{\text{De}}. \tag{2.9}$$

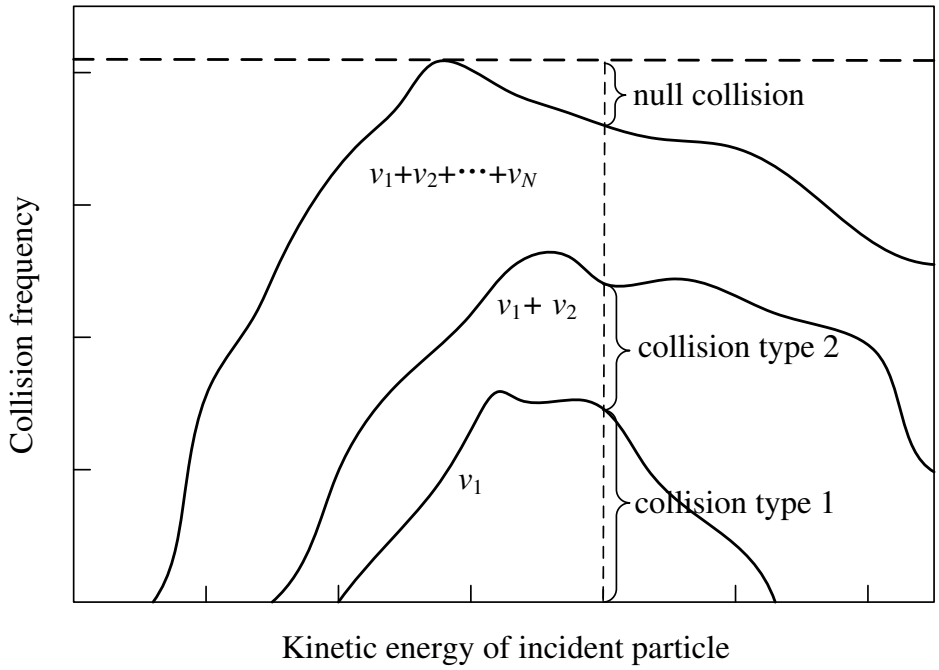

Figure 2.3: The addition of null collision in the Monte Carlo collision resulting in a constant collision frequency over all energies (Vahedi, 1993).

2.3 Research objectives

2.3.1 Code development

In order to simulate the capacitively coupled chlorine discharge, initially we should develop the oopd1 code for the simulation of chlorine discharge. There already exists several commercial software for plasma simulation with modular structures, friendly interfaces and abundant database. However, the codes for these commercial software are not open to public and it is difficult to realize the algorithms and data structures. Sometimes even the physical models adopted in these softwares cannot be comprehended. Thus, the xpdx1 series codes (Verboncoeur et al., 1993) have been developed for scientific purpose and become very popular and widely used. The xpdx1 series contain xpdp1, xpdc1 and xpds1 for planar, cylindrical and spherical geometries, respectively. The one-dimensional object-oriented plasma device code oopd1 (Hammel and Verboncoeur, 2003), is a partial reduction of the 2D oopic code

(Verboncoeur et al., 1995), originally developed by Professor John P. Verboncoeur and his co-workers at the Plasma Theory and Simulation Group at the University of California at Berkeley. This code aims to replace the xpdx1 series since oopd1 is an objective-oriented code, with modular structures which are easy to write, read, add to and change compared with the xpdp1 series. Basically, oopd1 adopts the PIC/MCC method and uses relativistic collision model. Besides, the oopd1 can enable the use of variable weighting factors for different species, which makes it possible to simulate electronegative discharge in which the density of ions is much higher than the electrons. This code also allows to follow neutral particles that have significantly higher density than charged particles. In addition to the above advantages of oopd1, the algorithm and structure in this code are also easy to understand, which is beneficial for the usage and, more importantly, secondary development.

After comprehending the algorithm and structure of oopd1, we added the reaction set to describe the chlorine discharge. To be specific, we choose 44 reactions for the chlorine discharge according to the previous work (Thorsteinsson and Gudmundsson, 2010a,b; Gudmundsson et al., 2013), and then search the cross section data for each reaction from the literature. As for the desired cross section data which has not been experimentally measured or theoretically calculated, we use data from other similar gases such as oxygen. As for some reactions with several conflicting cross sections, we either choose one according to the recommendations from other researchers or select parts from given cross sections and then group them together in a reasonable way to make a fitted cross section. The reaction set and cross section data will be introduced in chapter 3. After the cross section data and threshold for each reaction have been collected and selected, we load them in the code and add suitable interface so that the newly added part is compatible with the whole code. Then we run simulations using the newly revised code and compare simulation results with available measurements in section 4.1. Agreement between our simulation results and experimental measurements is good. Thus, we are convinced that the code we have developed can actually simulate capacitively coupled chlorine discharge.

Then the oopd1 is used to explore the SF and DF capacitively coupled chlorine discharges in subsequent studies.

2.3.2 Simulation method

The method we use to simulate the capacitively coupled chlorine discharge is actually a hybrid approach as we use both a global model (Thorsteinsson and Gudmundsson, 2010a; Gudmundsson et al., 2012) and a particle-in-cell/Monte Carlo simulation. The reasons why we apply this hybrid approach can be explained from two perspectives.

(I) For a pure Cl_2 feedstock gas, Cl atoms are formed mainly through electron impact dissociation of Cl_2 molecules. The Cl density is assumed to be low and is known to have little effect on the explored discharge (Park and Economou, 1990) and this assumption is expected to be even more relevant for lower input power. However, the fraction of Cl atoms in the feedstock gas has been found to influence the profile of the EEDF and the effective electron temperature since the momentum exchange cross section of Cl atoms is smaller than that of Cl_2 molecules (Aydil and Economou, 1992a). In addition, the fraction of Cl atoms has been theoretically calculated (Aydil and Economou, 1992a) and experimentally found (Aydil and Economou, 1992b) to be about 2 – 3 % and increase linearly with the absorbed power. Thus, both the Cl atoms and Cl_2 molecules should be considered in the discharge.

(II) If the Cl atoms and Cl_2 molecules are treated as particles in the discharge, since the number of Cl atoms and Cl_2 molecules is much larger than the charged species in the weakly ionized plasmas, there will be large amounts of superparticles for the neutrals. Consequently, the computer will run out of memory and the computational time is formidable if we treat all the Cl atoms and Cl_2 molecules as particles and track the trajectory of each neutral.

Confronted with the requirement to consider the neutrals in the discharge and the limitation of the computer, we make a compromise. We initially assume an empirical value of the absorbed power, P_{abs}, for a certain discharge and use it as an input parameter in a global model to

determine the fraction of Cl atoms and consequently the fraction of Cl_2 molecules. Then we assume both Cl_2 molecules and Cl atoms as the background gas with the fraction for each calculated from the global model. By this means, it is feasible to run the simulation without running out of memory. When the simulation runs to the steady state, we record the absorbed power and the profile of EEPF (bi-Maxwellian, Maxwellian or Druyvesteyn) obtained in the PIC/MCC simulation and use them as input parameters in the global model to calculate the fraction of Cl atoms again. Then we modify the fraction of Cl atoms in the background gas and rerun the simulation. The above process is done iteratively until the absorbed power we input in the global model calculation is the same as the absorbed power output from the PIC/MCC simulation. We assume that the gas pressure, p, in the discharge dose not change with dissociation, similar to the assumption in a global model made by Rogoff et al. (Rogoff et al., 1986). With the assistance of the global model, the time spent on the PIC/MCC simulation is substantially reduced.

We also make several assumptions and approximations in our study so as to simplify the simulation in a reasonable way and focus on the key parameters of our interest. These assumptions and approximations are listed below and described in detail in respective sections.

(I) All the reactions are assumed to occur between two particles such as electron-electron reaction, electron-neutral reaction and ion-neutral reaction. Three body reactions are not considered here due to its relatively small cross section and the low pressure condition.

(II) The central problem of discharge analysis is that given the control parameters, we should find the plasma parameters. Therefore, we mainly concentrate on the behavior of chlorine plasma in the discharge area. We omit the wafer and do not involve the simulation in the etching process at the surface. Instead, we assume that the neutral gas between the two electrodes is the background gas, which is uniform and in thermal equilibrium with a Maxwellian energy distribution at room temperature $T_g = 300$ K. This assumption is approximately valid because the influence of the gas flow through the chamber is relatively weak.

(III) We assume specific secondary electron emission coefficient and recombination coefficient at the surface in order to represent the real physics in the reactions between the wafer and the gas particles. We use 0.5 as the surface recombination coefficient because this value is within the reasonable range of measured Cl recombination coefficient. We do not assume specific material for the surface, but 0.5 is a reasonable choice if the electrodes are stainless steel.

(IV) The oopd1 code is a 1d-3v (one dimension in spatial space and three velocity components in phase space) code, which can describe the behavior of the plasma in one dimension (planar, cylindrical or spherical) in the spatial space and three velocity components in the phase space. This can save the running time for the simulation and one-dimensional description of the system suffices when modeling a capacitively coupled discharge due to the large ratio of transverse to longitudinal dimensions.

2.3.3 Single- and dual-frequency capacitively coupled chlorine discharges

After the simulation code has been developed and the method has been determined for simulating capacitively coupled chlorine discharge, the discharge model, i.e., the main objective, to be explored should be established. Figure 2.4 shows the schematic diagram of the diode parallel-plate plasma reactor in which the capacitively coupled plasma discharge is generated and sustained (Aydil and Economou, 1992a; Lymberopoulos and Economou, 1994). In the real experimental setup, the electrodes are placed in a vacuum chamber. The top electrode is usually equipped with uniform arrangement of pinholes, i.e., showerheads, through which the neutral gas is pumped in, while the bottom electrode usually holds the semiconductor wafer where the etching and deposition processes occur. The gases flowing through the chamber are ionized by the electric field between the two electrodes and plasmas consisting of electrons, ions and radicals are produced. The surface processing such as etching is done by the reactions

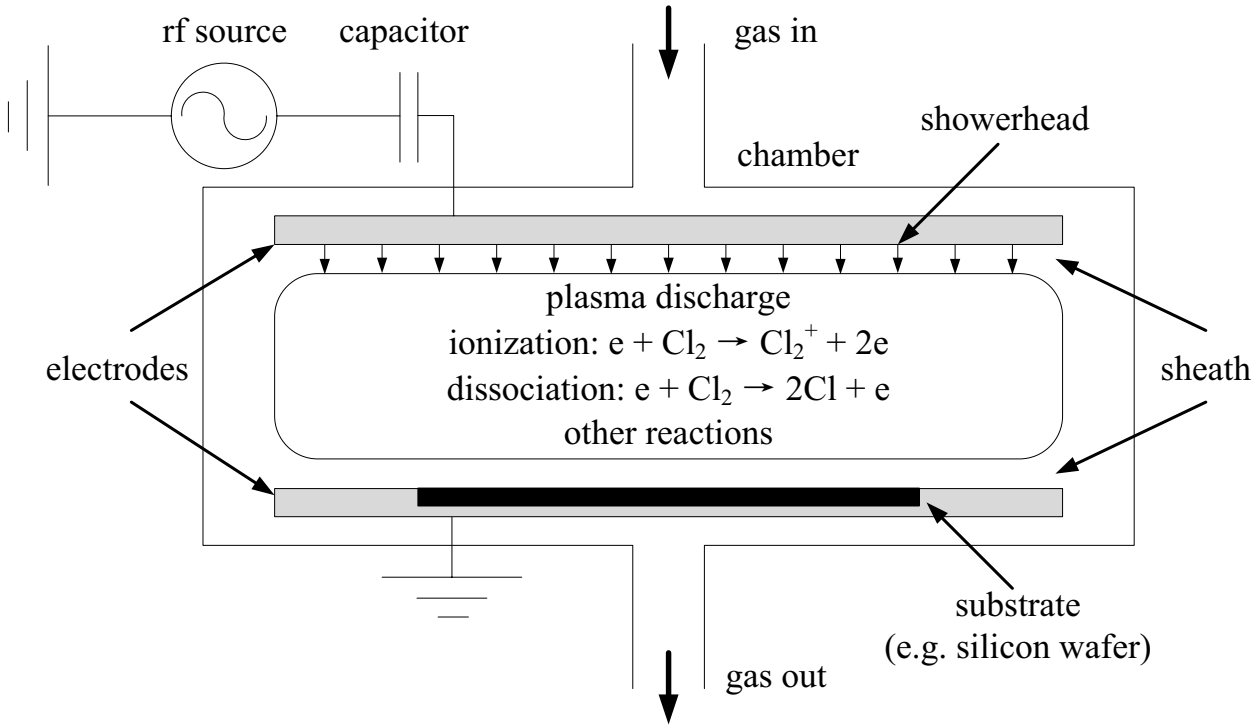

Figure 2.4: The schematic diagram of rf driven capacitively coupled chlorine plasma discharge.

between radicals and the wafer placed on the grounded electrode and the processing can be enhanced by the energetic bombardment of positive ions to the wafer surface.

In manufacturing process, circuit patterns are transferred to the film by exposing its surface to the species formed in plasma discharge. The etching mechanisms can be classified into four basic categories as shown in figures 2.5(a) – (d) (Lieberman and Lichtenberg, 2005). Chemical etching shown in figure 2.5(a) is mainly achieved by the radicals produced in the discharge. These radicals are neutral species and react with the surface material through conventional chemical reactions. In the sputtering as shown in figure 2.5(b), the material of the film is mainly mechanically ejected from its surface by the energetic bombardment of positive ions towards the surface. Selectivity and anisotropy often compete and are critical requirements in the etching process. Chemical etching has high selectivity and low anisotropy. Sputtering, on the contrary, shows complementary features, with high anisotropy and almost no selectivity. Therefore, ion-enhanced etching has been developed to possibly realize both high selectivity

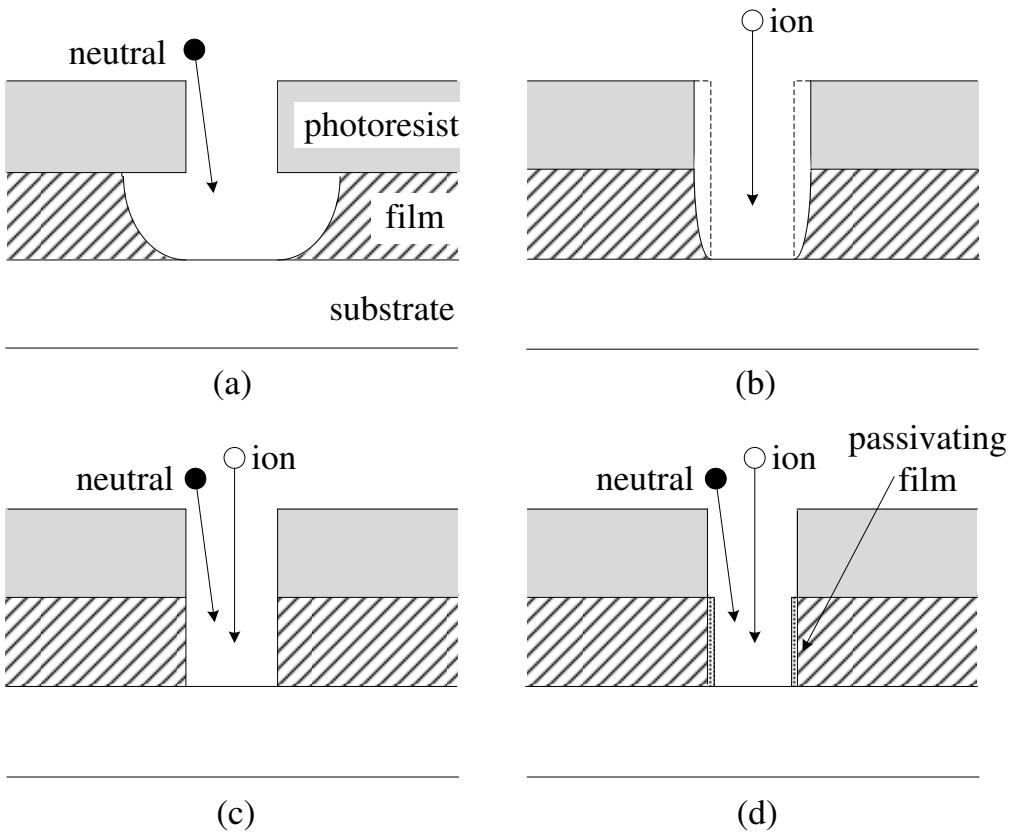

Figure 2.5: The four etching mechanisms in integrated circuit manufacture: (a) chemical etching, (b) sputtering, (c) ion-enhanced energetic etching and (d) ion-enhanced inhibitor etching.

and high anisotropy in the etching (Coburn and Winters, 1979). Ions can assist the etching process through two approaches, which are ion-enhanced energetic etching and ion-enhanced inhibitor etching as shown in figures 2.5(c) and (d), respectively. In ion-enhanced energetic etching, the ions are supposed to change the characteristic of the surface so that the chemical reactions between etchants and wafer materials occur more easily and frequently. In ion-enhanced inhibitor etching, the bombarding ions constantly prevent the deposition and growth of passivating film (inhibitor) on horizontal surfaces (see figure 2.5(d)). The passivating film only deposits on vertical surfaces and therefore the etching is strictly anisotropic. As to the chlorine discharge, ion-enhance energetic etching is mainly applied in etching semiconductors such as silicon while ion-enhanced inhibitor etching is mainly applied in etching metals such as

aluminium (Flamm, 1990).

As shown in figure 2.4, the plasma discharge includes many processes, such as the creation of plasma between the electrodes, the transport of created species through the sheath to the substrate, the reaction between the etchants and wafer materials. These processes are all important in manufacturing and of interest to researchers. Since we cannot consider all the important and interesting processes at the same time, we have to choose just one or two main processes, temporarily ignoring other processes and simplifying the discharge model to be explored. An overview of research on plasma discharge is shown in figure 2.6. According to figure 2.6, the central problem of discharge analysis is that given the control parameters for the driving source, the feedstock gas and the chamber geometry, the plasma parameters, including the plasma density, the ion flux hitting the electrode, the electron temperature, EEDF, IED and IAD, are determined. The control parameters are like knobs that can be twisted in order to tune the properties of the discharge for specific applications. These control parameters can be classified into three categories. (I) Parameters for the driving source such as the driving frequency, the rf current or voltage and the absorbed power. (II) Parameters for the feedstock gas such as the discharge pressure, the flow rate and the chemical components of the gas. (III) Parameters for the chamber geometry such as the area of the electrode and the gap length between the electrodes. In a CCP discharge, the spatial potential and the electric field distribution, the electron temperature, the radical density, the ion density, the radical and ion flux to the substrate, the IED and IAD at the substrate surface, the neutral energy distribution (NED) and neutral angular distribution (NAD) at the substrate surface are of interest. These parameters are critical to the etching properties and the relation between the requirements for etching and the explored parameters are listed in table 2.2.

Owing to the above reasons, we mainly concentrate on the behavior of chlorine plasma in the discharge area, investigating how the chlorine plasma is excited and sustained, how the particles such as radicals and energetic ions reach the surface and how the energy and momentum of

Table 2.2: The requirements for etching and the corresponding requirements for the parameters in plasma discharge.

Requirements for etching	Requirements for plasma parameters
High etching rate	High density and flux for radicals and ions
High anisotropy	Narrow IAD
High uniformity	Uniform radial density for radicals and ions
Selectivity and desired etching profile	IED and IAD modulated in reasonable range
Low dielectrical damage	Low energy for ions

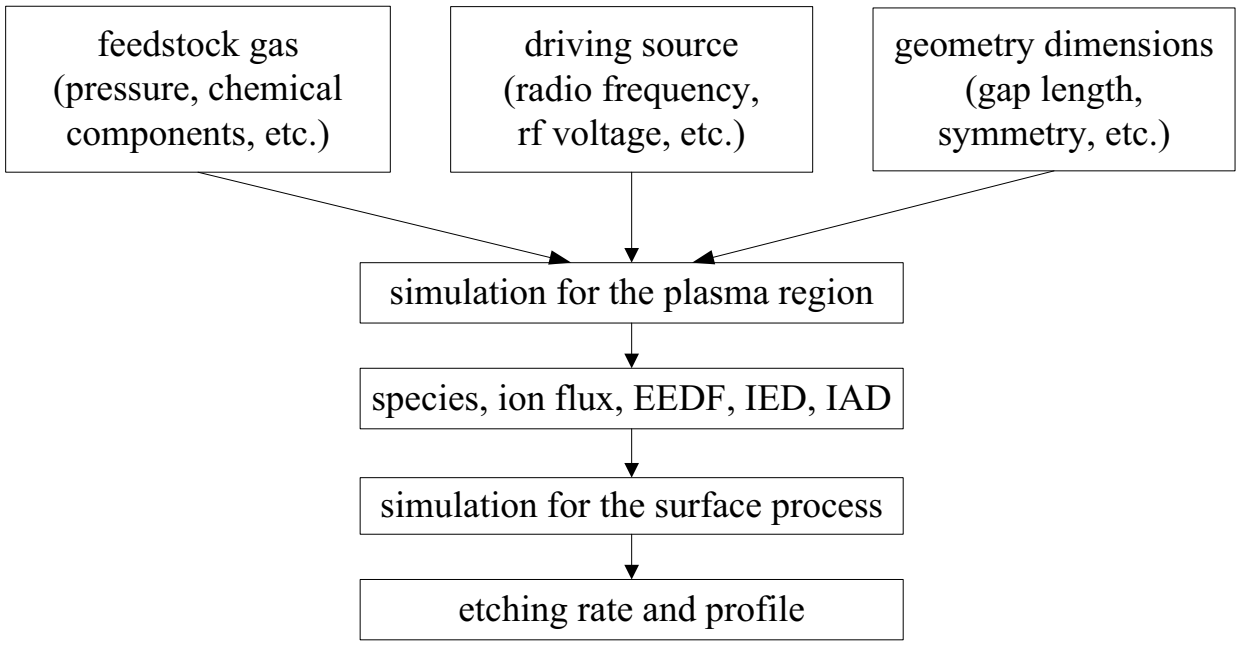

Figure 2.6: An overview of research on plasma discharge.

these particles are distributed at the surface of the substrate. Accordingly, we omit the wafer on the grounded electrode and do not involve the simulation for the etching process at present. After the above simplifications, the diagrams of the diode parallel-plate plasma reactor used in our simulation for single- and dual-frequency capacitively coupled discharge are shown in figures 2.7 and 2.8, respectively.

In the simulation for single-frequency capacitively coupled chlorine discharge shown in figure 2.7, we apply a voltage and a current source, respectively. The bottom electrode is grounded and the top electrode is subject to a driving source. The specific setup parameters for

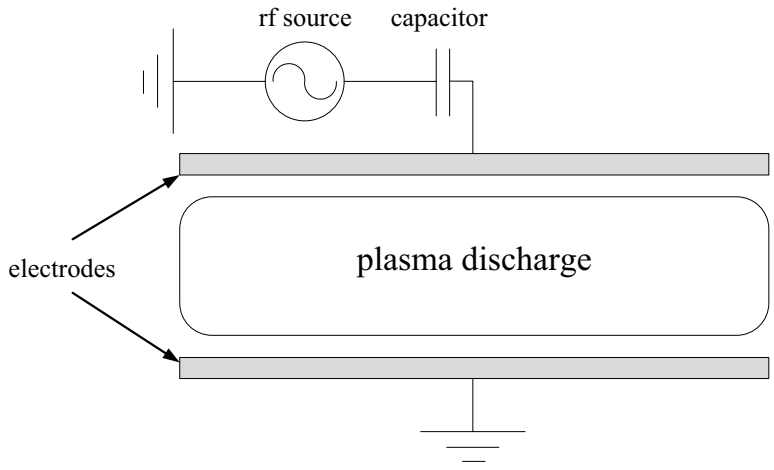

Figure 2.7: The schematic diagram of the simplified model used to simulate single-frequency capacitively coupled chlorine discharge.

voltage and current driven capacitively coupled chlorine discharges are described in sections 4.2 and 4.3, respectively. Apart from the type of driving source, another difference between the models in sections 4.2 and 4.3 is the chamber geometry. The chamber geometry applied in section 4.2 is the same as the capacitively coupled oxygen discharges explored in the previous studies (Lichtenberg et al., 1994; Gudmundsson et al., 2013), while the chamber geometry applied in section 4.3 is the same as the GEC (Gaseous Electronics Conference) rf reference cell (Hargis et al., 1994; Olthoff and Greenberg, 1995). In particular, we will explore the effect of gas pressure on the discharge in section 4.2 and explore the effect of driving current, driving frequency and secondary electron on the discharge in section 4.3.

In the simulation for dual-frequency capacitively coupled chlorine discharge shown in figure 2.8, the top electrode is grounded, with the bottom electrode, on which the wafer is placed, subject to two rf sources with different frequencies and current amplitudes. Due to the symmetric geometry, whether the top or the bottom electrode is grounded has no influence on the discharge. The high frequency, f_{hf}, is usually in the range 13.56 – 160 MHz, while the low frequency, f_{lf}, is usually in the range 0.46 – 13.56 MHz (Bi et al., 2011). The rf voltages and powers are from tens of to thousands of volts and watts, respectively, depending on specific applications. For etching devices, typical frequency combinations are 27.12/2 MHz,

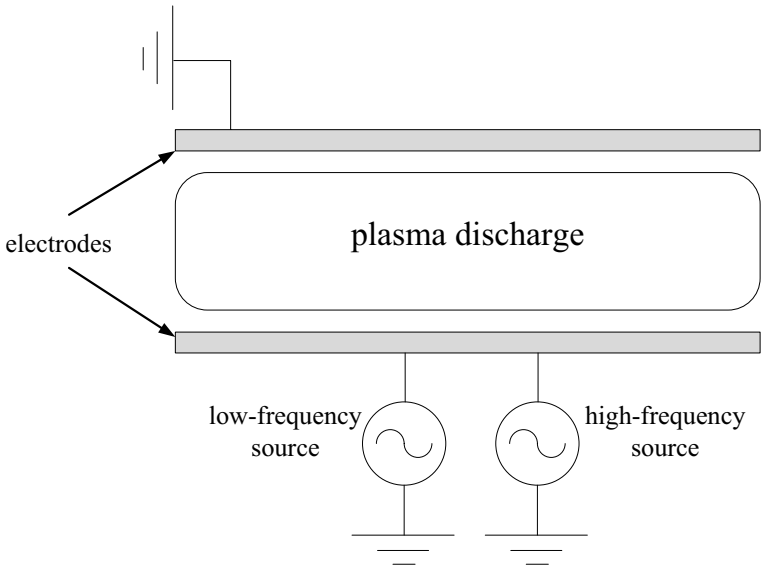

Figure 2.8: The schematic diagram of the simplified model used to simulate dual-frequency capacitively coupled chlorine discharge.

60/2 MHz and 160/13.56 MHz, while the typical frequency combination for deposition devices is 13.56/0.46 MHz (Bi et al., 2011). The specific setup parameters in dual-frequency capacitively coupled chlorine discharge are described in chapter 5. The chamber geometry applied is the same as in section 4.3. Other parameters which are not especially mentioned in chapter 5 are the same as the parameters used in current driven single-frequency capacitively coupled chlorine discharge discussed in section 4.3. We will explore the effect of the low-frequency current on the discharge in section 5.1. Particularly, we analyze the effect of adding a low-frequency source with a non-zero secondary electron emission coefficient in section 5.2 and the spatial IEDs and IADs of Cl_2^+ and Cl^+ ions in section 5.3.

Chapter 3

Chlorine specific parameters

In this study we consider a chlorine discharge that consists of electrons, the ground state chlorine molecule $Cl_2(X^1\sum_g^+,\ v=0)$, the ground state chlorine atom $Cl(^2P_u)$, the negative chlorine ion $Cl^-(^1S_g)$ and the positive chlorine ions $Cl^+(^3P_g)$ and $Cl_2^+(^2\Pi_g)$. The Cl atom has the highest electron affinity among all the elements of 3.61 eV (Gottscho and Gaebe, 1986), while the Cl_2 molecule has a very low (nearly zero) threshold energy for dissociative attachment with a low dissociation energy (2.48 eV) and a high electron affinity (2.45 eV) (Christophorou and Olthoff, 1999). According to the potential-energy diagram for excited states of the Cl_2 molecule (Christophorou and Olthoff, 1999), the electronic excited states of Cl_2 molecule are all repulsive states rather than attractive states, which means all electronic excitations appear to be dissociative with ground state Cl + Cl pair as the final products. Therefore, metastable Cl_2 molecule can hardly be sustained and are neglected in our code due to their little significance in the discharge. The discussion of the reaction set and the cross sections used is taken from Huang and Gudmundsson (2013).

Table 3.1: The reaction set for the chlorine discharge with the threshold energies, the references to the cross sections and the reference frame used for the cross sections for the heavy-particle collisions, i.e., target rest frame (TRF) or center of mass frame (CMF). (Cl_2^* and Cl^* denote the excited states of Cl_2 molecule and Cl atom, respectively.)

Reaction	Process	Thresh. [eV]	Ref.	Frame
Electron impact Cl_2				
$e + Cl_2 \longrightarrow e + Cl_2$	Elastic scattering	0	(Gregório and Pitchford, 2012)	–
$e + Cl_2 \longrightarrow Cl_2^+ + 2e$	Ionization	11.47	(Basner and Becker, 2004)	–
$e + Cl_2 \longrightarrow Cl + Cl^+ + 2e$	Ionization	15.7± 0.3	(Calandra et al., 2000) (Basner and Becker, 2004)	–
$e + Cl_2 \longrightarrow 2Cl^+ + 3e$	Ionization	31.13	(Calandra et al., 2000) (Basner and Becker, 2004)	–
$e + Cl_2 \longrightarrow Cl + Cl^-$	Dissociative attachment	nearly zero	(Kurepa and Belić, 1978) (Ruf et al., 2004)	–
$e + Cl_2 \longrightarrow Cl^+ + Cl^- + e$	Polar dissociation	11.9 ± 0.2	(Golovitskii, 2000)	–
$e + Cl_2 \longrightarrow Cl_2^* + e$	Excitation (see table 3.2)	–	–	–
Electron impact Cl				
$e + Cl \longrightarrow e + Cl$	Elastic scattering	0	(Wang et al., 2013)	–
$e + Cl \longrightarrow Cl^+ + 2e$	Ionization	12.99	(Hayes et al., 1987) (Ali and Kim, 2005)	–
$e + Cl \longrightarrow Cl^* + e$	Excitation (see table 3.3)	–	–	–
Electron detachment from Cl^-				
$e + Cl^- \longrightarrow Cl + 2e$	Detachment by electron	3.4	(Fritioff et al., 2003)	–
$e + Cl^- \longrightarrow Cl^+ + 3e$	Detachment by electron	28.6	(Fritioff et al., 2003)	–
$Cl^- + Cl_2 \longrightarrow Cl + Cl_2 + e$	Detachment by Cl_2	3.61	(Huq et al., 1984)	TRF[a]
$Cl^- + Cl \longrightarrow Cl_2 + e$	Detachment by Cl	1.13	See text	CMF
Recombination				
$e + Cl_2^+ \longrightarrow 2Cl$	Dissociative recombination	0	(Zhang et al., 2011)	–
$Cl_2^+ + Cl^- \longrightarrow 3Cl$	Mutual neutralization	0	(Church and Smith, 1978)	CMF
$Cl^+ + Cl^- \longrightarrow 2Cl$	Mutual neutralization	0	(Church and Smith, 1978)	CMF
Charge exchange				
$Cl^+ + Cl \longrightarrow Cl + Cl^+$	Charge exchange	0	(Subramonium, 2003)	CMF
$Cl_2^+ + Cl_2 \longrightarrow Cl_2 + Cl_2^+$	Charge exchange	0	(Subramonium, 2003)	CMF
$Cl^+ + Cl_2 \longrightarrow Cl + Cl_2^+$	Charge exchange	0	(Španěl et al., 1993)	CMF
$Cl^- + Cl \longrightarrow Cl + Cl^-$	Charge exchange	0	(Karmohapatro, 1965)	TRF[b]
$Cl_2^+ + Cl \longrightarrow Cl_2 + Cl^+$	Charge exchange	1.52	See text	TRF[b]
Fragmentation				
$Cl_2^+ + Cl_2 \longrightarrow Cl_2 + Cl + Cl^+$	Fragmentation	3.52	See text	CMF
Scattering				
$Cl_2 + Cl_2 \longrightarrow Cl_2 + Cl_2$	Scattering	0	See text	TRF[a]
$Cl + Cl_2 \longrightarrow Cl + Cl_2$	Scattering	0	See text	TRF[a]
$Cl + Cl \longrightarrow Cl + Cl$	Scattering	0	See text	TRF[b]
$Cl_2^+ + Cl_2 \longrightarrow Cl_2^+ + Cl_2$	Scattering	0	See text	CMF
$Cl^+ + Cl_2 \longrightarrow Cl^+ + Cl_2$	Scattering	0	See text	CMF
$Cl^- + Cl_2 \longrightarrow Cl^- + Cl_2$	Scattering	0	See text	TRF[a]

[a] Cl_2 molecule as the target.
[b] Cl atom as the target.

Table 3.2: The electron impact electronic, rotational and vibrational excitations of Cl_2 molecule with the threshold energies, released energies and references for the cross sections.

Excited state	Thresh. [eV]	Released [eV]	Ref.
$J > 0$	0.01	–	(Christophorou and Olthoff, 1999)
$v = 1$	0.07	–	(Kolorenč and Horáček, 2006)
$v = 2$	0.14	–	(Kolorenč and Horáček, 2006)
$v = 3$	0.21	–	(Kolorenč and Horáček, 2006)
$1\ ^3\Pi_u$	3.24	0.76	(Rescigno, 1994)
$1\ ^1\Pi_u$	4.04	1.56	(Rescigno, 1994)
$1\ ^3\Pi_g$	6.23	3.75	(Rescigno, 1994)
$1\ ^1\Pi_g$	6.86	4.38	(Rescigno, 1994)
$1\ ^3\Sigma_u^+$	6.80	4.32	(Rescigno, 1994)
$2\ ^1\Pi_u$	9.22	6.74	(Rescigno, 1994)
$1\ ^1\Sigma_u^+$	9.32	6.84	(Rescigno, 1994)

3.1 Reaction set

The reaction set for the chlorine discharge incorporated in the oopd1 code is given in tables 3.1 – 3.3. The reaction set is mainly based on the reaction set of a chlorine discharge gathered for an earlier global model calculation (Thorsteinsson and Gudmundsson, 2010a). In addition, we include reactions in chlorine discharge which have counterpart reactions in an oxygen discharge (Gudmundsson et al., 2013) due to similar electronegative properties of oxygen and chlorine. This reaction set includes electron impact ionization, dissociation, detachment processes, recombination between positive and negative ions, charge exchange, scattering between heavy particles and fragmentation, which is currently the most comprehensive reaction set among all simulation codes for a chlorine discharge.

3.2 Cross sections

After the reaction set is determined, we search for the cross section data for each reaction from the literature. The cross sections for all the reactions are shown in figures 3.1 – 3.8. The cross sections are used in the Monte Carlo collision process to determine the collision type for

Table 3.3: The electron impact excitations of Cl atom with the threshold energies and references for the cross sections.

Excited state	Thresh. [eV]	Ref.
4s	9.1	(Ganas, 1988)
5s	11.4	(Ganas, 1988)
6s	12.1	(Ganas, 1988)
4p	10.5	(Ganas, 1988)
5p	11.8	(Ganas, 1988)
3d	11.2	(Ganas, 1988)
4d	12.0	(Ganas, 1988)
5d	12.4	(Ganas, 1988)

particles. Since for one specific reaction, there may be more than one work giving the cross section, the rules of choosing cross section for each reaction in our work are as follows:

(I) If the cross section has been measured by experiments, we will use this experimentally measured data directly.

(II) If the cross section has never been determined experimentally, we will use the theoretically calculated cross section.

(III) If the cross section has never been measured or theoretically calculated, we will use the rate coefficient for the reaction to estimate the cross section. But this method will introduce some deviation since the rate coefficient is obtained by assuming Maxwellian distribution for electrons, which is not valid in the real discharge.

(IV) If the cross section has never been measured or theoretically calculated and the rate coefficient has never been measured, we will use the cross section for the corresponding reaction in oxygen discharge since oxygen and chlorine are both electronegative gases and have somewhat similar characteristics.

After all the cross sections are obtained, we extrapolate them to 10^4 eV assuming the dependence of the cross section on the energy to be $\sigma \propto \mathcal{E}^{-1/2}$ or $\mathcal{E}^{-1}$ according to the physics of the process as discussed by Lieberman and Lichtenberg (2005).

For electrons colliding with Cl_2 molecules, the main processes are elastic scattering in which

the electron momentum is changed, and inelastic processes such as dissociation and ionization in which the electron momentum and energy are both changed. The cross sections for electron impact collisions with the Cl_2 molecule have been comprehensively reviewed by Christophorou and Olthoff (1999), who also provide other fundamental data for the Cl_2 molecule. More recently, Gregório and Pitchford (2012) presented a set of cross sections for electron scattering from the ground state Cl_2 molecules in the energy range from 0.01 to 100 eV. This cross section was based on the theoretical work of Rescigno (1994) and extrapolation to low electron energies based on the recommendations given by Christophorou and Olthoff (1999). Additionally, we have extrapolated this cross section to 10^4 eV assuming $\sigma \propto \mathcal{E}^{-1/2}$ (Lieberman and Lichtenberg, 2005). Ionization of the Cl_2 molecule can occur in a number of ways, but since we only take into account singly ionized particles and non-vibrationally excited ground state molecules, our scope tightens to the non-dissociative ionization,

$$e + Cl_2 \longrightarrow Cl_2^+ + 2e,$$

and two dissociative ionization processes,

$$e + Cl_2 \longrightarrow Cl + Cl^+ + 2e \text{ (dissociative single ionization)}$$

$$e + Cl_2 \longrightarrow 2Cl^+ + 3e \text{ (dissociative double ionization),}$$

for the Cl_2 molecule. Among the three ionization processes, non-dissociative ionization of Cl_2 to form Cl_2^+, with a threshold energy of roughly 11.47 eV (Wise et al., 1995), was found to be the dominant process in the entire range of impact energies (Basner and Becker, 2004). The cross section for non-dissociative ionization is taken from the measurement of Basner and Becker (2004). The cross sections for dissociative single and double ionization, with threshold energy of 15.7 $\pm$ 0.3 eV and 31.13 eV (Christophorou and Olthoff, 1999), respectively, are obtained

through multiplying the branching ratio given by Calandra et al. (2000) by the cross section used for the non-dissociative ionization. These three ionization cross sections have a similar form to the Thomson ionization cross section for atoms such that σ falls proportional to $1/\mathcal{E}$ for $\mathcal{E} \gg \mathcal{E}_{\text{thr}}$ where $\mathcal{E}_{\text{thr}}$ is the threshold energy (Lieberman and Lichtenberg, 2005). Following this, we extrapolate these cross sections to 10^4 eV. For the dissociative attachment from the ground state Cl_2 molecule, the cross section is compiled from two cross sections. For energies above 0.2 eV, we use the cross section measured by Kurepa and Belić (1978) after increasing its absolute value by 30 % to give agreement with electron swarm data (Christophorou and Olthoff, 1999). The cross section measured by Ruf et al. (2004) is used at lower energies, describing the behavior near zero energy in detail. The threshold energy is nearly zero and the incident electron surrenders its energy to the Cl_2 molecule to form Cl_2^- which consequently dissociates to form the fragments Cl and Cl^-. The electron transition is assumed to be rapid on a nuclear timescale, and the energy of the ejected fragments can be calculated by applying the Frank-Condon principle. The potential energy for the Cl + Cl^- pair is assumed to be the difference between the dissociation energy of Cl_2 and the electron affinity of Cl, which is 1.13 eV below the ground state potential for Cl_2. This energy difference plus the incident electron energy, $\mathcal{E}_{\text{inc}}$ + 1.13 eV, is divided between the fragments. The cross section for polar dissociation, with a threshold energy of 11.9 ± 0.2 eV (Christophorou and Olthoff, 1999), is taken from the work by Golovitskii (2000). The cross sections for electron scattering, the three electron impact ionization processes, dissociative attachment and polar dissociation are shown in figure 3.1.

All electronic excitations for the Cl_2 molecule appear to be dissociative, so the dissociation of the Cl_2 molecule is treated as an excitation of the Cl_2 molecule, which subsequently breaks into fragments, i.e., e + $Cl_2 \longrightarrow Cl_2^* + e \longrightarrow Cl + Cl + e$. The electron transition is assumed to be rapid on a nuclear timescale. The cross sections for the electronic excitations of Cl_2 are taken from the theoretical work of Rescigno (1994). The excitation to the five lowest states ($1\ ^3\Pi_u$, $1\ ^1\Pi_u$, $1\ ^3\Pi_g$, $1\ ^1\Pi_g$ and $1\ ^3\Sigma_u^+$) all lead to dissociation into the ground state Cl + Cl

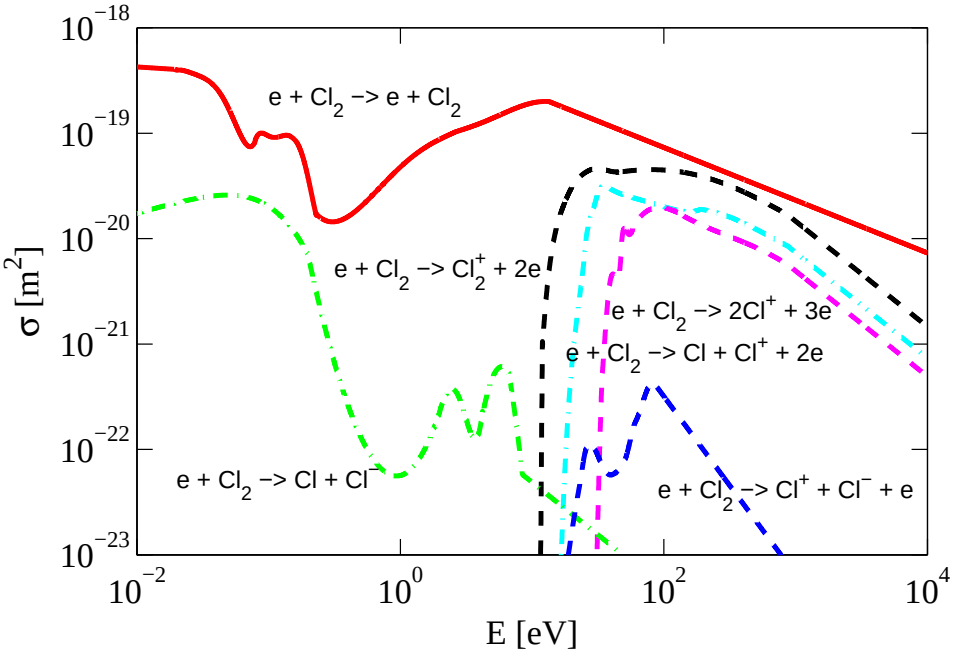

Figure 3.1: The cross sections for electron scattering, electron impact ionization processes, dissociative attachment and polar dissociation of the chlorine molecule.

(Peyerimhoff and Buenker, 1981), and the released energy to each pair of heavy fragments is the difference between the threshold energy of the excitation and the potential of the ground state Cl + Cl or 2.48 eV (Christophorou and Olthoff, 1999). As to the two higher excited levels, 2 $^1\Pi_u$ and 1 $^1\Sigma_u^+$, which are the optically allowed Rydberg states with a significant dissociation energy (Rescigno, 1994), we treat them the same as the above five dissociation processes, with ground state Cl + Cl as the final products. The cross sections for electron impact electronic excitations of Cl_2 molecule leading to dissociation are listed in table 3.2 and shown in figure 3.2.

The vibrational and rotational excitations of the Cl_2 molecule are included to serve as energy loss mechanism for electrons and are also listed in table 3.2. These processes only serve to consume electron energy and the vibrationally and rotationally excited states are assumed to return instantaneously to the ground state. Rotational excitation has been found to be relatively unimportant while vibrational excitations are found to greatly influence the shape of

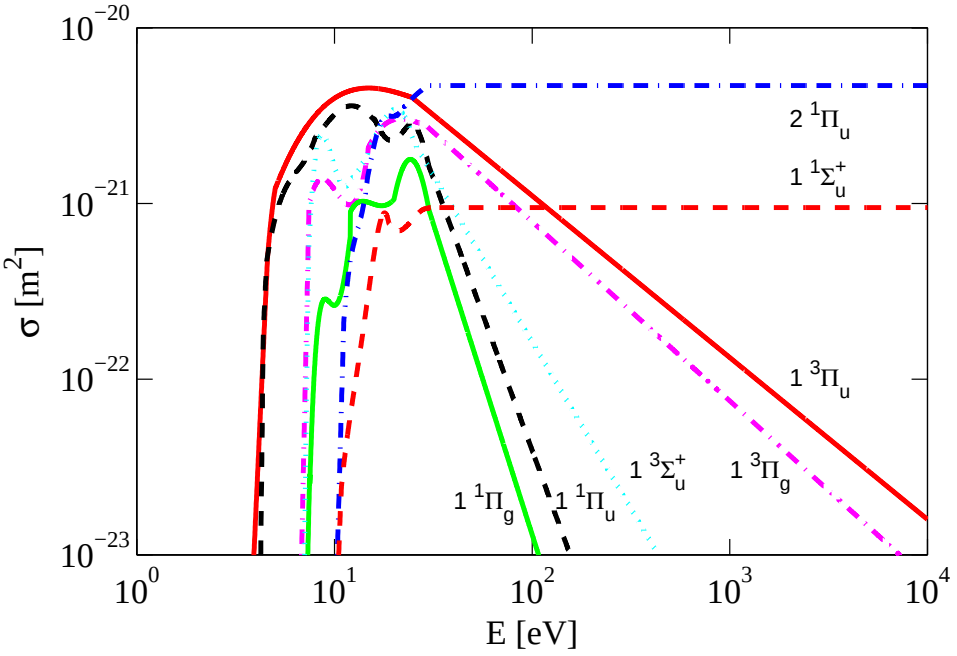

Figure 3.2: The cross sections for electron impact electronic excitations of chlorine molecule leading to dissociation.

the EEDF in oxygen discharges (Vahedi and Surendra, 1995). The cross section for rotational excitation is a compilation of the calculated data from 0.01 to 2 eV (Kutz and Meyer, 1995) and experimentally measured data from 2 to 100 eV (Gote and Ehrhardt, 1995), which is then extrapolated to 10^4 eV assuming the dependence to be $1/\mathcal{E}$ (Lieberman and Lichtenberg, 2005). The cross sections for electron impact rotational and vibrational excitations of Cl_2 molecule contributing to energy loss are shown in figure 3.3. The electron impact electronic, rotational and vibrational excitations of Cl_2 molecule included are all listed in table 3.2.

The cross section for elastic scattering of electrons off of the Cl atom is obtained from the recent calculation by Wang et al. (2013) and we extrapolate it to 10^4 eV. The cross section for electron impact ionization of ground state Cl atom, with a threshold energy of 12.99 eV (Wise et al., 1995), is taken from the measurement of Hayes et al. (1987) and then extended to higher energies based on the cross section calculated by Ali and Kim (2005), which has

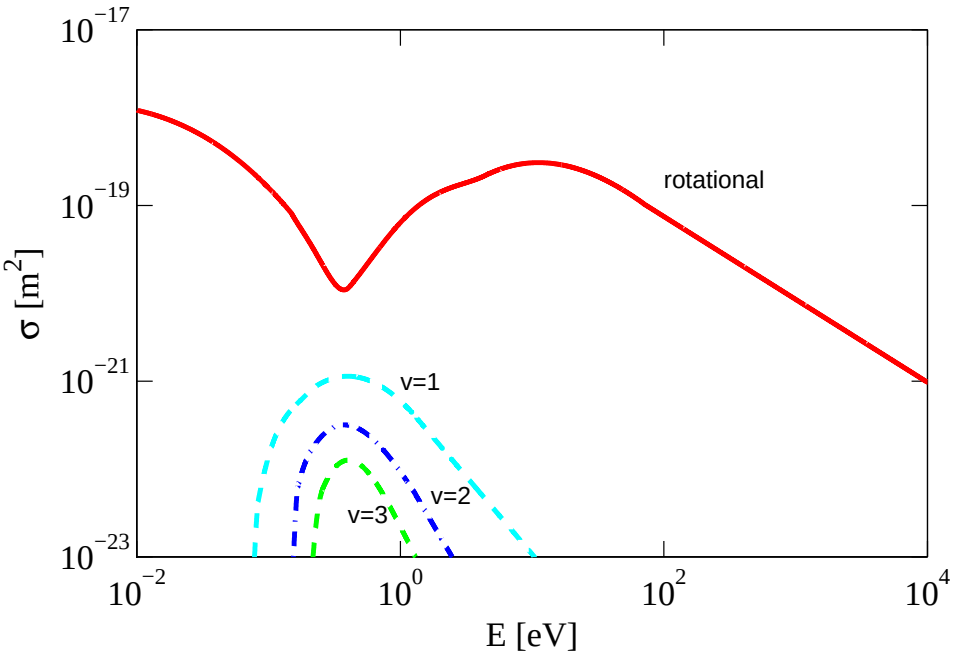

Figure 3.3: The cross sections for electron impact rotational and vibrational excitations of Cl_2 molecule contributing to energy loss.

almost the same value as the measured cross section at 200 eV (Hayes et al., 1987). This cross section is a typical Thomson cross section, which reaches its maximum value for $\mathcal{E} = 2\mathcal{E}_{\text{thr}}$ and falls proportional to $\mathcal{E}^{-1}$ for $\mathcal{E} \gg \mathcal{E}_{\text{thr}}$ (Lieberman and Lichtenberg, 2005). Since none of the lowest excited states of the Cl atom are metastable, electron impact excitations of Cl atom are incorporated to only account for collisional energy loss and these excited states are assumed to return instantaneously to the ground state Cl. These excited states are listed in table 3.3. The cross sections for elastic scattering off of the Cl atom and electron impact excitations and ionization of the Cl atom are shown in figure 3.4.

The cross sections for electron impact detachment of single and double electrons from Cl^-, with a threshold energy of 3.4 eV (Chanson et al., 2012) and 28.6 eV (Fritioff et al., 2003) respectively, are taken from the measurements by Fritioff et al. (2003). For detachment by the Cl_2 molecule, we use the cross section measured by Huq et al. (1984), and the threshold of this

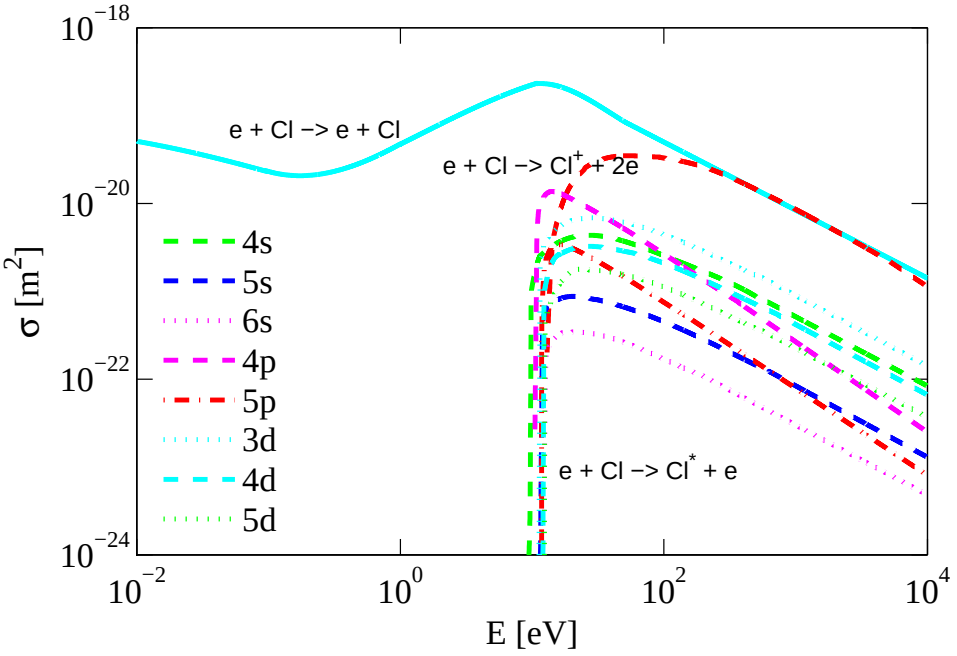

Figure 3.4: The cross sections for elastic scattering off of the Cl atom and electron impact excitation and ionization of the Cl atom.

reaction is assumed to be the electron affinity of Cl, 3.61 eV. The cross section for detachment by the Cl atom has not been measured nor calculated yet. Since the potential difference between ground state Cl_2 and Cl + Cl^- pair is 1.13 eV and this reaction is the inverse reaction for dissociative attachment, we assume this process to have a threshold energy of 1.13 eV. The cross section is assumed to be given by

$$\sigma = \sigma_0 \left(1 - \frac{\mathcal{E}_{\text{thr}}}{\mathcal{E}}\right) \tag{3.1}$$

where $\sigma_0 = 1.09 \times 10^{-19}$ m^2, which is the cross section for $O^- + O \longrightarrow O_2 + e$ above 0.184 eV used by Gudmundsson et al. (2013). The cross sections for detachment by electrons, Cl_2 molecules and Cl atoms are shown in figure 3.5.

The cross section for dissociative recombination is taken from the calculation by Zhang et al. (2011). For mutual recombinations and most charge exchange reactions, the cross sections

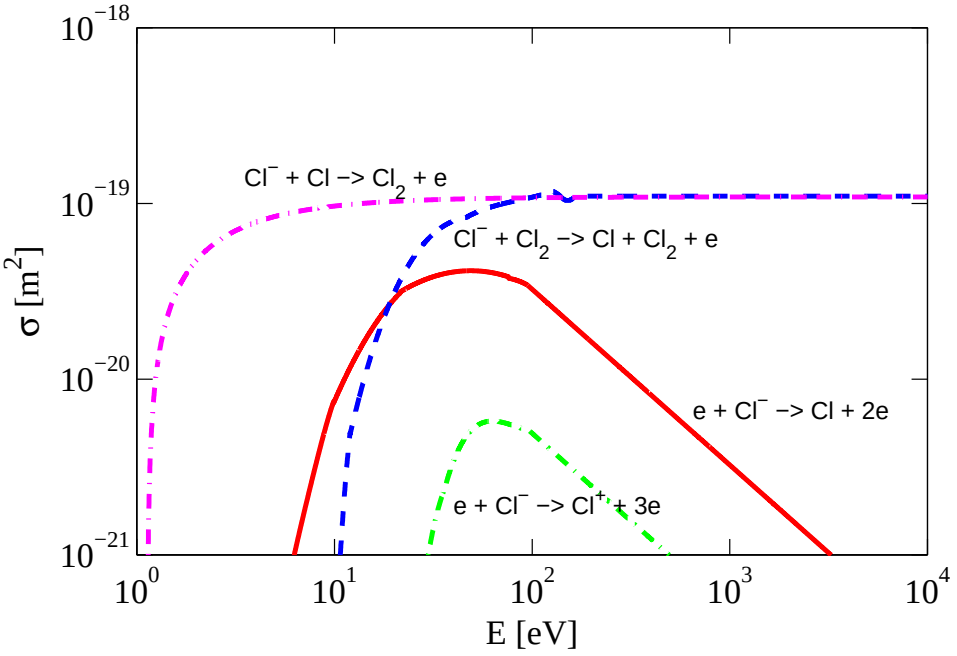

Figure 3.5: The cross sections for detachment by electrons, Cl_2 molecule and Cl atom.

are obtained from the rate coefficients using the relation $\sigma = k/(2e\mathcal{E}/m)^{1/2}$, where k is the rate coefficient of the reaction and m is the reduced mass of the reactants (Lieberman and Lichtenberg, 2005). The rate coefficient for mutual neutralization of Cl^- and Cl_2^+ is measured at 300 K to be 5.00×10^{-14} m^3/s (Church and Smith, 1978) and we have modified it to depend inversely on the square root of the collision energy, or $k = 5.00 \times 10^{-14}(300/T_g)^{1/2}$ m^3/s according to Lieberman and Lichtenberg (2005). Since a rate coefficient has never been determined specifically for the mutual neutralization of Cl^- and Cl^+, it is generally assumed to be equal to the rate coefficient for mutual neutralization of Cl^- and Cl_2^+ (Rogoff et al., 1986; Lee and Lieberman, 1995; Kim et al., 2005; Thorsteinsson and Gudmundsson, 2010a). The cross sections for dissociative recombination and mutual neutralization are shown in figure 3.6.

Both resonant and non-resonant charge exchange are included in the reaction set. The

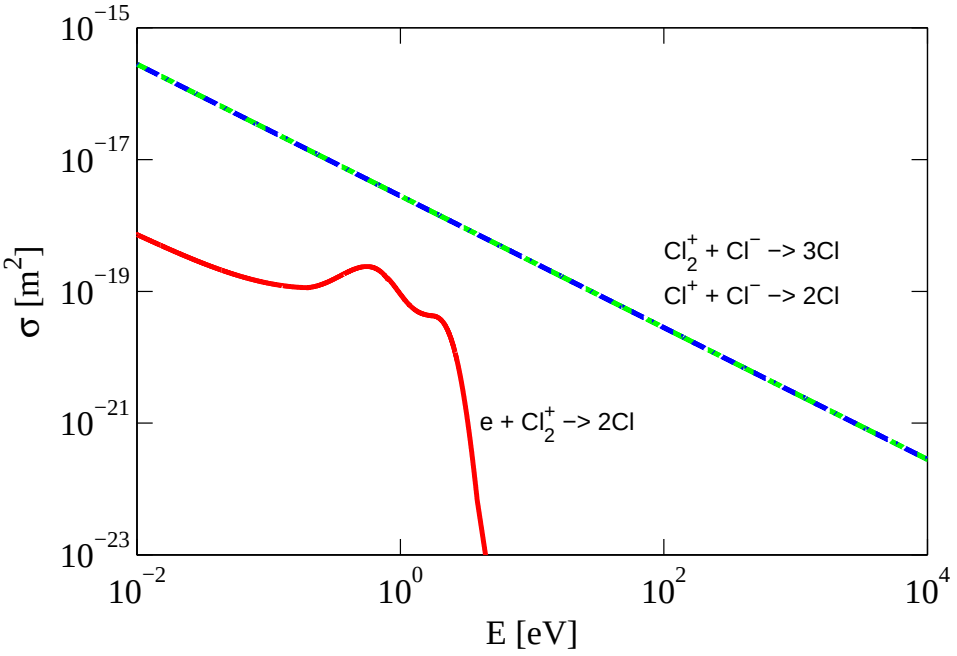

Figure 3.6: The cross sections for dissociative recombination and mutual neutralization.

charge exchange between Cl^+ ion and Cl atom,

$$Cl^+ + Cl \longrightarrow Cl + Cl^+,$$

has a rate coefficient $k = 1 \times 10^{-15}$ m^3/s (Subramonium, 2003). The charge exchange between Cl_2^+ ion and Cl_2 molecule,

$$Cl_2^+ + Cl_2 \longrightarrow Cl_2 + Cl_2^+,$$

has a rate coefficient $k = 0.8 \times 10^{-15}$ m^3/s (Subramonium, 2003). The charge exchange between Cl^+ ion and Cl_2 molecule,

$$Cl^+ + Cl_2 \longrightarrow Cl + Cl_2^+,$$

has a rate coefficient $k = 5.40 \times 10^{-16}$ m^3/s at 300 K measured by Španěl et al. (1993). While,

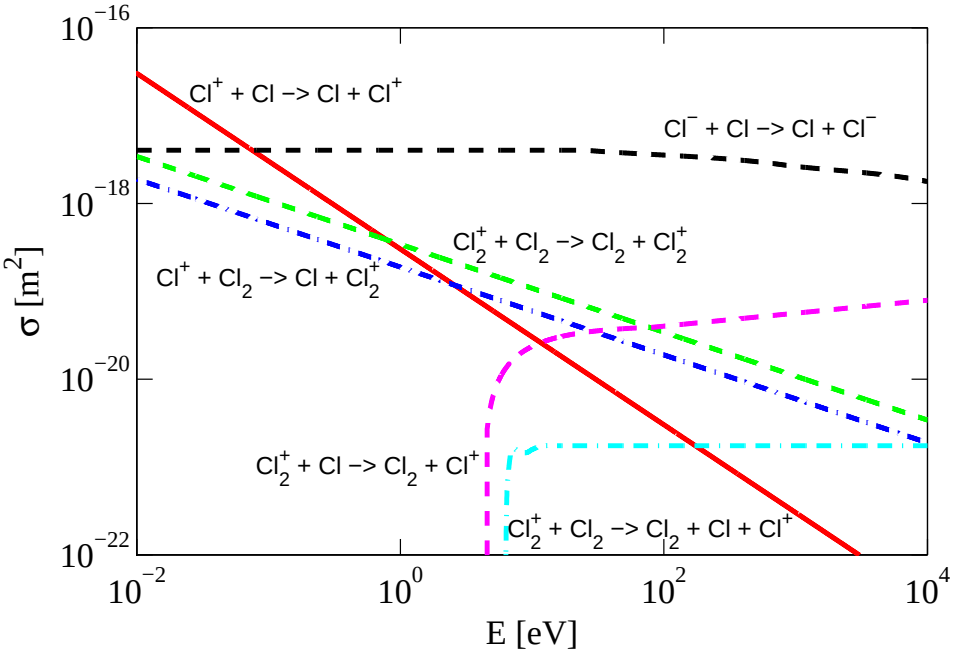

Figure 3.7: The cross sections for charge exchange and fragmentation reactions.

for the charge exchange between Cl^- ion and Cl atom,

$$Cl^- + Cl \longrightarrow Cl + Cl^-,$$

we create a fit to the cross section calculated by Karmohapatro (1965). For the charge exchange between Cl_2^+ ion and Cl atom,

$$Cl_2^+ + Cl \longrightarrow Cl_2 + Cl^+,$$

the cross section is assumed to be the same as the cross section for the corresponding reaction in oxygen, $O_2^+ + O \longrightarrow O_2 + O^+$, measured by Stebbings et al. (1963), except changing the threshold to 1.52 eV, which is the difference between the ionization threshold of Cl and Cl_2. High-energy Cl_2^+ ions can collide with Cl_2 molecules and fragment into Cl^+ and Cl,

$$Cl_2^+ + Cl_2 \longrightarrow Cl_2 + Cl^+ + Cl$$

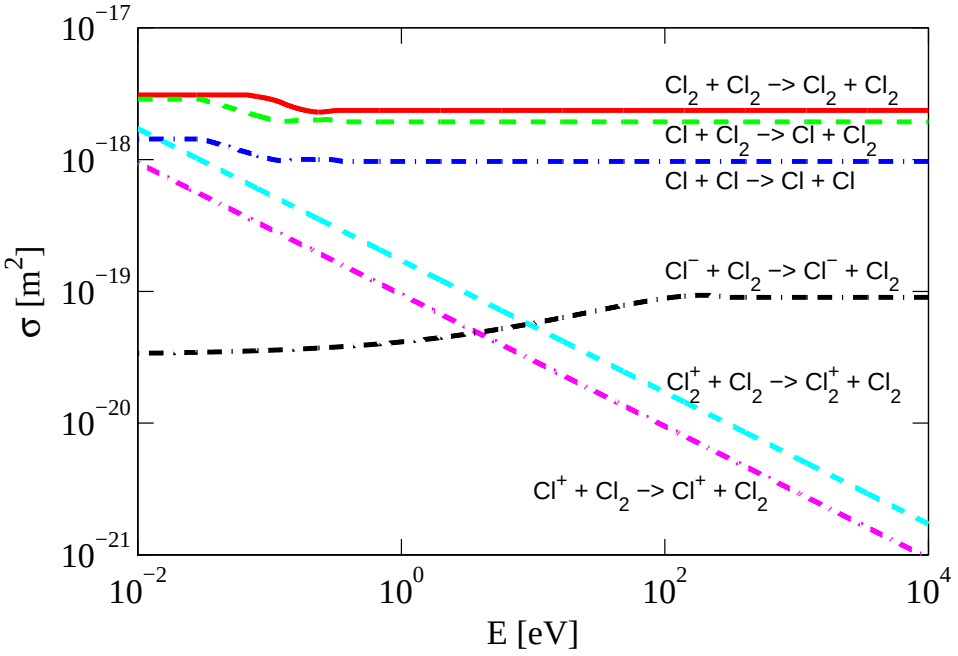

Figure 3.8: The cross sections for elastic scattering between the heavy particles.

for which the threshold is assumed to be the potential energy required to form Cl^+ + Cl pair or 3.52 eV. We assume the cross section for this reaction to be the same as that for the fragmentation of O_2^+ into O^+ and O by O_2 measured by Moran and Roberts (1968) except changing its threshold to 3.52 eV. The cross sections for all charge exchange and fragmentation reactions are shown in figure 3.7.

All the considered heavy-particle scattering reactions are listed in table 3.1. We assume that the scattering of Cl_2 molecule by Cl_2 molecule behaves the same way as the scattering of O_2 molecule by O_2 molecule and use the cross section measured by Brunetti et al. (1981). Scattering of Cl atom by Cl_2 molecule is assumed to behave like the scattering of O atom by O_2 molecule and the cross section measured by Brunetti et al. (1981) is used. Scattering of Cl atom by Cl atom is assumed half of the cross section for the scattering of O atom by O_2 molecule. The cross section for the scattering of Cl_2^+ off of Cl_2 and Cl^+ off of Cl_2 are assumed to be half of the cross section for the charge exchange between Cl_2^+ and Cl_2 and between Cl^+

and Cl_2, respectively. The cross section for the scattering of Cl^- off of Cl_2 is assumed to be the same as the corresponding reaction in oxygen discharge, $O^- + O_2 \longrightarrow O^- + O_2$, and the same cross section measured by Muschlitz (1959) is used. The cross sections for elastic scattering between the heavy particles are shown in figure 3.8.

The reason why we distinguish charge exchange and elastic scattering between ions and neutrals in table 3.1 is according to Cramer (1959) and Lieberman and Lichtenberg (2005). Seen from the experimental values for resonant charge exchange and elastic scattering of noble gas ions, e.g., Ar^+ (Cramer, 1959), He^+ and Ne^+ (Lieberman and Lichtenberg, 2005), in their parent gases, the cross section for elastic scattering, σ_s, is different from the cross section for charge exchange, σ_{cx}, and σ_s is approximately half of σ_{cx} in the measured energy range from 10 to 400 eV. Based on this, we distinguish charge exchange and elastic scattering in our reaction set and assume the cross section for the scattering of Cl_2^+ off of Cl_2 and Cl^+ off of Cl_2 to be half of the cross section for the charge exchange between Cl_2^+ and Cl_2 and between Cl^+ and Cl_2, respectively. The processes are indeed treated differently in the code. The charge exchange is basically a transfer of the charge and can thus create high-energy neutrals while the scattering involves changes in both velocity and direction of the species.

Some cross sections are plotted in center of mass frame (CMF) and some are plotted in target rest frame (TRF) in the cited papers shown in table 1, so we plot the cross sections in figures 3.1 – 3.8 and keep them identical to the cross sections in the cited papers. Thus, the cross sections for reactions plotted in figures 3.1 – 3.8 are in the same scale and the same frame with the cross section plotted in the cited papers in which these cross sections are measured or calculated. Even though the cross sections shown in figures 3.1 – 3.8 are plotted in different frames, in the simulation we transform all the cross sections to TRF and the computational processes are conducted under the same frame.

Chapter 4

Single-frequency capacitively coupled chlorine discharge

Here we explore the spatial variation of plasma kinetics and parameters in a single-frequency CCP driven by either a voltage source or a current source. Since capacitively coupled discharges are usually driven by either a voltage source or a current source, we explore these two regimes in section 4.2 and section 4.3, respectively. The discussion of the voltage driven discharge has been published in a paper by Huang and Gudmundsson (2013) and the discussion of the current driven discharge is discussed in another paper (Huang and Gudmundsson, 2014a).

4.1 Comparison with measurements

Before we explore the kinetics of a capacitively coupled chlorine discharge, we compare the simulation results with experimental measurements of the electron density, the plasma impedance and phase angle found in the literature to demonstrate the validity of the simulation code.

Comparison with measurements of electron density

Ono et al. (1992) determined the atomic concentration versus pressure for a capacitively coupled chlorine discharge in the pressure range 30 – 600 mTorr assuming neutral gas temperature of 500 K. The alumina covered aluminum electrodes were 22 cm in diameter with a separation of 4 cm and a microwave interferometer was used to monitor the plasma electron density. According to the measurements, the Cl fraction, $n_{\mathrm{Cl}}/n_{\mathrm{g}}$ (n_{Cl} is the density of Cl atoms and n_{g} is the gas density), increases with decreasing pressure from 0.27 % to 0.72 % while the electron and Cl atom density have a steady increase with increasing operating pressure. In our simulation, we assume Cl_2 molecules and Cl atoms to be the background gas, maintaining a constant and uniform density in the discharge area, with thermal equilibrium at $T_{\mathrm{g}} = 500$ K. The density of Cl_2 molecules and Cl atoms and the applied rf voltage, V_{rf}, are obtained from the measurements of Ono et al. (1992), and the input parameters for the simulations are listed in table 4.1. First we compare the experimentally measured electron density with the simulation results assuming the secondary electron emission coefficient, γ_{se}, to be fixed at 0 and 0.3 and the comparison is shown in figure 4.1. We see that when $\gamma_{\mathrm{se}} = 0$, the measured electron density is about two times higher than the simulation results. When we set $\gamma_{\mathrm{se}} = 0.3$, the measured electron density is comparable to the simulation result, but lower than the simulated electron density below 100 mTorr and higher than the simulated value above 100 mTorr. Thus, this mismatch is probably due to the secondary electrons which can actually affect the discharge. Secondary electrons have been found to affect the electron density and as the ratio of the electric field over the gas density, E/n, decreases within 10^3 Td, the secondary electron emission due to the bombardment of ions increases (Phelps and Petrović, 1999). According to this we allow the secondary electron emission coefficient to vary within reasonable range from 0.15 to 0.45 in the simulation in order to fit the simulation results to the experimental values. Figure 4.1 shows that our simulation can actually predict the electron density in the discharge by adjusting the secondary electron emission coefficient within a reasonable range.

Table 4.1: The input parameters for the simulations which are used to compare with the experimental measurements by Ono et al. (1992).

p [mTorr]	V_{rf} [V]	$n_{\mathrm{Cl}}/n_{\mathrm{g}}$ [%]	γ_{se}
30	625	0.72	0.15
45	580	0.60	0.18
80	510	0.56	0.27
100	485	0.54	0.30
200	400	0.54	0.35
300	350	0.40	0.42
500	320	0.30	0.45

The reason why we use secondary electron emission coefficient as a fitting parameter in the above comparison is as follows. We intend to compare our simulation results with experimental measurements to demonstrate the validity of our code. However, not all the experimental parameters are given by Ono et al. (1992) and the secondary electron emission coefficient is usually not reported even though it can actually play a role in the discharge. Due to the lack of data, we did not consider the secondary electrons at first and run the simulations with $\gamma_{\mathrm{se}} = 0$. The obtained simulation results for electron density are of the same magnitude with the experimental measurements, but lower than the measurements by a factor of two to three. We suppose that this mismatch is possibly caused by the secondary electrons. In order to make our simulation results match the measurements better, we have taken the secondary electrons into consideration. We firstly assumed the secondary electron emission coefficient, γ_{se}, to be a constant or 0.3. The simulation results became quite comparable to the measurements, but still had some mismatch. Afterwards, we allow γ_{se} to decrease with increasing E/n and vary within a reasonable range so as to get an excellent match between the simulation results and measurements. Although the choice of γ_{se} is from try-and-error test and seemingly intuitive, the general trend for γ_{se} has been reported by Phelps and Petrović (1999), who found that the electron yield per Ar^+ ion incident on the clean metal surface decreases with increasing E/n within 10^3 Td. Sahni and Lanza (1976) also reported similar variation of electron emission coefficient with E/n or E/p. Thus, we show that by tuning some parameters, our simulation

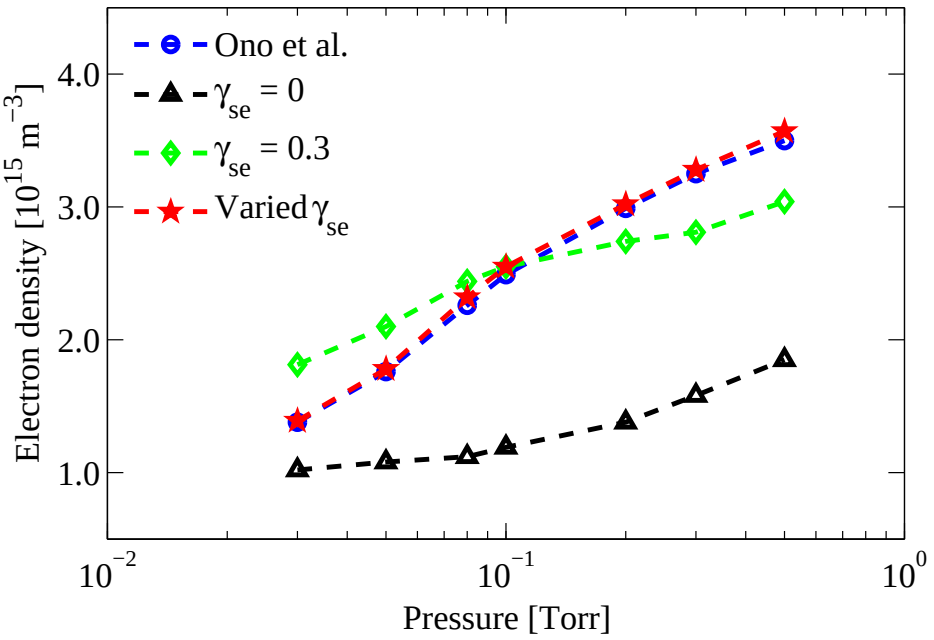

Figure 4.1: Comparison of electron density between the experimental measurements by Ono et al. (1992) and our simulation results with fixed (0 and 0.3) and varied (0.15 – 0.45) γ_{se}.

results can fit well with the measurements and figure 4.1 actually shows the process in which we tried to make our simulation results approach the measurements by Ono et al. (1992). Admittedly, we notice the influence of secondary electrons in this section. We will explore the effect of secondary electrons in detail in subsequent studies in section 4.3.

Comparison with measurements of plasma impedance

Bose (1995) measured the rf voltage, rf current, phase angle and plasma impedance using impedance and power meters placed directly on the powered electrode. The experiments were performed in a single wafer parallel-plate diode etcher consisting of two equal parallel electrodes with a radius of 10.16 cm. The top electrode was powered by an rf generator up to 1000 W at 13.56 MHz with the bottom electrode grounded. The electrode spacing was fixed at 2 cm and the flow rate was 100 sccm for Cl_2. We simulate the experiments using

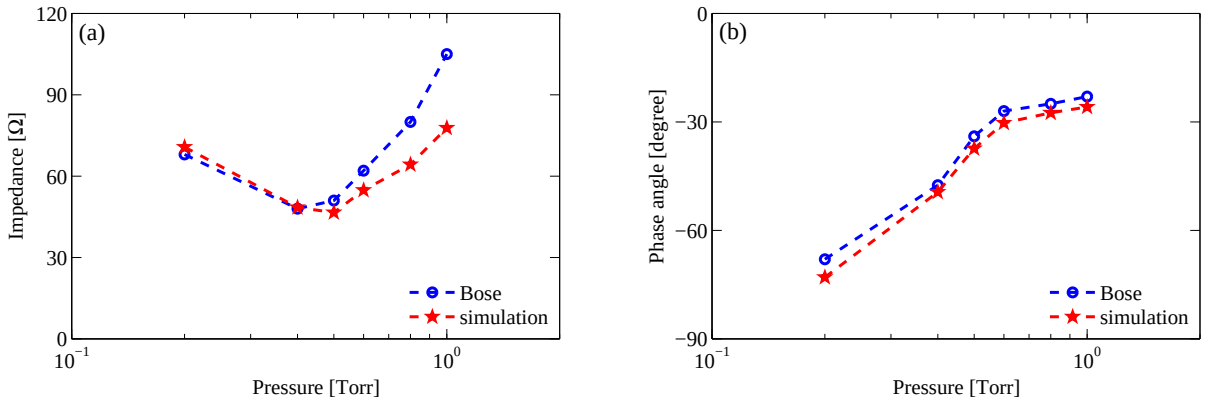

Figure 4.2: Comparison of the (a) impedance and (b) phase angle between the experimental measurements of Bose (1995) and our simulation results.

the same rf voltage applied to the electrodes in the experiments and the simulations cover the pressure range 0.2 – 1 Torr. When γ_{se} is varied in the simulation, the obtained impedance and phase angle almost remain invariant, which is consistent with the judgement by Bose that the secondary electron emission has little influence on the impedance measurement and power deposition in the explored pressure range (Bose, 1995). So here we assume γ_{se} to be 0 for all the explored cases. Similar variations of the impedance and the phase angle with the pressure are obtained through our simulation. The comparisons between the experimental measurements and simulation results are shown in figures 4.2(a) and (b) for the impedance and phase angle, respectively. The error between the simulation results and experimental measurements is within 20 %. The discrepancy between the simulation results and experimental measurements of the impedance above 600 mTorr shown in figure 4.2(a) is possibly due to the fact that the discharge becomes highly collisional and shifts from capacitive to capacitive-resistive discharge, resulting in the loss of accuracy for the simulation results. As our subsequent explorations will not cover the pressure range above 600 mTorr, we have gained enough confidence that the oopd1 code can provide reasonable and satisfying predictions of the plasma behavior and discharge parameters.

4.2 Voltage driven capacitively coupled chlorine discharge

For the voltage driven capacitively coupled chlorine discharge, we assume that the plasma is sustained between two parallel plates as shown in figure 2.7. One of the electrode is driven by a voltage source

$$V(t) = V_{\mathrm{rf}} \sin(\omega \mathrm{t}),$$

where V_{rf} is the amplitude of the applied rf voltage. We assume the discharge to be operated at a single frequency of 13.56 MHz and the applied voltage $V_{\mathrm{rf}} = 222$ V with a large capacitor of 1 F in series. We also assume the electrodes to be circular with a diameter of 14.36 cm and a separation of 4.5 cm. These are the same parameters as explored for the capacitively coupled oxygen discharge by Gudmundsson et al. (2013). Due to the large ratio of transverse to longitudinal dimension of the discharge area, the oopd1 code with one spatial dimension description for the system and three velocity components for the dynamics of the particles suffices.

The CCPs are usually operated over a wide range of gas pressures. Processes which require nearly collisionless sheath and high energy for the bombarding ions will be operated at pressures below 50 mTorr, while processes which require high radical density and low electron temperature will be operated at higher pressures. As we can expect, the plasma parameters such as the density of electrons and ions and the electron heating mechanism actually vary over this large pressure range. Therefore, we vary the discharge pressure from 5 to 100 mTorr to explore the dependence of the plasma parameters on discharge pressure. As the neutral gas density is much higher than the density of charged particles, the neutral species are assumed to be the background with uniform density in space and a Maxwellian velocity distribution at room temperature ($T_{\mathrm{g}} = 300$ K). In addition, according to the measurements in a chlorine discharge by Donnelly and Malyshev (2000), the neutral chlorine gas temperature is 300 K when the absorbed power is lower than 50 W in the pressure range 1 – 100 mTorr. Our simulations are

conducted within the pressure range 5 – 100 mTorr with the absorbed power lower than 10 W, so 300 K is a reasonable choice for the gas temperature. As the Cl atom hits the electrode, it is assumed to return as a thermal Cl atom with a 50 % probability or two Cl atoms can return as a thermal Cl_2 molecule with a 50 % probability. The measured Cl recombination coefficient for anodized Al is about 0.2 at room temperature and for stainless steel about 0.85 at room temperature but drops to 0.3 at 350 K (Kota et al., 1998), so a recombination coefficient of 0.5 is a reasonable choice.

The dynamics of the charged particles (electrons, Cl_2^+, Cl^+ and Cl^- ions) are followed as well as the Cl atoms and Cl_2 molecules when their energy exceeds 1 eV. We choose a subcycling factor of 16 for the heavy particles and assume parabolic initial density profile (Kawamura et al., 2000). The time step Δt and grid spacing Δx are chosen to resolve the electron plasma frequency, ω_{pe}, and the electron Debye length, λ_{De}, of the low-energy electrons following equations (2.8) and (2.9). The simulation grid is uniformly distributed between the two electrodes, creating 1000 cells in the discharge area. Since the density of Cl_2^+ and Cl^- ions are higher than the density of electrons and Cl^+ ions by two or three orders of magnitude, the weighting factor is allowed to vary to accommodate comparable number of simulation particles for each species. The weighting factor is set to be 10^8 for Cl_2 molecules, Cl atoms, Cl_2^+ and Cl^- ions, 10^7 for electrons and 10^6 to 10^7 for Cl^+ ions. These correspond to about 20 – 40 Cl^+ ions and electrons and 200 – 400 Cl_2^+ and Cl^- ions per cell. The secondary electron emission coefficient is assumed to be 0 for the 4 cases explored here and more detailed investigation on the influence of γ_{se} will be carried out in section 4.3. The electron time step is chosen to be 3.68×10^{-11} s. The simulation is run for 11×10^6 time steps or 5500 rf cycles.

4.2.1 Effect of gas pressure

We run 4 cases for the capacitively coupled chlorine discharge from 5 to 100 mTorr to explore the dependence of the plasma parameters on the discharge pressure. The simulation results

are numerically listed in table 4.2 and graphically shown in figures 4.3 – 4.9. The fraction of Cl atoms shown in table 4.2 is higher than the experimentally reported value by Ono et al. (1992) in table 4.1. We suppose that the ratio of Cl atoms reported by Ono et al. (1992) as listed in table 4.1 underestimates the actual ratio of Cl atoms in the discharge. We also admit that the ratio of Cl atoms calculated by the global model in our work as listed in table 4.2 probably overestimates the actual ratio of Cl atoms in the discharge somewhat. We explain the underestimation and overestimation as follows.

(I) Ono et al. (1992) have reported the fraction of Cl atoms in a capacitively coupled chlorine discharge to be lower than 1 % within the pressure range 30 – 500 mTorr as listed in table 4.1. However, another experiment conducted by Aydil and Economou (1992b) showed that the fraction of Cl atoms is about 2 – 3 % at 300 – 500 mTorr with the absorbed power at 20 – 80 W. In addition, Lee et al. (1997) developed a global model for a capacitively coupled chlorine discharge and the fraction of dissociation of chlorine molecules is found to be about 6 % at 100 mTorr. Also, Malyshev and Donnelly (2000) explored an inductively coupled chlorine discharge and the the fraction of Cl atoms is measured to be about 5 % at 10 W in the pressure range 1 – 20 mTorr. More recently, according to the measurements in an inductively coupled chlorine discharge by Booth et al. (2012), the ratio of Cl density is found to be a few percentages in the pressure range 2 – 50 mTorr when the absorbed power is lower than 100 W. Therefore, even though the above discharges are under various conditions, we can infer that the measurements of the fraction of Cl atoms by Ono et al. (1992) underestimate the actual value and the reasonable value for the fraction of Cl atoms should be a few percentages.

(II) The estimation for chlorine atoms using global model is somewhat a limitation in our work. In our simulation, we need to rely on the global model to estimate the density of Cl atoms as the component of the background gas. However, the global model is mainly developed for modeling ICP rather than CCP discharge. The proportion of the power dissipated in electron heating in ICP is much higher than in CCP. Therefore, the use of global model will lead to

Table 4.2: The simulation results for the 4 cases in order to explore the dependence of the plasma parameters in the center of the discharge on the pressure. (n_e, n_{Cl^+}, n_{Cl^-} and α_0 denote the density of electrons, Cl^+ and Cl^- ions and the electronegativity in the center of the discharge, respectively.)

p [mTorr]	P_{abs} [W]	n_{Cl}/n_g [%]	$\overline{V}_s$ [V]	n_e [$10^{14}m^{-3}$]	n_{Cl^+} [$10^{13}m^{-3}$]	n_{Cl^-} [$10^{16}m^{-3}$]	T_{eff} [eV]	α_0
5	0.66	5.3	103.6	2.04	13.6	1.37	3.75	67
10	0.87	6.4	102.1	2.81	10.4	2.61	3.35	93
50	2.57	8.9	98.7	4.74	5.21	6.56	3.21	138
100	7.80	13.8	96.8	6.51	7.84	10.2	3.04	157

some overestimation of the density of Cl atoms in the discharge, especially when in the low pressure range. As the pressure decreases to below 10 mTorr, most of the power is dissipated in ion heating in the sheath region for accelerating ions to the surface. Meanwhile, the sheath region expands to an extent that the discharge area is apparently divided into one bulk region and two sheath regions. Thus, the assumption in the global model that the power is uniformly distributed in the discharge area is not completely true so that estimation for the density of Cl atoms will be larger than the actual value by some amount. This overestimation will have some influence on the density of Cl^+ but little influence on the density of electrons, Cl_2^+ and Cl^- ions. The influence of this overestimation will not be explored in our study.

Figures 4.3 and 4.4(a) show the effective electron temperature profile and the EEPF in the center of the discharge, respectively. As the pressure increases from 5 to 100 mTorr, the effective electron temperature in the center of the discharge, T_{eff}, decreases as seen in figure 4.3. The decrease of the effective electron temperature with increasing pressure is also observed in an electropositive helium discharge by Godyak et al. (1992) and in an electronegative chlorine discharge by Franz (2005). Godyak et al. suppose that the increase in the gas pressure inhibits the fast electrons from reaching the center of the discharge and diminishes the efficiency of the heat transfer from the plasma boundaries to the center of the discharge (Godyak et al., 1992). We note that there is indeed a depletion of high-energy electrons with increasing discharge pressure as seen in the EEPF in figure 4.4(a). Franz assumes that the effective

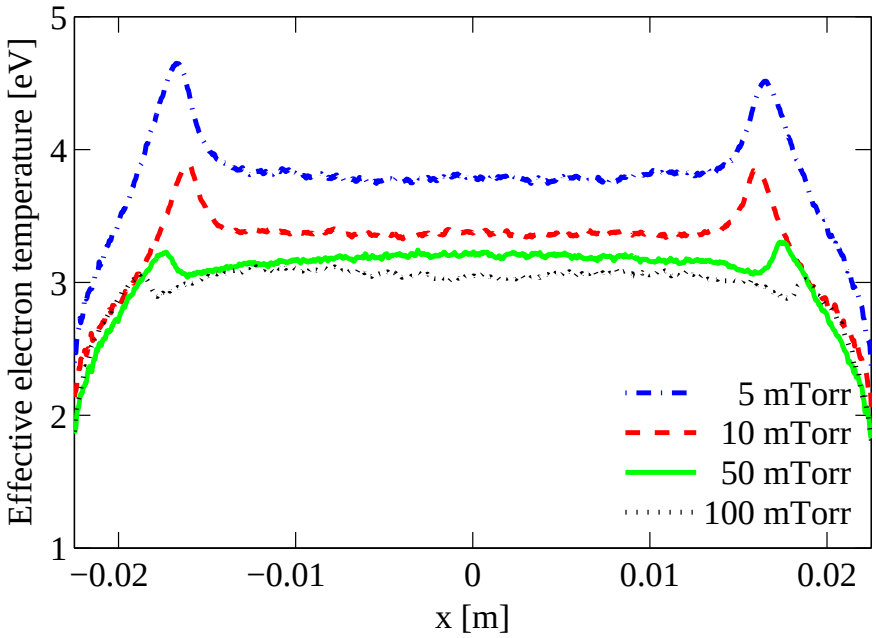

Figure 4.3: The effective electron temperature profile for a parallel plate capacitively coupled chlorine discharge with a gap separation of 4.5 cm by a 222 V voltage source at 13.56 MHz.

electron temperature is determined by the equilibrium between the creation of ions by electron impact ionization in the bulk region and the loss of ions due to diffusion at the surface, which consequently leads to the inverse dependence of the effective electron temperature on the logarithm of the discharge pressure (Franz, 2005). According to our simulation results, the electron heating rate shown in figure 4.5 increases with increasing pressure, indicating more endothermic reactions for electrons, most of which are ionization reactions and consequently generate low-energy electrons. The proportion of the low-energy electrons increases as shown in figure 4.4(a), leading to the decrease of the average electron energy and hence the effective electron temperature with increasing pressure shown in figure 4.3. There is a peak in the effective electron temperature at the bulk-sheath interface. This peak has also been observed in an oxygen discharge (Lisovskiy and Yegorenkov, 2006) and a chlorine discharge (Lymberopoulos and Economou, 1995), which coincides with the peak in the electron heating profile at the

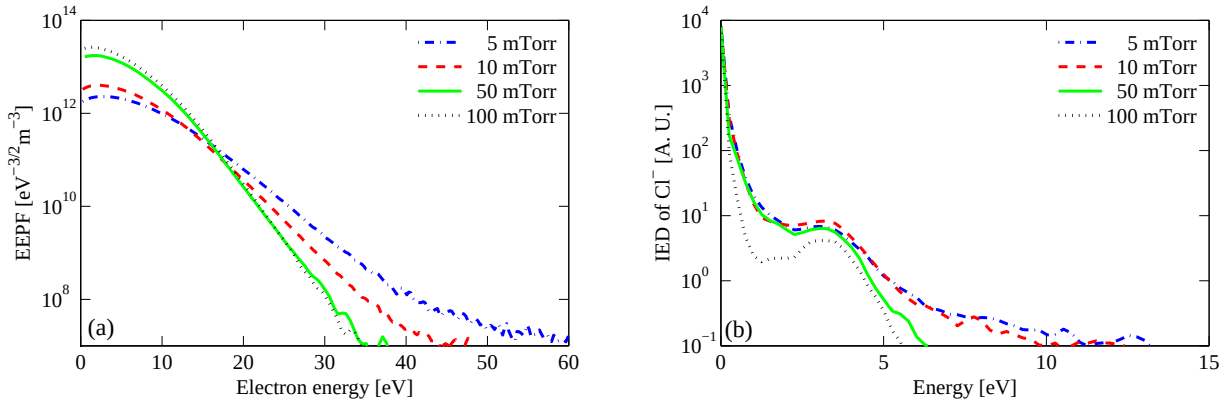

Figure 4.4: The (a) EEPF and (b) IED of Cl^- in the center of a parallel plate capacitively coupled chlorine discharge with a gap separation of 4.5 cm by a 222 V voltage source at 13.56 MHz.

bulk-sheath interface. As the electrons approach the electrode, they are repelled by the sheath potential, consequently leading to a steep drop in the effective electron temperature (Meyyappan and Govindan, 1991).

Figure 4.4(b) shows the IED of Cl^- ions in the center of the discharge. Below 1.5 eV, the IED of Cl^- has a Maxwellian profile and the effective temperature is at room temperature, i.e., 0.026 eV. However, there is a maxima or plateau area at about 3.3 eV. Similarly, the energy distribution of Cl atoms in the discharge center is also found to have a maxima at approximately the same energy value. When we switch off the resonant charge exchange between Cl^- and Cl, the maxima at 3.3 eV in the IED of Cl^- ions disappears. Therefore, this maxima is mainly due to the charge exchange between Cl^- and Cl which changes the high-energy Cl atoms to high-energy Cl^- ions.

Generally, there are two main heating mechanisms in capacitively coupled discharges: Ohmic heating due to electron-neutral collisions and stochastic heating in the sheath region due to momentum transfer from the oscillating sheath. The peaks in the electron heating rates near the bulk-sheath interface shown in figure 4.5 are mainly due to stochastic heating while the electron heating rates in the bulk region are mainly due to Ohmic heating. According to the measurements of Franz and Klick (2005) in a capacitively coupled chlorine discharge, the

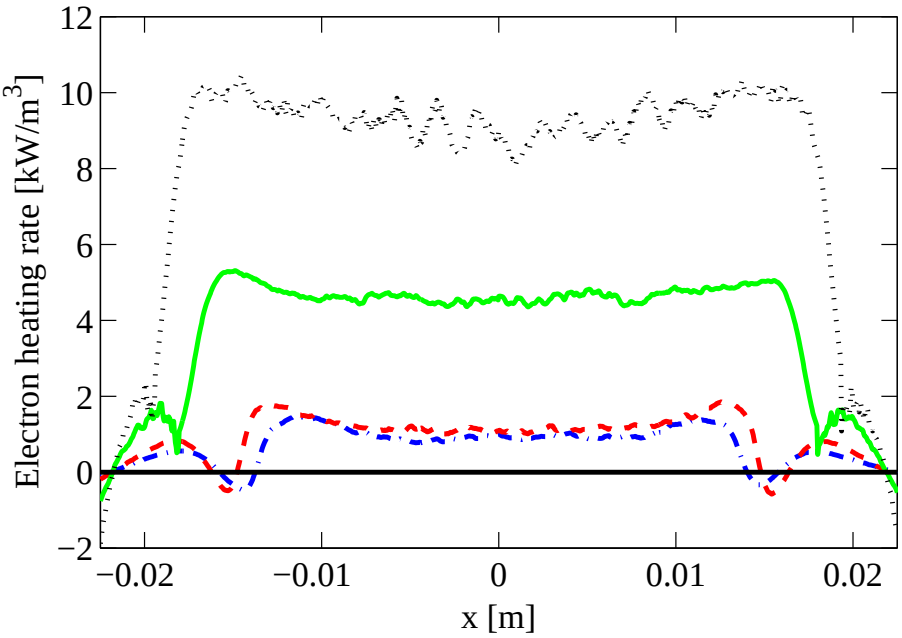

Figure 4.5: The electron heating rate profile for a parallel plate capacitively coupled chlorine discharge with a gap separation of 4.5 cm by a 222 V voltage source at 13.56 MHz. (The legend in this figure is the same as in figure 4.3.)

transition from stochastic heating to Ohmic heating occurs at about 30 – 40 mTorr and the onset of Ohmic heating appears relatively sharply in this pressure range. Figure 4.5 shows that as the pressure increases, electron heating rates in both the bulk and sheath regions increase, which indicates that Ohmic heating can be concentrated in both of these regions and this heating can actually be characterized as local heating. We do not observe a Maxwellian EEPF due to the low electron density shown as seen in table 4.2 which reduces the thermalization required for creating Maxwellian EEPF.

Figure 4.6 shows the fraction of power absorbed by electrons, Cl_2^+ and Cl^+ ions. At low pressure (below 10 mTorr), most of the power is deposited on the positive ions in the sheath region for accelerating these ions towards the electrode. The relatively small fraction of power absorbed by the electrons is distributed in the bulk and sheath region due to Ohmic heating through electron neutral collisions and stochastic heating through momentum transfer from

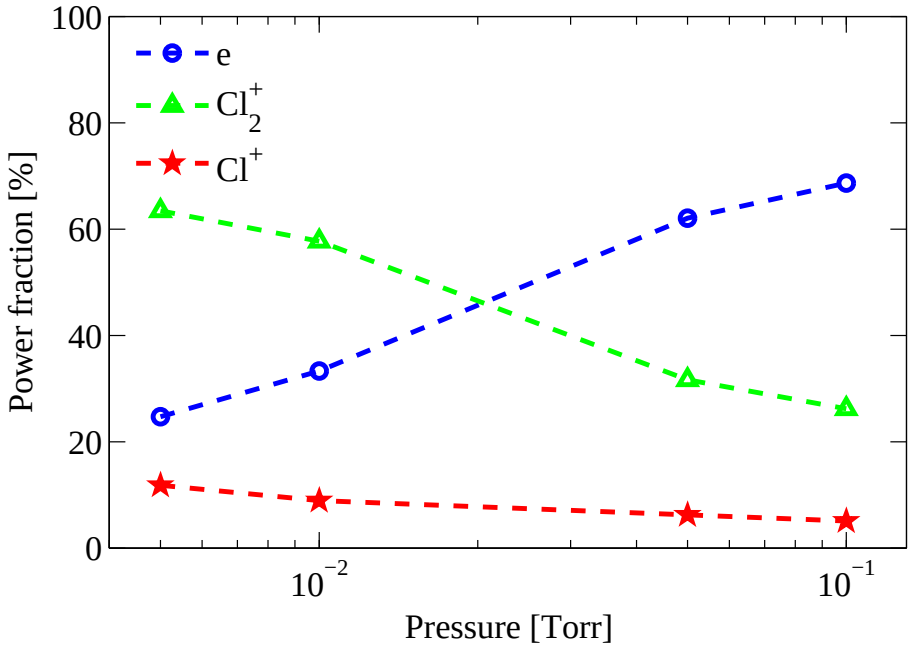

Figure 4.6: The fraction of power absorbed by electrons, Cl_2^+ and Cl^+ ions for a parallel plate capacitively coupled chlorine discharge with a gap separation of 4.5 cm by a 222 V voltage source at 13.56 MHz.

the oscillating sheath, respectively (Surendra and Graves, 1991b). The electron heating rate profile at low pressure is similar to what is observed in an electropositive argon discharge at 500 mTorr in which the Ohmic heating is comparable to the stochastic heating (Vahedi et al., 1993). At high pressure (above 50 mTorr), most of the power is deposited on the electrons in the bulk region mainly by the Ohmic heating therein. The electron heating rate profile at high pressure is similar to what is observed by a fluid model of an electronegative discharge at 500 mTorr by Oh et al. (1990) and a capacitively coupled chlorine discharge at 100 mTorr by Lymberopoulos and Economou (1994) in which the Ohmic heating dominates. The negative part in the electron heating rate at the bulk-sheath interface is mainly due to the Ramsauer minimum in the cross section for elastic scattering (Surendra and Graves, 1991a) as can be seen in figures 3.1 and 3.4. Electron cooling observed near the electrode can be ascribed to the diffusion of electrons towards the electrodes against the strong sheath fields according to

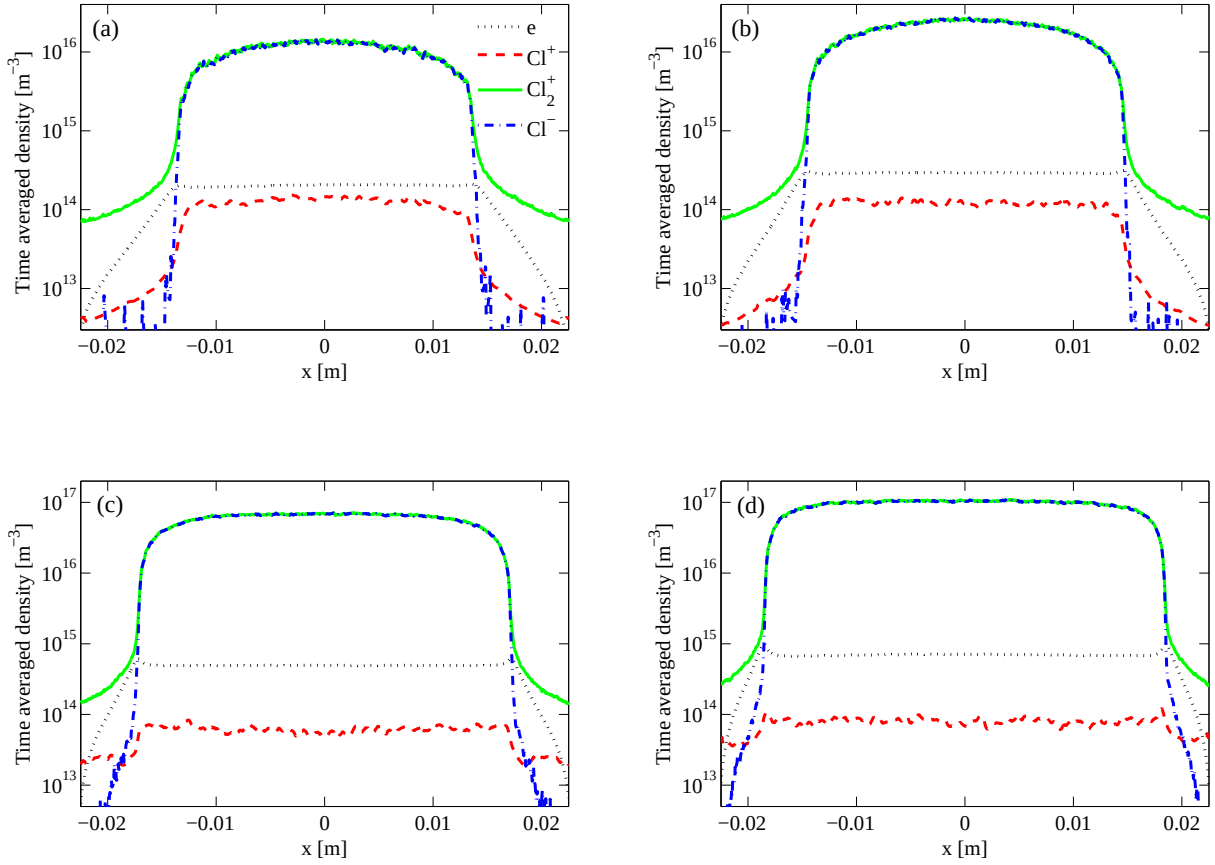

Figure 4.7: The density profile at (a) 5 mTorr, (b) 10 mTorr, (c) 50 mTorr and (d) 100 mTorr for a parallel plate capacitively coupled chlorine discharge with a gap separation of 4.5 cm by a 222 V voltage source at 13.56 MHz.

Lymberopoulos and Economou (1994). The ion heating for Cl_2^+ and Cl^+ ions is mostly deposited in the sheath region and increases steadily when approaching the electrode, which is similar to the ion heating rate for the positive ions in both the electropositive argon discharge (Vahedi et al., 1993) and electronegative discharges (Oh et al., 1990; Lymberopoulos and Economou, 1994).

As to the Cl atoms tracked in the simulation, since the density of Cl atoms is much higher than the density of charged species, not all the Cl atoms can be tracked as particles in the simulation. Therefore, we only track the fast Cl atoms with an energy higher than 1 eV, similar to the investigation on fast neutrals in an argon discharge by Wang et al. (2007). The simulation

results show that these high-energy Cl atoms have a uniform and flat density profile at about 2.5×10^{15} m^{-3} in the bulk region for the 4 explored cases. In the sheath region, the density of high-energy Cl atoms increases steadily as approaching the surface. As the pressure increases from 5 to 100 mTorr, the density of fast Cl atoms at the surface increases from about 1.3×10^{16} to 6.5×10^{16} m^{-3}.

The density profiles of charged particles for the explored 4 cases are shown in figures 4.7(a) – (d) and the values of each species in the center of the discharge are listed in table 4.2. An electronegative core and an electropositive edge are observed as seen in figures 4.7(a) – (d). In the bulk region, the Cl^- ions are confined by the ambipolar field and the density of Cl^- ions is comparable to the Cl_2^+ ions, by which the charge neutrality is assured. The electrons are restrained by the ambipolar field and have a nearly uniform density in the bulk region mainly due to the existence of the negative ions. In the sheath region, the density of Cl_2^+ ions and electrons decreases as they approach the electrodes, with almost no Cl^- ions in this area. Nearly no Cl^- ions can reach the electrode surface and be lost there. The division of the bulk and sheath region can be explicitly seen from the turning point of the electron density profile shown in figures 4.7(a) – (d) where the electron density loses its flatness and begins to fall. Similar density profile is observed and explored theoretically for an oxygen discharge and a chlorine discharge by Lichtenberg et al. (1994, 1997).

At low pressure, the profile for Cl_2^+ ions is cosine-like or parabolic since Cl_2^+ ions are lost mainly due to diffusion to the walls (Meyyappan and Govindan, 1991), which is similar to the electropositive argon discharge (Wang et al., 2011). As the pressure increases, the recombination between Cl_2^+ and Cl^- ions becomes the major source for the loss of Cl_2^+ ions and the ionization and attachment reaction rates become uniform in the bulk region. Thus, the density profile for Cl_2^+ and Cl^- ions becomes quite flat in the bulk region (Meyyappan and Govindan, 1991). Lichtenberg et al. (1997) also observed the transition from parabolic to more flattened (elliptic) density profile for Cl_2^+ and Cl^- ions due to the change in the loss mechanism for Cl_2^+ ions from

diffusion dominated to recombination dominated with increasing pressure.

As the pressure is increased, the density of electrons undergoes a slight increase. This phenomenon is also observed experimentally by Franz (2005) in a capacitively coupled chlorine discharge and in simulation by Bera et al. (2011) in a capacitively coupled oxygen discharge. Franz assumes that the pressure-induced increase of electrons is counterbalanced by the increase of dissociative attachment which is enhanced at high pressures (Franz, 2005). Bera et al. supposes that the effectiveness of the pressure-induced increase of electrons is diminished by the decrease of the effective electron temperature and consequently the ionization process is prohibited (Bera et al., 2011). According to our simulation results, figures 4.7(a) – (d) show that the density of Cl^- ions increases with increasing pressure, maintaining density level comparable to the density of Cl_2^+ ions in the bulk region, indicating that the electron impact ionization for creating Cl_2^+ ions increases almost equally with dissociative attachment for creating Cl^- ions. Also, the effective electron temperature actually shows a decrease with increasing pressure in figure 4.3 so as to suppress the ionization process and guarantee the particle balance in the discharge.

The density profile for Cl^+ ions is very different from Cl_2^+ ions. In the bulk region, the density of Cl^+ ions is uniform and maintained at very low value of about $0.5 - 1.5 \times 10^{14}$ m^{-3}, decreasing slightly with increasing pressure. Although the fraction and density of Cl atoms increase with increasing pressure, the Cl^+ ions in the bulk region still decreases since in this region the Cl^+ ions are mainly created through the electron impact ionization processes, which are suppressed by the decreased effective electron temperature at high pressure. However, at the plasma-electrode boundary, the density of Cl^+ ions increases steadily with increasing pressure, which is mainly due to the increased heavy-particle collisions for creating Cl^+ ions in the sheath region and will play a significant role in plasma processing at the surface. In the sheath region, when the pressure is below 10 mTorr, the profile for Cl^+ ions shows similar trend as Cl_2^+ ions, while when the pressure is above 50 mTorr, as approaching the electrode

from the bulk-sheath interface, the density of Cl^+ will first decrease and then become flat or even show a slight increase. Similar trend is observed for H_2^+ ions in a capacitively coupled hydrogen discharge by Longo (2006) and Diomede et al. (2005) and the strong variation of the density of H_2^+ ions in the sheath region is ascribed to the conversion from the majority H_3^+ ions to minority H_2^+ ions through the endothermic reaction, $H_3^+ + H_2 \longrightarrow H_2^+ + 3H$ (Diomede et al., 2005). O'Connell also find that the formation of H_2^+ ions in the sheath region is mainly from H_3^+ ions through collision-induced dissociation or non-resonant charge transfer (O'Connell, 2004). Accordingly, when we switch off similar endothermic reactions in the reaction set, i.e., conversions from majority Cl_2^+ ions to minority Cl^+ ions through non-resonant charge exchange and fragmentation, we find that the flatness and slight increase disappear and the density of Cl^+ ions shows the same trend as Cl_2^+ ions in the sheath region. In addition, we find that the conversion through charge exchange is the main channel for the creation of Cl^+ ions in the sheath region and the conversion through fragmentation only has slight influence due to its small cross section as seen in figure 3.7. Thus, the Cl^+ ions in the sheath region is mainly created through heavy-particle collisions including non-resonant charge exchange and the ion mean free path decreases with increasing pressure, leading to more collisional sheath and consequently more heavy-particle collisions for creating Cl^+ ions.

The electronegativity, defined by

$$\alpha_0 = n_{Cl^-}/n_e \tag{4.1}$$

is listed in table 4.2 for the center of the discharge. We can see that increasing the pressure will contribute to high electronegativity. This was also observed by Kawano et al. (2000) in a chlorine discharge and was explained by that the effect of the pressure on the density of Cl_2^+ and Cl^- ions is stronger than that on the electron density. The electronegativity for the chlorine discharge in the explored cases is much higher than the oxygen discharge observed

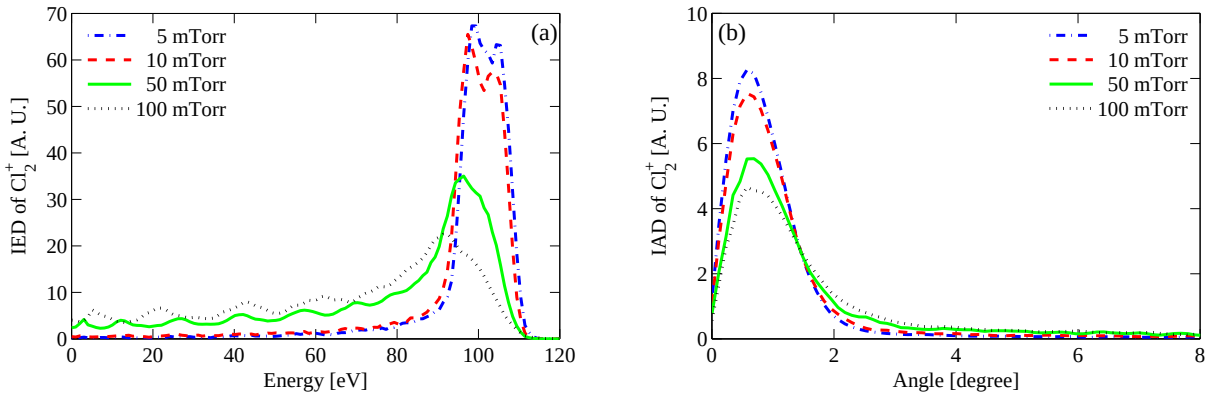

Figure 4.8: The (a) IED and (b) IAD of Cl_2^+ at the grounded electrode for a parallel plate capacitively coupled chlorine discharge with a gap separation of 4.5 cm by a 222 V voltage source at 13.56 MHz.

by Lichtenberg et al. (1994) and Gudmundsson et al. (2013) mainly because the dissociative attachment in chlorine discharge is an exothermic reaction (Gottscho and Gaebe, 1986) and has a large cross section in the low-energy range where most of the electrons are accumulated (Kurepa and Belić, 1978). The electronegativity in the discharge center for the 100 mTorr case obtained from the simulation is 157, which is comparable to the electronegativity obtained from a fluid model calculation (Meyyappan and Govindan, 1991) for a chlorine discharge operated at 300 mTorr.

Figures 4.8(a) and 4.9(a) show the IED of Cl_2^+ and Cl^+ ions hitting the grounded electrode, respectively. At low pressure, the IED of Cl_2^+ and Cl^+ ions has a bimodal structure and is centered at the average sheath potential, $\overline{V}_s$, which satisfies the relation

$$\mathcal{E}_{ion} = \overline{V}_s \approx 0.83 \times \frac{V_{rf}}{2} \tag{4.2}$$

where $\mathcal{E}_{ion}$ is the mean ion kinetic energy for ions hitting the electrode (the median of the IED). These indicate that the Cl_2^+ and Cl^+ ions travel through an almost collisionless sheath at low pressure (5 mTorr and 10 mTorr) according to the verification in an argon discharge by Wang et al. (2011). Similar IED profile indicating collisionless sheath has also been observed for O_2^+

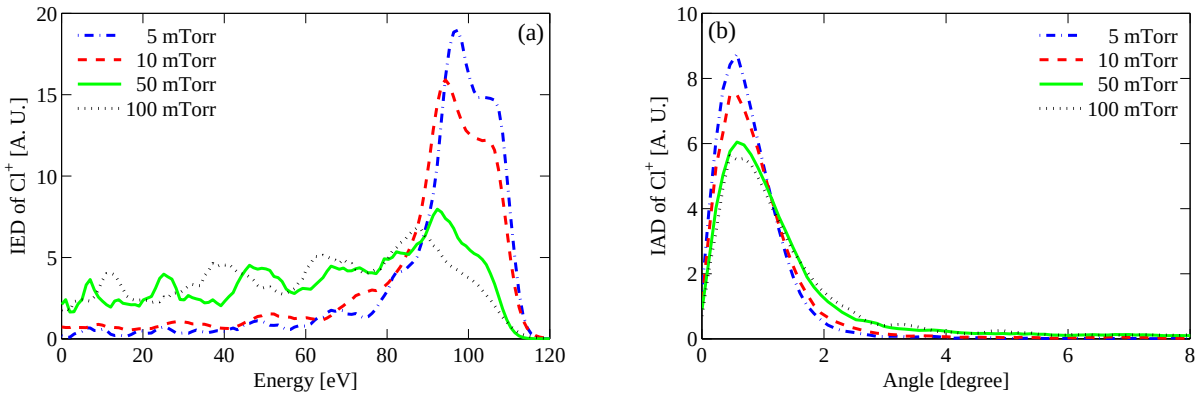

Figure 4.9: The (a) IED and (b) IAD of Cl^+ at the grounded electrode for a parallel plate capacitively coupled chlorine discharge with a gap separation of 4.5 cm by a 222 V voltage source at 13.56 MHz.

and O^+ ions in an oxygen discharge at 3 mTorr by Kratzer et al. (2001).

As the pressure is increased to above 50 mTorr, the IEDs of Cl_2^+ and Cl^+ ions become wider and shift to the low-energy region, with the proportion of ions in the low-energy region enhanced. These are mainly due to the decreased ion mean free path for the positive ions with increasing pressure, which consequently leads to more heavy-particle collisions including elastic scattering and charge exchange between neutrals and ions. As for Cl_2^+ and Cl^+ ions, resonant charge exchange and elastic scattering with neutrals will generate fast neutrals and slow thermal ions. Since these thermal ions are created inside the sheath region and thereafter accelerated by the electric field to the electrode, these ions only experience a fraction of the full sheath potential and have comparatively lower energy. Also, the charge exchange reactions lead to the formation of multi-peaks in the low-energy region and the number of multi-peaks is approximately equal to the average number of rf periods it takes an ion to cross the sheath (Kawamura et al., 1999). Similar appearance of multi-peaks with the shift of IED to the low-energy region is also observed for H_2^+ ions in a hydrogen discharge (O'Connell et al., 2007), for O_2^+ and O^+ ions in an oxygen discharge (Wild and Koidl, 1991) and for Ar^+ ions in argon discharges (Manenschijn and Goedheer, 1991; Kawamura et al., 1999; Wang, 2012). The multi-peaks in the IED of Cl^+ ions are more considerable than for Cl_2^+ ions and this is mainly due

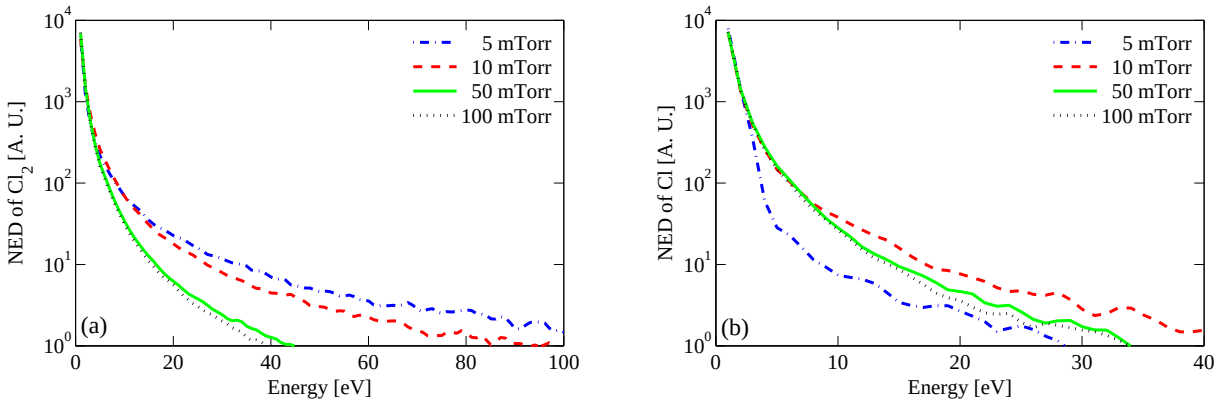

Figure 4.10: The NED of (a) Cl_2 and (b) Cl at the grounded electrode for a parallel plate capacitively coupled chlorine discharge with a gap separation of 4.5 cm by a 222 V voltage source at 13.56 MHz.

to the non-resonant charge exchange occurring in the sheath region which consumes Cl_2^+ ions and creates slow thermal Cl^+ ions and consequently enhance the multi-peaks in the low-energy region in the IED of Cl^+ ions.

Figures 4.8(b) and 4.9(b) show the IAD of Cl_2^+ and Cl^+ ions hitting the grounded electrode, respectively. In the explored pressure range most Cl_2^+ and Cl^+ ions hit the grounded electrode with a velocity almost normal to the electrode, indicating high anisotropy. Within the sheath, ions are accelerated by the electric field towards the electrode. Therefore, the IAD is highly directed towards the electrode. With increasing pressure, the proportion of ions with small angle perpendicular to the electrode decreases and the IAD extends more to the large-angle area, which are due to isotropically scattered ions by elastic scattering with neutrals in the sheath region and correspond to the shift of IED to the low-energy region as shown in figures 4.8(a) and 4.9(a). Similar variation of IED and IAD for argon and helium discharges with increasing pressure has been observed by Kushner (1985) who pointed out that the spreading of IAD has significant consequence in plasma etching since anisotropic delivery of activation energy to the surface is required to obtain vertical etches and to etches whose depth exceeds their width.

Due to the limitation of the computer, we only track the high-energy neutrals with energy higher than 1 eV. The NED of Cl_2 molecules and Cl atoms hitting the grounded electrode are

shown in figures 4.10(a) and (b), respectively. The fast neutrals are created though charge exchange and elastic scattering with positive ions. Therefore, the energy distributions are related to the ion energy distribution. Since the neutrals cannot be accelerated in the sheath region, the energy of neutrals are much lower than positive ions and most neutrals incident on the surface have energy below 10 eV. Figure 4.10(a) shows that as the pressure increases, the proportion of fast Cl_2 molecules decreases. This is because the mean free path for Cl_2 molecules decreases with increasing pressure and more collisions occur, which consequently leads to more energy loss for Cl_2 molecules. This variation is similar to the variation of the NED for Ar atoms at the surface in a dual-frequency argon discharge explored by Wang et al. (2007). Figure 4.10(b) shows that as the pressure increases from 5 mTorr to 10 mTorr, the high-energy tail of the NED for Cl atoms is enhanced due to more Cl^+ ions created in the sheath and consequently more fast Cl atoms. However, as the pressure is further increased to 100 mTorr, the high-energy tail shrinks slightly since the increase of high-energy Cl atoms is counterbalanced by the increased elastic scattering with decreasing mean free path.

4.3 Current driven capacitively coupled chlorine discharge

In the simulation of current driven SF capacitively coupled chlorine discharge, the discharge is assumed to be sustained between two parallel plates as shown in figure 2.7, one of which is subject to a current source

$$J(t) = J_{\mathrm{rf}} \sin(2\pi f t)$$

where J_{rf} is the amplitude of the current density and f is the driving frequency. The two electrodes are placed in a vacuum chamber. Feedstock chlorine gas is pumped into the chamber and excited by the electric field between the electrodes where plasmas consisting of electrons, ions and radicals are produced. The wafers to be processed are placed on one of the electrodes. We use the geometry of the GEC rf reference cell (Hargis et al., 1994; Olthoff and Greenberg,

Table 4.3: The simulation results for cases 1 – 10 in order to explore the effect of driving current, driving frequency and secondary electrons on the discharge. (n_e, n_{Cl^+}, n_{Cl^-} and α_0 denote the density of electrons, Cl^+ and Cl^- ions and the electronegativity in the center of the discharge, respectively.)

Case	J_{rf} [A/m^2]	f [MHz]	γ_{se}	P_{abs} [W]	n_{Cl}/n_g [%]	$\bar{s}_m$ [m]	T_{eff} [eV]	$\overline{V}_s$ [V]	n_e [10^{14}m^{-3}]	n_{Cl^+} [10^{14}m^{-3}]	n_{Cl^-} [10^{16}m^{-3}]	α_0
1	40	27.12	0.0	1.20	9.38	0.0046	3.60	92.1	7.20	2.05	6.01	83.5
2	20	27.12	0.0	0.43	3.80	0.0028	3.88	38.2	3.35	0.32	4.53	135
3	60	27.12	0.0	2.65	18.1	0.0057	3.09	161	13.4	7.14	6.23	46.5
4	80	27.12	0.0	4.94	26.1	0.0061	2.92	222	20.5	15.4	8.92	43.5
5	21	13.56	0.0	1.20	9.38	0.0054	3.96	112	3.11	1.01	4.18	134
6	55	40.68	0.0	1.20	9.38	0.0039	3.03	69.2	13.9	3.02	6.77	48.7
7	74	60	0.0	1.20	9.38	0.0030	2.97	50.8	17.5	2.26	8.13	46.5
8	40	27.12	0.1	1.26	10.1	0.0045	3.52	90.1	7.61	2.78	6.02	79.1
9	40	27.12	0.2	1.31	10.5	0.0044	3.43	88.3	7.91	3.61	6.05	76.5
10	40	27.12	0.4	1.40	11.2	0.0042	3.33	84.0	8.48	5.15	6.16	72.6

1995) for the discharge chamber with the diameter of the plates to be 0.102 m and the gap length between the two plates to be 0.0254 m. The diameter of the electrodes is much larger than the gap length so that a one-dimensional description suffices. The discharge pressure is assumed to be 10 mTorr. The recombination coefficient for Cl atoms at the surface is assumed to be the same as the recombination coefficient used in the voltage driven discharge in section 4.2. As a Cl atom hits the electrode, it returns as a thermal Cl atom with 50 % probability or two Cl atoms can return as a thermal Cl_2 molecule with 50 % probability. The simulation grid is uniform and consists of 1000 cells. The electron time step is chosen to be 1.84×10^{-11} s according to the stability criterion (Gudmundsson et al., 2013). The simulation is run for 5500 rf cycles for each case. The density profile and the electron heating rate profile are averaged over 54 rf cycles after the simulation runs to a stable state.

Case 1 is the basic case explored as the benchmark in this study. In case 1, the discharge is driven by a 40 A/m^2 current source at 27.12 MHz with a gap separation of 0.0254 m. The secondary electron emission coefficient is assumed to be 0.0. Both Cl_2 molecules and Cl atoms are treated as the initial background gas with uniform density in space and a Maxwellian velocity distribution at room temperature ($T_g = 300$ K). Due to the limitation of the computer, we only track the high-energy neutrals with energy exceeding 1 eV.

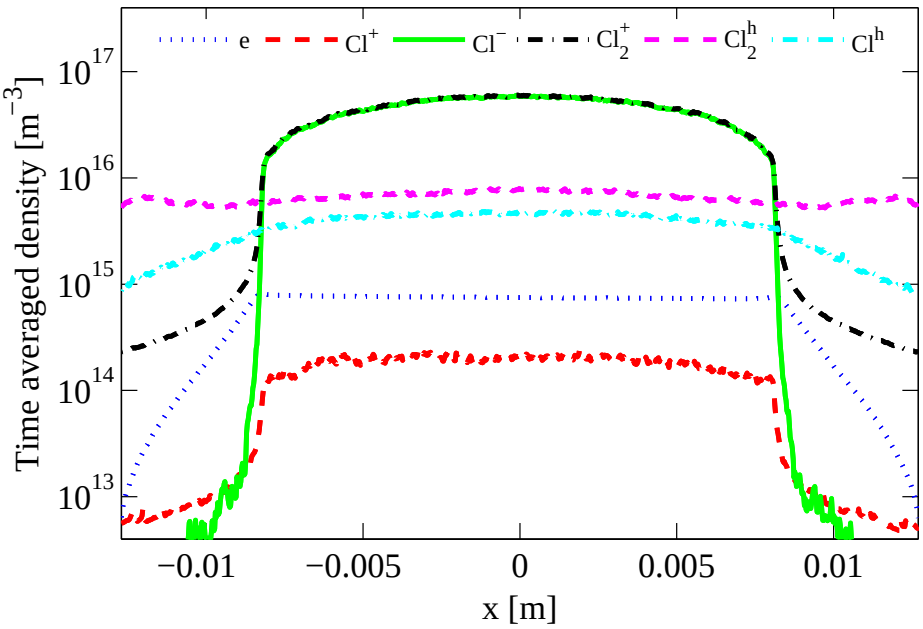

Figure 4.11: The time averaged density profile for a parallel plate capacitively coupled chlorine discharge at 10 mTorr with a gap separation of 0.0254 m by a 40 A/m^2 current source operated at 27.12 MHz. (Cl_2^h and Cl^h denote the high-energy Cl_2 molecules and Cl atoms with energy exceeding 1 eV, respectively.)

The other explored cases can be classified into 3 groups in order to explore the effect of driving current, driving frequency and secondary electrons on the discharge, respectively.

(I) In cases 2, 3 and 4, the current density is changed to 20 A/m^2, 60 A/m^2 and 80 A/m^2 respectively with other control parameters the same as in case 1.

(II) In cases 5, 6 and 7, the driving frequency is changed to 13.56 MHz, 40.68 MHz and 60 MHz, respectively. The absorbed power is maintained at 1.20 W by adjusting the current density so that the dissociation fraction of the chlorine gas remains invariant in cases 1, 5, 6 and 7. Other control parameters are the same as in case 1.

(III) In cases 8, 9 and 10, the secondary electron emission coefficient is changed to 0.1, 0.2 and 0.4 respectively with other control parameters the same as in case 1.

In the CCP discharge, the densities of radicals and charged particles and their spatial

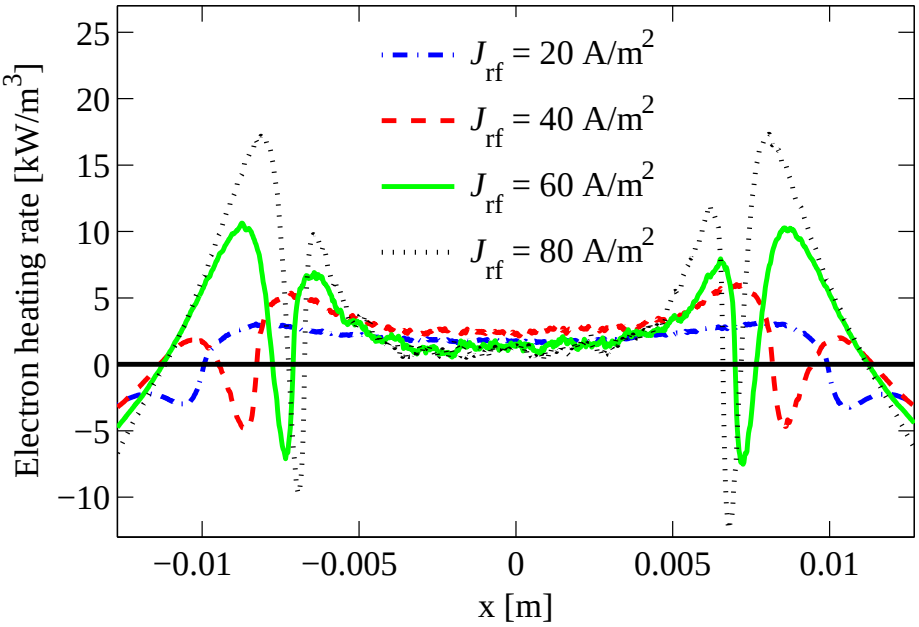

Figure 4.12: The time averaged electron heating rate profile for a parallel plate capacitively coupled chlorine discharge at 10 mTorr with a gap separation of 0.0254 m by a current source operated at 27.12 MHz.

distributions are strongly affected by the energy and density distributions of the electrons, which are the key plasma parameters in the discharge. The radicals interact with the substrate to form volatile products, thereby etching the substrate, or adsorb and react to deposit thin film. Meanwhile, the bombardment by positive ions can further enhance these processes. Therefore, the plasma parameters of interest are the effective electron temperature, the flux of radicals and ions towards the substrate, the ion energy and angular distributions at the surface, etc. These plasma parameters are critical to the etching properties in manufacturing processing and will be mainly explored in our study. The simulation results for cases 1 – 10 are listed in table 4.3 and shown in figures 4.11 – 4.25.

Figure 4.11 shows the time averaged density profile for electrons, Cl_2^+, Cl^+, Cl^-, Cl and Cl_2 in case 1. This density profile is similar to the density profile obtained through a fluid model developed for recombination dominated chlorine discharge (Franklin and Snell, 2000)

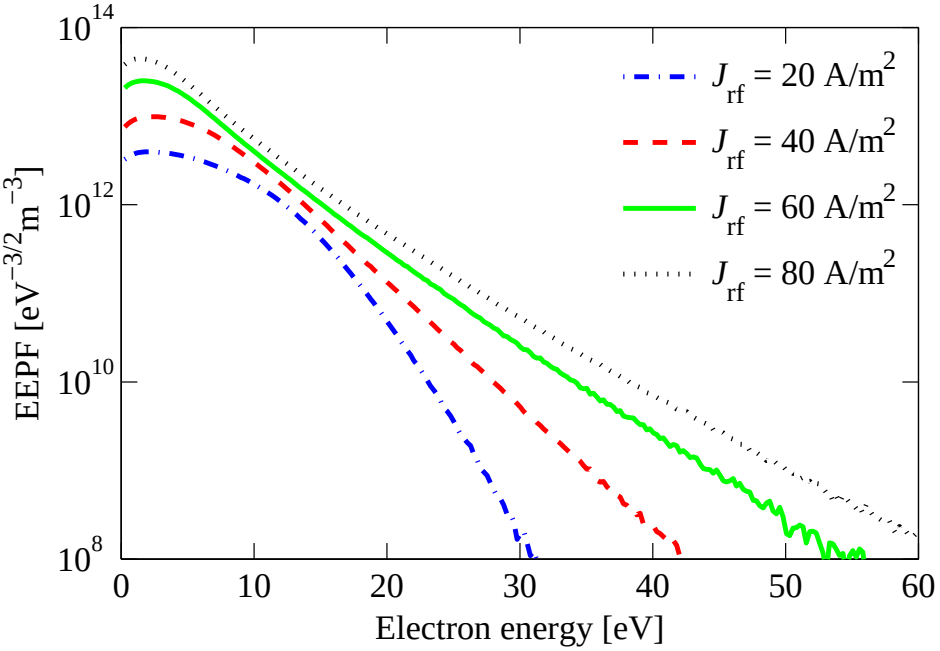

Figure 4.13: The EEPF in the center of a parallel plate capacitively coupled chlorine discharge at 10 mTorr with a gap separation of 0.0254 m by a current source operated at 27.12 MHz.

and the density profiles obtained in electronegative oxygen discharges through PIC/MCC simulations (Gudmundsson et al., 2013) and fluid model calculations (Küllig et al., 2012). In the bulk region, a high density of Cl^- ions is compared to a low electron density, which is the result of a very efficient electron impact dissociative attachment, $e + Cl_2 \longrightarrow Cl + Cl^-$. Thus, the electronegativity in the discharge center, α_0, reaches 83.5, which shows strong electronegative property of the discharge. Since the density of Cl^- ions is approximately two orders of magnitude higher than the density of electrons, the condition of quasineutrality in the plasma bulk necessitates commensurate densities of Cl_2^+ and Cl^- ions therein. The electron density in the bulk plasma is nearly flat, which is again caused by the high density of Cl^- ions. Under such condition, the electron ambipolar diffusivity is almost equal to the free electron diffusivity (Rogoff, 1985) and the high electron diffusivity promotes more uniform electron density profile. The density of Cl^+ ions is less than the density of Cl_2^+ ions by two orders of

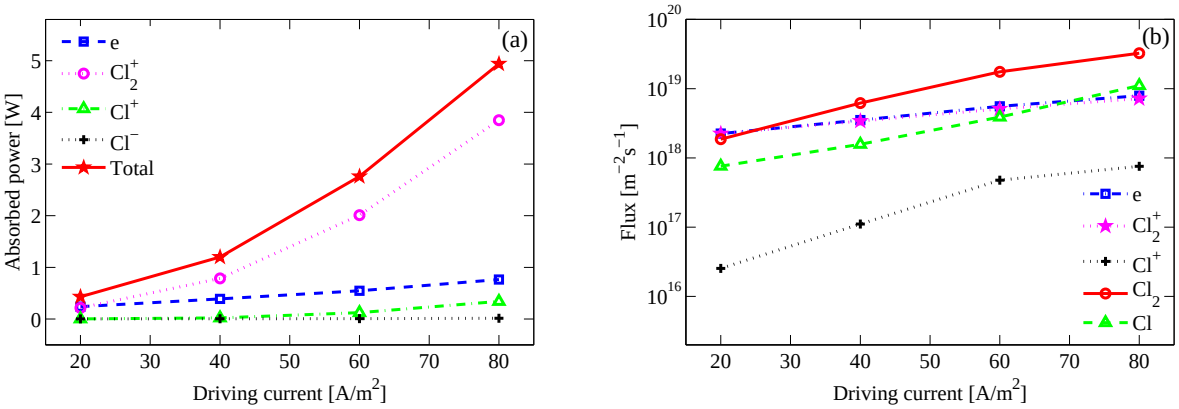

Figure 4.14: The (a) absorbed power by electrons, Cl_2^+, Cl^+ and Cl^- ions in the whole discharge volume and (b) flux of electrons, Cl_2^+ and Cl^+ ions, and high-energy ($>$ 1 eV) Cl_2 molecules and Cl atoms reaching the powered electrode for a parallel plate capacitively coupled chlorine discharge at 10 mTorr with a gap separation of 0.0254 m by a current source operated at 27.12 MHz.

magnitude and shows similar profile with the electron density in the bulk region and similar profile with the density of Cl_2^+ ions in the sheath region.

The density profiles of high-energy ($>$ 1 eV) Cl_2 molecules and Cl atoms shown in figure 4.11 are both relatively uniform in the bulk region. However, in the sheath region the density of high-energy Cl_2 molecules increases slightly as approaching the surface while the density of high-energy Cl atoms decreases by about 70 %. Since dissociative excitation of Cl_2 molecules is found to be the major source of Cl radicals, the decrease of high-energy Cl atoms is mainly attributed to decreased dissociation processes in the sheath region.

4.3.1 Effect of driving current

Cases 1 – 4 are used to explore the effect of driving current on the discharge and the results are shown in figures 4.12 – 4.17. Figure 4.12 shows the electron heating rate profile along the axis of the discharge region, which is a typical electron heating rate profile for capacitively coupled discharge and can be explicitly divided into two parts, i.e., the Ohmic heating in the bulk region due to electron-neutral collisions and the stochastic heating in the sheath region due

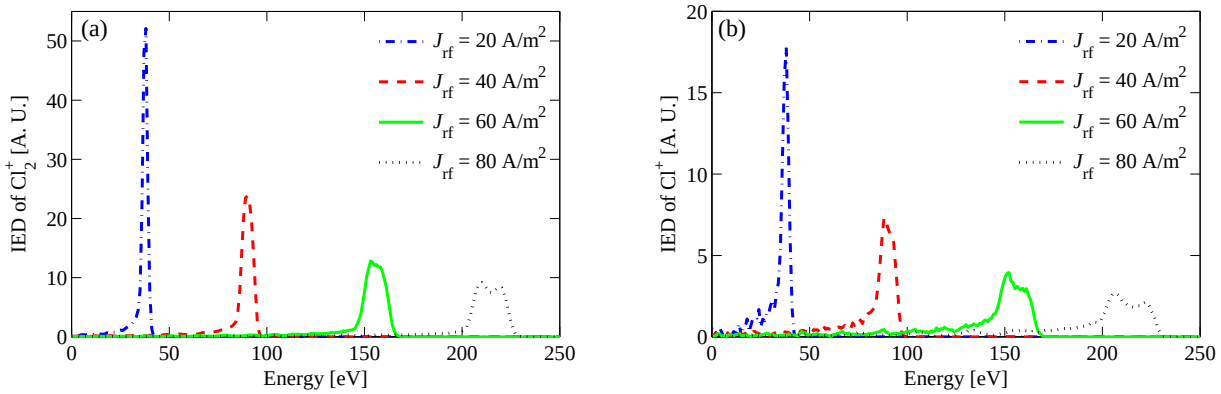

Figure 4.15: The IED of (a) Cl_2^+ ions and (b) Cl^+ ions at the powered electrode for a parallel plate capacitively coupled chlorine discharge at 10 mTorr with a gap separation of 0.0254 m by a current source operated at 27.12 MHz.

to momentum transfer by the oscillating sheath. As the driving current increases from 20 to 80 A/m^2, the profile of the EEPF in the center of the discharge shown in figure 4.13 shifts from Druyvesteyn like to Maxwellian like, and then to bi-Maxwellian. Specifically, the proportions of high-energy ($>$ 20 eV) electrons and low-energy ($<$ 5 eV) electrons both increase while the proportion of medium-energy (5 – 20 eV) electrons decreases with increasing driving current. The enhancement of high-energy electrons is attributed to the enhanced stochastic heating with increasing driving current as shown in figure 4.12. As the driving current increases, more energetic electrons with energy higher than the ionization threshold (11.47 eV for Cl_2 and 12.99 eV for Cl) are created through stochastic heating in the sheath region and then more ionization processes occur in the bulk plasma. These ionization processes convert high-energy electrons to low-energy electrons, which lead to the attenuation of medium-energy electrons and the enhancement of low-energy electrons in the EEPF with increasing driving current. Since the effective electron temperature in the discharge center, T_{eff} ($= \frac{2}{3}<\mathcal{E}>$, where $<\mathcal{E}>$ is the average electron energy), is mainly determined by low-energy electrons, T_{eff} shows a tendency of a decrease with increasing driving current as listed in table 4.3.

According to the above analysis, more ionization processes occur as the driving current increases. Therefore, more positive Cl_2^+ and Cl^+ ions are created. These ions enter the sheath

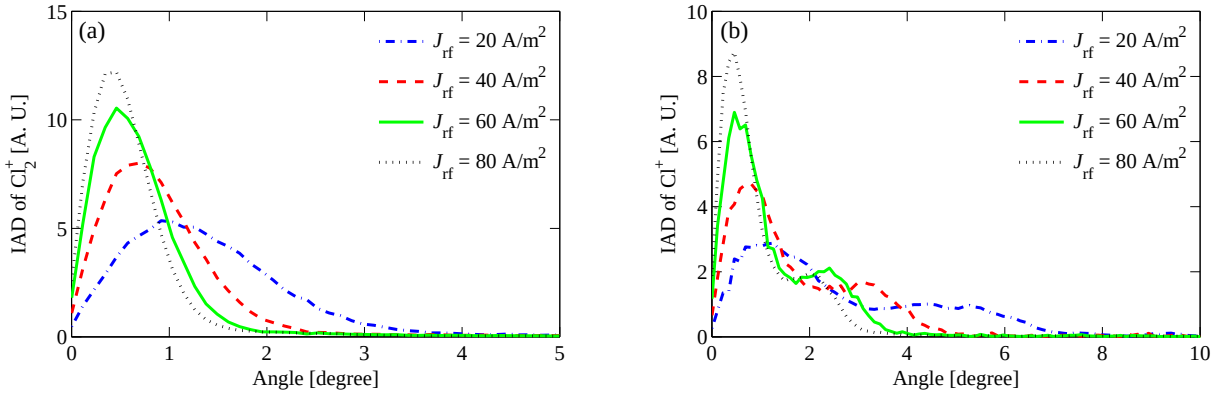

Figure 4.16: The IAD of (a) Cl_2^+ ions and (b) Cl^+ ions at the powered electrode for a parallel plate capacitively coupled chlorine discharge at 10 mTorr with a gap separation of 0.0254 m by a current source operated at 27.12 MHz.

region and are accelerated to the electrode by a strong electric field, leading to the increase of both the absorbed power deposited on positive ions and the flux of positive ions to the surface, which can be seen in figures 4.14(a) and (b). Similar variation for the absorbed power has been observed in capacitively coupled chlorine discharges through model calculations (Rogoff et al., 1986; Lee et al., 1997). Moreover, the densities of electrons, Cl radicals, Cl_2^+, Cl^+ and Cl^- ions have been found to increase almost linearly with increasing power deposited on the electrons (Lee et al., 1997), which can also be observed in figure 4.14(a) and table 4.3.

Figures 4.15(a) and (b) and figures 4.16(a) and (b) show the IED and IAD of Cl_2^+ and Cl^+ ions at the powered electrode for different driving currents, respectively. As the driving current increases, the IEDs of Cl_2^+ and Cl^+ ions both shift to the high-energy region and evolves from single-peak to bimodal profile. Meanwhile, the IADs of Cl_2^+ and Cl^+ ions become more accumulated at small angles and show more anisotropic profile. The IED in capacitive discharges has been thoroughly reviewed and analyzed by Kawamura et al. (1999). The sheath formed in our explored cases is a collisionless rf sheath. In collisionless sheath, the crucial parameter determining the shape of the IED is the relation $\tau_{\mathrm{ion}}/\tau_{\mathrm{rf}}$, where τ_{ion} is the ion transit time and $\tau_{\mathrm{rf}} = 2\pi/\omega$ is the rf period. The ion transit time is calculated by (Kawamura et al.,

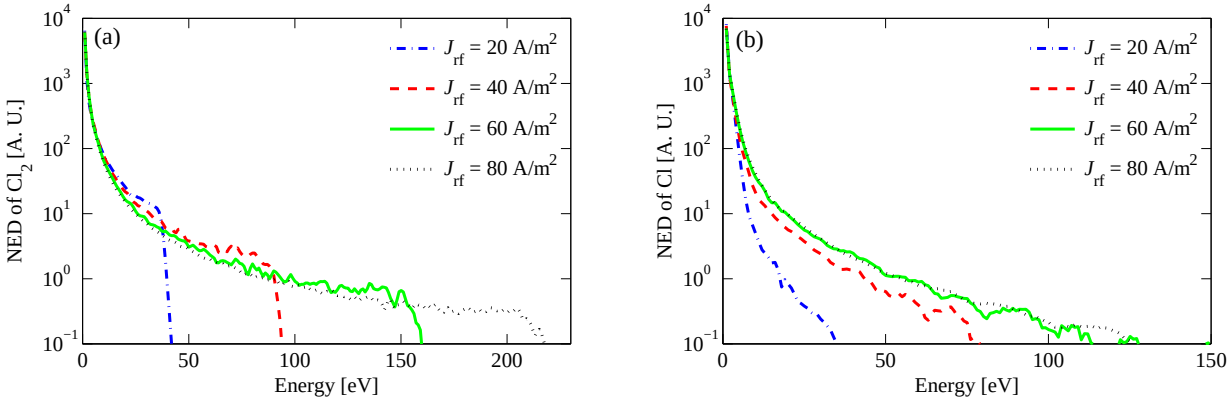

Figure 4.17: The NED of high-energy (> 1 eV) (a) Cl_2 molecules and (b) Cl atoms at the powered electrode for a parallel plate capacitively coupled chlorine discharge at 10 mTorr with a gap separation of 0.0254 m by a current source operated at 27.12 MHz.

1999)

$$\tau_{\text{ion}} = 3\overline{s}_{\text{m}}\left(\frac{M}{2e\overline{V}_{\text{s}}}\right)^{1/2} \tag{4.3}$$

where $\overline{s}_{\text{m}}$ is the average sheath thickness, $\overline{V}_{\text{s}}$ is the average sheath potential, M is the ion mass, and e is the electron charge. Cases 1 – 4 fall into the high-frequency regime ($\tau_{\text{ion}}/\tau_{\text{rf}} \gg 1$). The ions only respond to the average sheath potential drop, resulting in a narrow IED with one or two maxima points, different from the broad IED obtained in the low-frequency regime ($\tau_{\text{ion}}/\tau_{\text{rf}} \ll 1$). The width of the IED in the high-frequency regime has been analytically calculated by Benoit-Cattin and Bernard (1968) by assuming realistic Child-Langmuir space-charge sheath electric field, constant sheath width, sinusoidal sheath voltage and zero initial ion velocity at the sheath-plasma boundary. The expression for the IED width, ΔE_{i}, is given by (Benoit-Cattin and Bernard, 1968)

$$\Delta E_{\text{i}} = \frac{8e\widetilde{V}}{3\overline{s}_{\text{m}}\omega}\left(\frac{2e\overline{V}_{\text{s}}}{M}\right)^{1/2} = \frac{4e\widetilde{V}}{\pi}\left(\frac{\tau_{\text{rf}}}{\tau_{\text{ion}}}\right) \tag{4.4}$$

where $\widetilde{V}$ is the applied voltage and $\omega = 2\pi f$ is the radian frequency. Therefore, the IED is centered at $e\overline{V}_{\text{s}}$ and has two peaks split by ΔE_{i} proportional to $\widetilde{V}$. Both the average sheath

potential and the applied voltage increase with increasing driving current in cases 1 – 4, then the IEDs shift to high-energy region and become broader in figures 4.15(a) and (b). Meanwhile, the normal component of the ion velocity is increased by the sheath potential and consequently the IADs shown in figures 4.16(a) and (b) become more accumulated at small-angle region.

Figures 4.17(a) and (b) show the NED of Cl_2 molecules and Cl atoms, respectively. The NED, IED and IAD shown in our work are all flux distributions. We track the particles (ions and high-energy neutrals) which reach the surface within certain time. Then we record their energy to give an energy distribution. The NEDs of Cl_2 molecules and Cl atoms are similar to the NED of H atoms in a capacitively coupled H_2 discharge (Panarese et al., 2013). The low-energy part of the NED is well fitted by a Maxwellian distribution at the gas temperature, while the NED has a long superthermal tail. As the driving current increases, the NED extends to high-energy region. The fast neutrals reaching the surface are mainly created through elastic scattering and charge exchange between fast ions and thermal neutrals in the sheath region.

4.3.2 Effect of driving frequency

Cases 1, 5, 6 and 7 are used to explore the effect of driving frequency on the discharge and the results are shown in figures 4.18 – 4.22. As the driving frequency increases with fixed absorbed power, the variations of the electron heating rate shown in figure 4.18 and the EEPF shown in figure 4.19 are quite different from other discharges. As the driving frequency increases from 13.56 to 40.68 MHz, the stochastic heating in the sheath region becomes prominent and the Ohmic heating in the bulk plasma is diminished as shown in figure 4.18, while the EEPF changes from Druyvesteyn like to bi-Maxwellian profile as shown in figure 4.19. The proportion of the majority low-energy electrons increases with increasing driving frequency and therefore the effective electron temperature decreases. The bi-Maxwellian EEPF is mainly enhanced by the stochastic heating in the plasma sheath and the electron nonlocal kinetic property as the driving frequency is increased. Similar variation of the electron heating rate profile with increasing

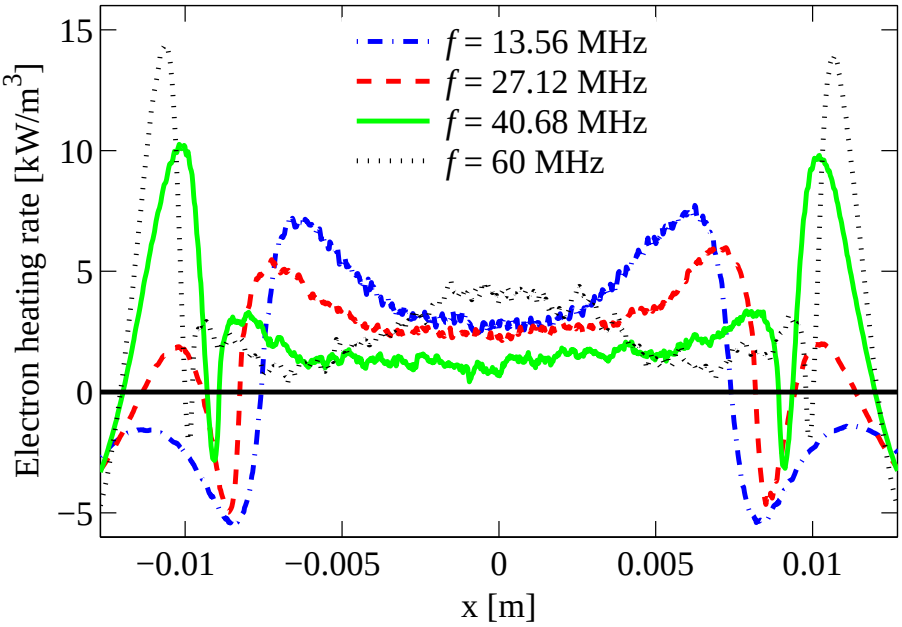

Figure 4.18: The time averaged electron heating rate profile for a parallel plate capacitively coupled chlorine discharge at 10 mTorr with a gap separation of 0.0254 m by a current source. The absorbed power is maintained at 1.20 W for each case by adjusting the applied current.

driving frequency at fixed dissipated power has been observed in a capacitively coupled H_2 discharge (Novikova et al., 2003), in which the peaks in the electron heating rate profile in the sheath region become sharper and the sheath width decreases as the driving frequency increases. Similar variation of EEPF with increasing driving frequency is observed in an electropositive Ar discharge (Abdel-Fattah and Sugai, 2003) and an electronegative SiH_4/H_2 discharge (Yan and Goedheer, 1999) and is explained by a transition in electron heating mode from Ohmic heating in the bulk region at low frequency to stochastic heating in the sheath region at high frequency. As the driving frequency is increased, the average sheath potential decreases. Consequently, positive ions are pulled out less efficiently and the density of ions in the bulk region increases as shown in table 4.3. Due to charge quasineutrality, the density of electrons also increases. In the bulk region, the current density ($J_{\text{bulk}} \approx e\mu_e E_{\text{bulk}}$, where μ_e is the mobility coefficient and E_{bulk} is the electric field in the bulk) is constant due to constant absorbed power. Therefore,

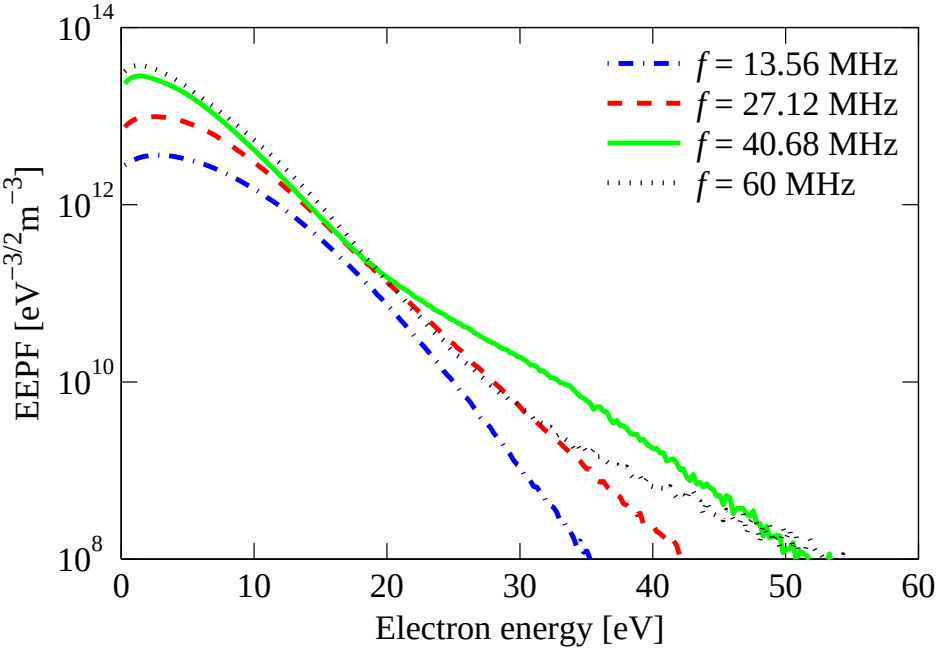

Figure 4.19: The EEPF in the center of a parallel plate capacitively coupled chlorine discharge at 10 mTorr with a gap separation of 0.0254 m by a current source. The absorbed power is maintained at 1.20 W for each case by adjusting the applied current.

a higher electron density means a weaker electric field in the bulk region, which is responsible for heating electrons. Thus, a weaker bulk electric field means decrease in electron heating in the bulk, which leads to the decrease of the effective electron temperature in the discharge center (Yan and Goedheer, 1999). As the driving frequency further increases from 40.68 to 60 MHz, the Ohmic heating in the bulk region shown in figure 4.18 increases dramatically, which indicates more collisions between electrons and neutrals. Meanwhile, the proportion of low-energy electrons is increased as shown in figure 4.19 and the effective electron temperature decreases.

As the driving frequency increases, the density of Cl_2^+ ions in the bulk region increases, which is consistent with the variation of the density of Cl_2^+ ions with increasing frequency from 1 to 13 MHz at fixed power in a chlorine discharge observed experimentally (Donnelly et al., 1982). Meanwhile, the electron density is found to increase with increasing frequency at fixed power,

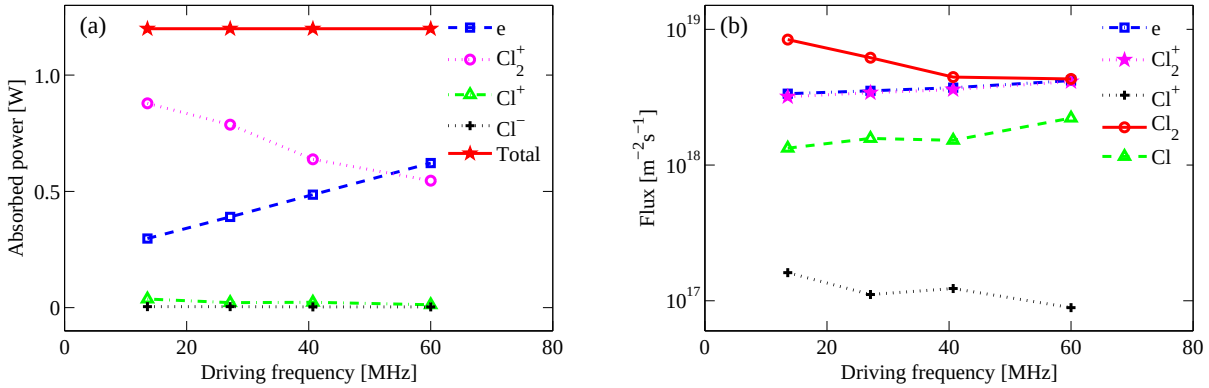

Figure 4.20: The (a) absorbed power by electrons, Cl_2^+, Cl^+ and Cl^- ions in the whole discharge volume and (b) flux of electrons, Cl_2^+ and Cl^+ ions, and high-energy (> 1 eV) Cl_2 molecules and Cl atoms reaching the powered electrode for a parallel plate capacitively coupled chlorine discharge at 10 mTorr with a gap separation of 0.0254 m by a current source. The absorbed power is maintained at 1.20 W for each case by adjusting the applied current.

which is similar to what is seen in simulation of capacitively coupled H_2 (Novikova et al., 2003) and experimentally in Ar (Zhu et al., 2007) discharges. Since the electron density increases more sharply with increasing frequency than the density of Cl^- ions, the electronegativity decreases. In a capacitively coupled CF_4 discharge (Segawa et al., 1999), the electronegativity is found to decrease slightly with increasing driving frequency but it is more strongly dependent on the discharge pressure rather than the driving frequency. However, in capacitively coupled chlorine discharge, both the discharge pressure as shown in table 4.2 and the driving frequency as shown in table 4.3 are found to strongly affect the electronegativity. Figure 4.20(a) shows that the power absorbed by electrons increases linearly while the power absorbed by ions decreases linearly by the same amount with increasing frequency, which is because the average sheath potential decreases with increasing driving frequency and ions are accelerated by a lower sheath potential. Figure 4.20(b) shows that the fluxes of Cl_2^+ and Cl^+ ions remain almost invariant with increasing driving frequency for fixed power, which is similar to the variation of the flux of SiH_3^+ ions in a capacitively coupled SiH_4/H_2 discharge (Yan and Goedheer, 1999).

Table 4.3 shows that as the driving frequency increases at fixed absorbed power, the average

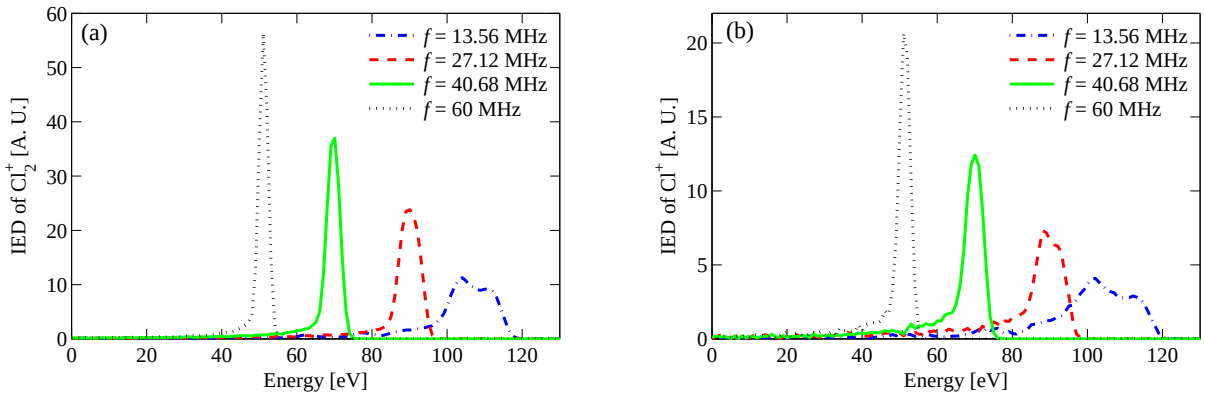

Figure 4.21: The IED of (a) Cl_2^+ ions and (b) Cl^+ ions at the powered electrode for a parallel plate capacitively coupled chlorine discharge at 10 mTorr with a gap separation of 0.0254 m by a current source. The absorbed power is maintained at 1.20 W for each case by adjusting the applied current.

sheath potential decreases, which leads to the results that the IEDs of Cl_2^+ and Cl^+ ions shown in figures 4.21(a) and (b) become narrower and shift towards lower energy and the IADs of Cl_2^+ and Cl^+ ions shown in figures 4.22(a) and (b) extend towards larger angle. The decrease of average sheath potential and similar shift of IED with increasing frequency is also observed in other discharges that concern frequency variation under constant power conditions (Schwarzenbach et al., 1996; Yan and Goedheer, 1999; Segawa et al., 1999; Amanatides and Mataras, 2001; Novikova et al., 2003; Zhu et al., 2007). This variation is attributed to an increase of the displacement current with increasing frequency, and hence a lower rf voltage is needed at high frequency to maintain the same power density. According to an exploration of an Ar/O_2 discharge (Zhang et al., 2013), as the driving frequency increases from 2 to 60 MHz, τ_{rf}/τ_{ion} decreases, and the applied voltage also decreases. The Ar^+ ions experience more rf cycles before reaching the wafer surface. Therefore, according to equation (4.4), the width of the IED progressively decreases and the two peaks of the IED eventually merge as the frequency increases as shown in figures 4.21(a) and (b).

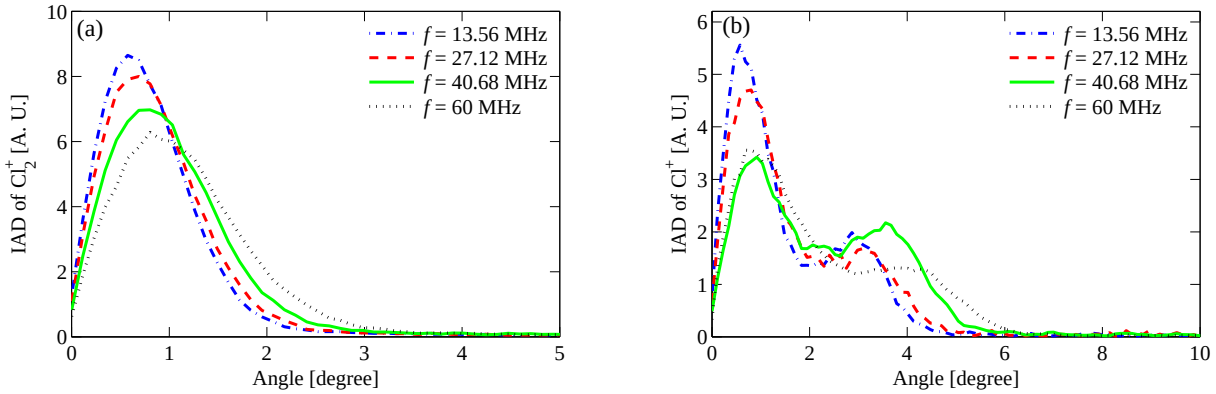

Figure 4.22: The IAD of (a) Cl_2^+ ions and (b) Cl^+ ions at the powered electrode for a parallel plate capacitively coupled chlorine discharge at 10 mTorr with a gap separation of 0.0254 m by a current source. The absorbed power is maintained at 1.20 W for each case by adjusting the applied current.

4.3.3 Effect of secondary electrons

Under the discharge conditions in our study, the sheath is almost collisionless and more ions undergo full length of the sheath and acquire an energy comparable to the average sheath potential, so secondary electron emission will have certain influence on the discharge and will be considered in subsequent study. In order to test the effect of secondary electron emission due to the bombardment of Cl_2^+ and Cl^+ ions on the discharge, we run cases 8, 9 and 10 at 10 mTorr with all the initial parameter the same as in case 1 except changing the secondary electron emission coefficient, γ_{se}, to 0.1, 0.2 and 0.4, which are similar to the values of γ_{se} that have been explored for an oxygen discharge (Roberto et al., 2006) and within the range of typical secondary electron emission coefficient compiled by Phelps and Petrović (1999). The secondary electron emission yield is typically in the range $0.01 \leq \gamma_{se} \leq 0.3$ for clean metal surfaces and slightly higher for dirty metal surfaces (Böhm and Perrin, 1993; Phelps and Petrović, 1999). For oxides it can be in the range 0.1 – 0.5 or even higher according to a renowned database compiled by Joy (1995). Although the secondary electron emission coefficient can be even higher (> 1) for electrodes made of oxide such as MgO (Ohtsu and Fujita, 2004), the range of γ_{se} explored in our study will not cover that high value. The results for cases 1, 8, 9 and 10 are shown in

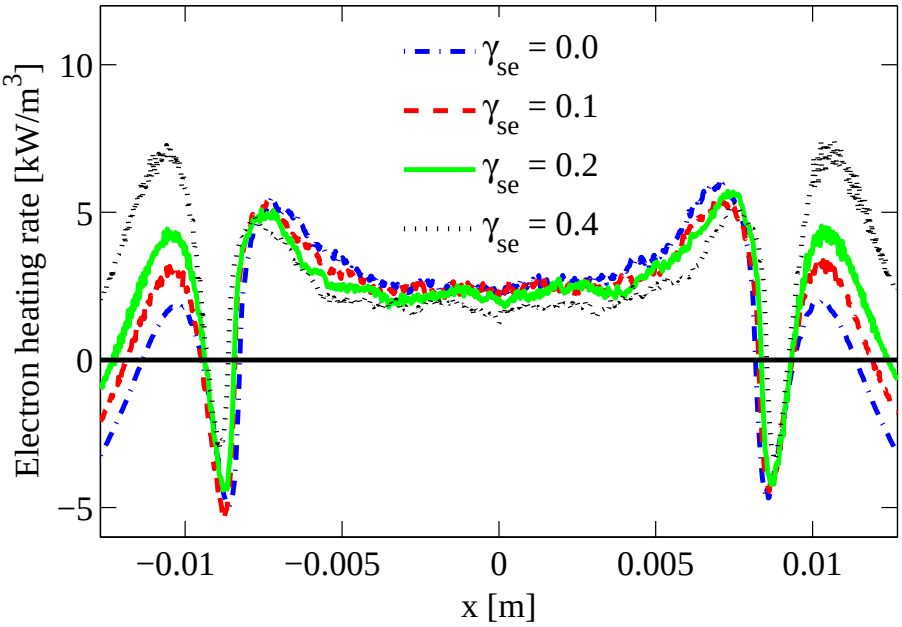

Figure 4.23: The time averaged electron heating rate profile for a parallel plate capacitively coupled chlorine discharge at 10 mTorr with a gap separation of 0.0254 m by a 40 A/m^2 current source operated at 27.12 MHz.

figures 4.23 – 4.25.

As γ_{se} increases, the average sheath potential as listed in table 4.3 decreases slightly since a lower voltage drop is needed there to ensure equal fluxes of electrons and ions, which is also used to explain the asymmetry of the sheath potential induced by the secondary electrons by Lafleur et al. (2013). Accordingly, the IEDs of Cl_2^+ and Cl^+ ions shift to the low-energy region by the same amount of the decrease of $\overline{V}_s$. The electron heating rate shown in figure 4.23 has similar variation with the electron heating rate in a capacitive oxygen discharge operated at 20 mTorr (Roberto et al., 2006). The electron heating rate in the sheath region increases while in the bulk region decreases slightly. Figure 4.24 shows the evolution of EEPF with the increase of γ_{se}. The enhancement of high-energy electrons in the tail of EEPF is due to more electrons emitted at the electrode and then accelerated to the bulk region by the electric field in the sheath as γ_{se} increases.

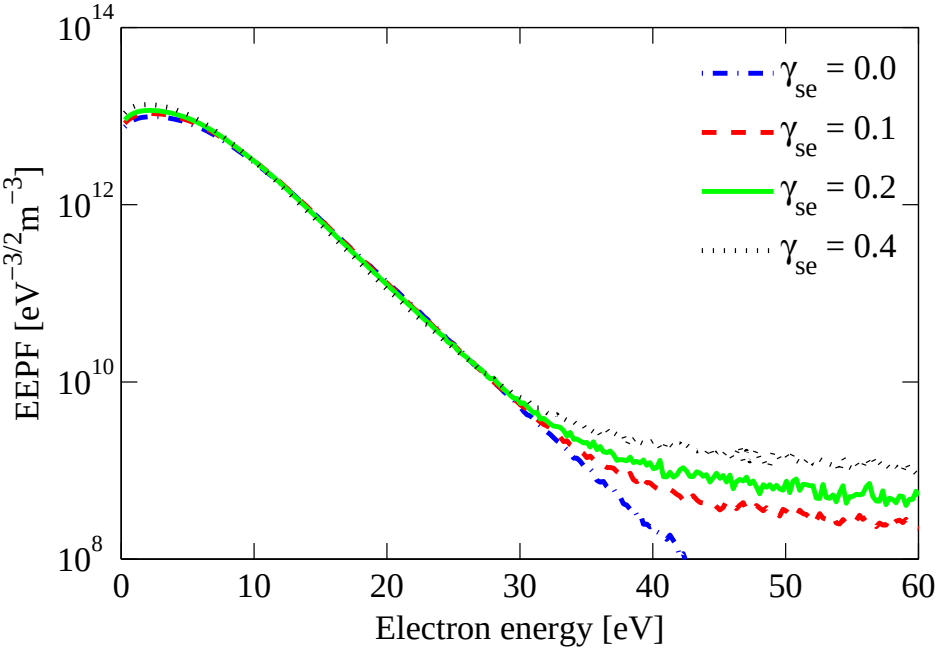

Figure 4.24: The EEPF in the center of a parallel plate capacitively coupled chlorine discharge at 10 mTorr with a gap separation of 0.0254 m by a 40 A/m^2 current source operated at 27.12 MHz.

We note that the power absorbed by electrons increases with increased secondary electron emission coefficient as seen in figure 4.25(a). The decrease of the power absorbed by Cl_2^+ is mainly due to the decrease of the average sheath potential. The ion flux shown in figure 4.25(b) increases slightly with increasing γ_{se}, which is mainly because of enhanced ionization in the sheath. As γ_{se} increases, there are more secondary electrons emitted from the surface. These secondary electrons get accelerated by the sheath voltage and obtain very high energy. As a result, they efficiently lead to ionization processes especially when the gas pressure is high enough. New ions formed in the sheath then travel towards the wall and contribute to the increased fluxes of Cl_2^+ and Cl^+ ions at the surface.

The effective electron temperature in the discharge center listed in table 4.3 decreases with increasing γ_{se}. As γ_{se} increases, more ionization processes occur because of more secondary electrons with high energy, and the system starts to enter a γ-heating mode in which the electron

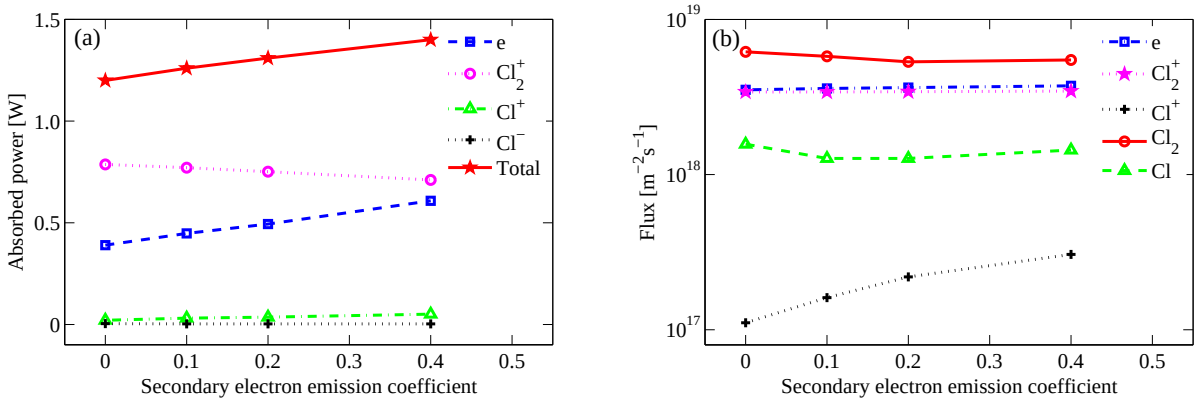

Figure 4.25: The (a) absorbed power by electrons, Cl_2^+, Cl^+ and Cl^- ions in the whole discharge volume and (b) flux of electrons, Cl_2^+ and Cl^+ ions, and high-energy (> 1 eV) Cl_2 molecules and Cl atoms reaching the powered electrode for a parallel plate capacitively coupled chlorine discharge at 10 mTorr with a gap separation of 0.0254 m by a 40 A/m^2 current source operated at 27.12 MHz.

heating is mainly due to acceleration of electrons by electric field in the sheath as shown in figure 4.23. Since more ionization processes occur, the effective electron temperature in the bulk decreases to still satisfy the particle balance. As there are much more bulk electrons than high-energy secondary electrons, the average electron energy and hence the effective electron temperature decreases, even if the ionization rate actually increases.

The effect of secondary electrons on other parameters such as the IAD and NED are negligible. Similarly, in capacitively coupled helium (Surendra et al., 1990) and chlorine (Kawano et al., 2000) discharges, the electron and ion densities are found to increases slightly with increasing γ_{se} and the major features of the discharges are essentially unchanged.

Chapter 5

Dual-frequency capacitively coupled chlorine discharge

We add another source with a low driving frequency to the SF CCP discharge explored in case 1 in section 4.3 and the discharge evolves to a typical DF CCP discharge as shown in figure 2.8. The discharge is driven by a dual-frequency current source

$$J(t) = J_{\mathrm{hf}}\sin(2\pi f_{\mathrm{hf}}t) + J_{\mathrm{lf}}\sin(2\pi f_{\mathrm{lf}}t)$$

where f_{hf}, f_{lf}, J_{hf}, J_{lf} are the frequency and current density of the high- and low-frequency sources, respectively. The plasma density is found to scale with the square of the high frequency ($n \propto f_{\mathrm{hl}}^2$) and the average energy of ions reaching the substrate is found to scale with the low-frequency voltage ($\mathcal{E}_{\mathrm{i}} \propto V_{\mathrm{lf}}$) (Lieberman and Lichtenberg, 2005). According to this, we can set $f_{\mathrm{hf}} \gg f_{\mathrm{lf}}$ and $J_{\mathrm{lf}} \ll J_{\mathrm{hf}}$ to try to decouple the two sources and test the separate control of ion flux and energy. Here we set $f_{\mathrm{hf}} = 27.12$ MHz and $f_{\mathrm{lf}} = 2$ MHz, respectively. The high-frequency current density, J_{hf}, is maintained at 40 A/m^2. The low-frequency current density, J_{lf}, is varied from 0 to 4 A/m^2 in cases 1, 11, 12 and 13 respectively to investigate how the discharge evolves from single-frequency discharge to dual-frequency discharge. The phase difference between the

two currents is set to be 0 at the beginning of the simulation. Other parameters are the same as in case 1 as listed in table 4.3. The simulation is run for 5500 high-frequency cycles. The density profile and the electron heating rate profile are averaged over 54 high-frequency cycles, i.e., nearly 4 low-frequency cycles, after the simulation runs to a stable state. The simulation results are listed in table 5.1 and shown in figures 5.1 – 5.5.

Ideally, the ion flux to the electrode should remain constant after adding a low-frequency source and the ion bombarding energy should increase linearly with increasing low-frequency current. In practice, the independent control of ion energy and flux is found to be difficult. The independence is found to be only possible within a small range of parameter space (Boyle et al., 2004). Also, both the low-frequency and high-frequency sources will influence the ion energy and angular distributions (Zhang et al., 2013). The reason for the difficulty in the separate control is ascribed to the coupling between the two sources (Gans et al., 2006; Ahn and Chang, 2009) and the nonlinear dynamics of plasmas powered by multi-frequency sources (Rauf and Kushner, 1999).

The analysis of the effect of low-frequency current on dual-frequency capacitively coupled chlorine discharge is given in section 5.1 and is taken from a published paper (Huang and Gudmundsson, 2014a). The analysis of the effect of adding a low-frequency source with a non-zero secondary electron emission coefficient on the discharge is given in section 5.2 and has been written as a paper (Huang and Gudmundsson, 2014b). The analysis of the spatial ion energy and angular distributions in dual-frequency capacitively coupled chlorine discharge given in section 5.3 has also been written as a paper (Huang and Gudmundsson, 2014c).

5.1 Effect of low-frequency current

Table 5.1 shows that with increasing low-frequency current from 0 to 4 A/m^2, the electron density first increases slightly and then decreases, while the density of Cl^- ions decreases slightly

Table 5.1: The simulation results for cases 1, 11, 12 and 13 in order to explore the effect of adding a low-frequency source on the discharge. (n_e, n_{Cl^+}, n_{Cl^-} and α_0 denote the density of electrons, Cl^+ and Cl^- ions and the electronegativity in the center of the discharge, respectively.)

Case	J_{hf} [A/m^2]	J_{lf} [A/m^2]	P_{abs} [W]	n_{Cl}/n_g [%]	$\bar{s}_m$ [m]	T_{eff} [eV]	$\overline{V}_s$ [V]	V_{hf} [V]	V_{lf} [V]	n_e [10^{14}m^{-3}]	n_{Cl^+} [10^{14}m^{-3}]	n_{Cl^-} [10^{16}m^{-3}]	α_0
1	40	0	1.20	9.38	0.0046	3.60	92.1	181	0	7.20	2.05	6.01	83.5
11	40	1	1.31	10.5	0.0049	3.53	102	206	37	7.41	2.33	5.80	78.3
12	40	2	1.88	14.1	0.0067	3.47	151	270	123	7.89	4.02	6.02	76.3
13	40	4	3.76	22.4	0.0080	4.09	251	325	391	5.64	9.28	6.65	118

and then increases. Consequently, the electronegativity first decreases and then increases. The variation of the density of Cl^- ions is consistent with the variation of plasma density in a dual-frequency (60/2 MHz) CF_4 discharge reported by Wang et al. (2012). They explained this variation by the influence of increasing low-frequency voltage on the effective frequency (Kim and Lee, 2005b). The density of Cl^+ ions increases steadily with increasing low-frequency current, which is mainly due to the increased dissociation fraction of background gas caused by increased absorbed power.

Figure 5.1 shows the time averaged electron heating rate profile for a chlorine discharge as the low-frequency current is added and the current density is increased. As the low-frequency current increases from 0 to 2 A/m^2, the role of electron heating in the bulk region decreases and the EEPF in figure 5.2 shows that the number of low-energy electrons (< 5 eV), as well as the number of high-energy (> 15 eV) electrons, increases steadily. The increase of low-energy electrons with increasing low-frequency current is also observed in Ar discharges by Kim and Lee (2004, 2005a). The increase of low-energy electrons can be explained by the reduction in the collisional heating of the low-energy bulk electrons as shown in figure 5.1. Since more electrons are trapped in the dc ambipolar potential barrier and can only gain their energy from the bulk electric field through collisional heating process, the effective electron temperature of the low-energy electrons decreases.

As the low-frequency current further increases from 2 to 4 A/m^2, there is a significant depletion of low-energy electrons and enhancement of high-energy electrons in the EEPF shown in figure 5.2. Similar variation of the EEPF in a dual-frequency CF_4 discharge has been reported

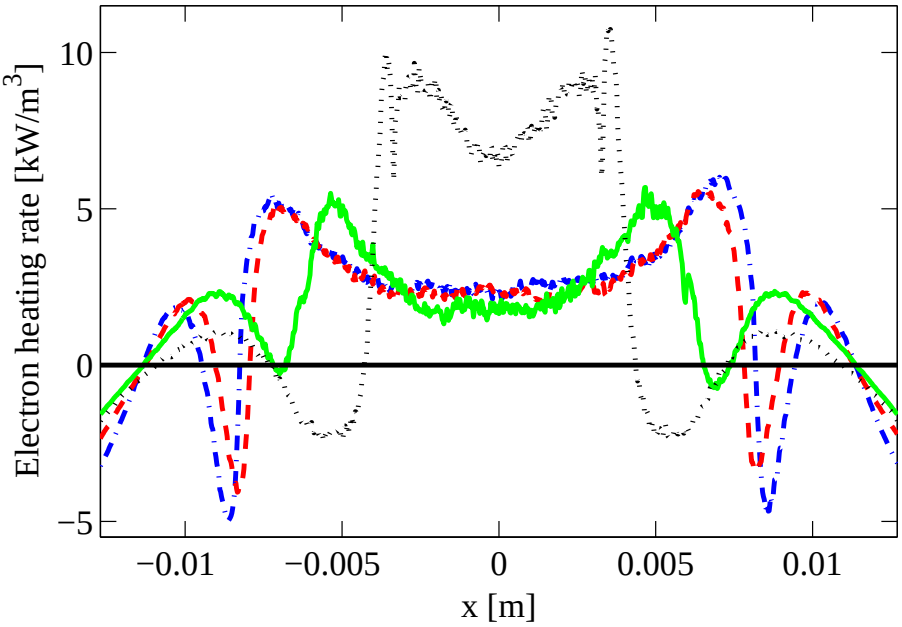

Figure 5.1: The time averaged electron heating rate profile for a dual-frequency parallel plate capacitively coupled chlorine discharge at 10 mTorr with a gap separation of 0.0254 m. (The legend in this figure is the same as in figure 5.2.)

(Donkó and Petrović, 2006). The enhanced high-energy tail in the EEPF is also observed in figure 4.13. However, we should notice that the mechanism for the enhancement of the high-energy tail of EEPFs in figures 4.13 and 5.2 are different. In figure 4.13, the enhanced high-energy tail of the EEPF is due to the enhanced stochastic heating in the sheath region shown in figure 4.12. In figure 5.2, the enhanced high-energy tail of the EEPF is due to the enhanced electric field in the bulk region, which is a characteristic feature of electronegative discharge according to Georgieva et al. (2003). The transition of EEPF from Druyvesteyn like to bi-Maxwellian profile with increasing low-frequency current in dual-frequency Ar discharges (Kim and Lee, 2004, 2005a) is not observed in our study. In addition, the phenomenon that the heating effect is dramatically enhanced with the addition of a low-frequency source (Turner and Chabert, 2006, 2007a,b; Sharma and Turner, 2013) is not observed in our study.

Figures 5.3(a) and (b) show the absorbed power and the flux with the addition of a low-

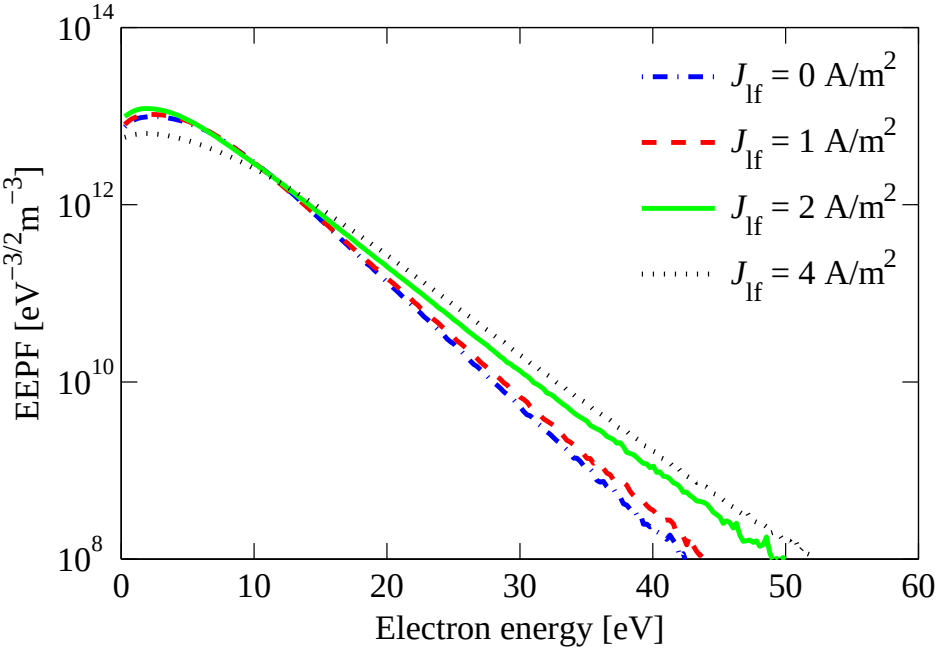

Figure 5.2: The EEPF in the center of a dual-frequency parallel plate capacitively coupled chlorine discharge at 10 mTorr with a gap separation of 0.0254 m.

frequency source, respectively. The average sheath potential increases with increasing low-frequency current, and consequently the power absorbed by positive ions in the sheath increases, which mainly results in increased total power. However, the power absorbed by electrons remains nearly constant. The flux of Cl_2^+ ions to the surface increases monotonically with increasing low-frequency current, which is similar to the variation of the ion flux with increasing low-frequency power in a dual-frequency Ar/O_2 discharge (Booth et al., 2010). The average sheath potential, as well as the median of the IEDs for Cl_2^+ and Cl^+ ions shown in figures 5.4(a) and (b), increases almost linearly with increasing low-frequency current. This is similar to the variation of the flux and energy of CF_3^+ ions observed in a dual-frequency CF_4 discharge (Donkó and Petrović, 2006) and Ar^+ ions in a dual-frequency Ar discharge (Wakayama and Nanbu, 2003) with increasing low-frequency voltage. The density of Cl^- ions in the discharge center listed in table 5.1 depends slightly on the low-frequency current, which shows that it

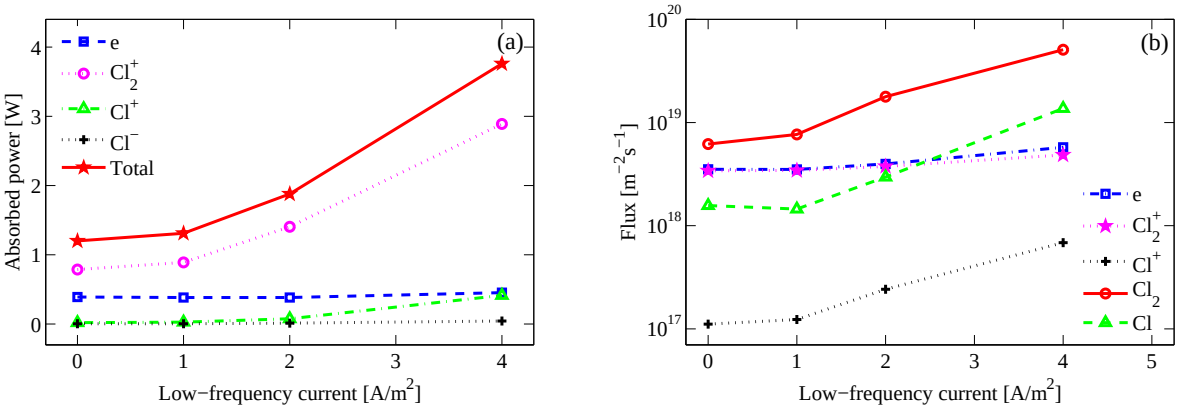

Figure 5.3: The (a) absorbed power by electrons, Cl_2^+, Cl^+ and Cl^- ions in the whole discharge volume and (b) flux of electrons, Cl_2^+ and Cl^+ ions, and high-energy (> 1 eV) Cl_2 molecules and Cl atoms reaching the powered electrode for a dual-frequency parallel plate capacitively coupled chlorine discharge at 10 mTorr with a gap separation of 0.0254 m.

is the frequency and amplitude of the high-frequency current that govern the plasma density. Figure 5.3(b) shows that as the low-frequency current increases from 0 to 4 A/m^2, the fluxes of high-energy (> 1 eV) Cl atoms and Cl_2 molecules increase, which is due to increased densities of high-energy Cl atoms and Cl_2 molecules in both the bulk and sheath region. This kind of increase is also observed in figure 4.14(b) in the single-frequency discharge when the driving current is increased from 20 to 80 A/m^2.

Table 5.1 shows that as the low-frequency current increases, the low-frequency voltage component, V_{lf}, increases more significantly than the high-frequency voltage component, V_{hf}, which indicates that an addition of low-frequency current into a high-frequency capacitive discharge predominantly enhances the discharge voltage. This is because of the capacitive characteristic of the plasma discharge at low pressure. In capacitive discharge, the low-frequency current encounters higher impedance than the high-frequency current. Thus, the ion bombardment energy to the electrode can be controlled using low-frequency current source without a significant change in the total discharge current. Spatial ion energy and angular distributions of Cl_2^+ and Cl^+ ions along the axis of the discharge in case 12 are especially analyzed in section 5.3. Here we mainly concentrate on the variation of IED and IAD at the

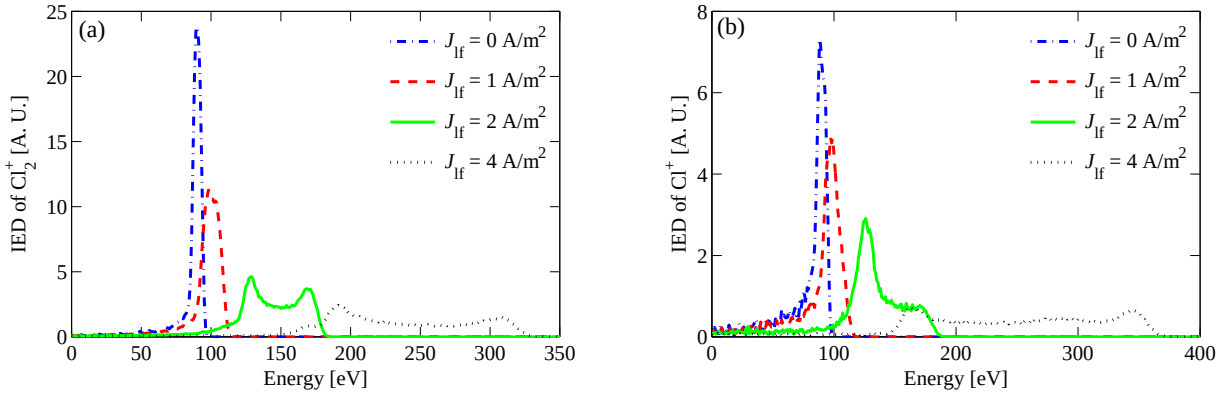

Figure 5.4: The IED of (a) Cl_2^+ ions and (b) Cl^+ ions at the powered electrode for a dual-frequency parallel plate capacitively coupled chlorine discharge at 10 mTorr with a gap separation of 0.0254 m.

electrode surface with varying low-frequency current. Figures 5.4(a) and (b) and figures 5.5(a) and (b) show the IED and IAD of Cl_2^+ and Cl^+ ions with the addition of a low-frequency source, respectively. The IED becomes wider and extends to the high-energy region with increasing low-frequency current. Meanwhile, the IAD is more concentrated in the small-angle region with increasing low-frequency current. The variation of the IED is similar to the variation of IED for Ar^+ ions as has been demonstrated in a dual-frequency Ar discharge (Kim and Lee, 2005b). The variation of the IAD is similar to the variation of IADs for CF_3^+ and F^+ ions in a dual-frequency CF_4 discharge (Wang et al., 2012) and CF_3^+ and Ar^+ ions in a dual-frequency Ar/CF_4 discharge (Bi et al., 2009). Without low-frequency source, ions cannot respond to the instantaneous change of the electric field at such a high frequency, i.e., 27.12 MHz. Ions are accelerated to the electrode by the average sheath potential. These ions almost undergo no collisions in the sheath region and bombard the electrode with energy equal to the average sheath potential. Therefore, the IED in the single-frequency regime is narrow with one outstanding peak. After adding a 2 MHz low-frequency source, ions can follow the instantaneous change of the electric field generated by the two sources. Therefore, the energy of ions incident on the electrode is affected by the phase and the amplitude of the low-frequency current. After adding the low-frequency source, the average sheath potential increases, and the maximum value of the incident

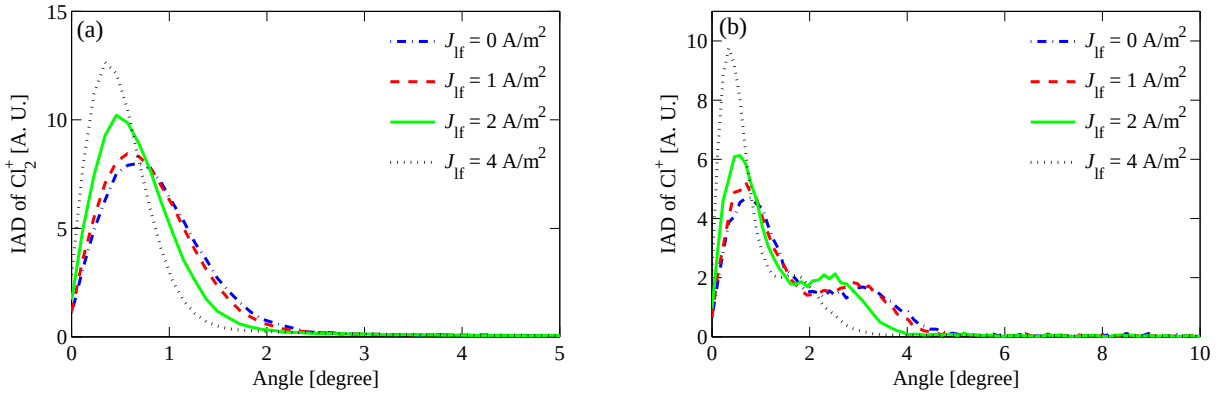

Figure 5.5: The IAD of (a) Cl_2^+ ions and (b) Cl^+ ions at the powered electrode for a dual-frequency parallel plate capacitively coupled chlorine discharge at 10 mTorr with a gap separation of 0.0254 m.

ion energy becomes higher. The IED extends to the high-energy region as low-frequency current is increased. Furthermore, the ions will be accelerated directly by a stronger electric field. The IED becomes wider and moves towards the higher-energy region. Meanwhile, figures 5.5(a) and (b) show that the incident angle gets narrower. This is because the ions are driven by a higher vertical electric field and the directional speed leads to a smaller angular distribution.

Figures 4.16(b), 4.22(b) and 5.5(b) show that the IAD of Cl^+ ions at the electrode surface has a secondary peak at about 2° – 5°, which is found to be caused by electron impact dissociative ionization, $e + Cl_2 \longrightarrow Cl + Cl^+ + 2e$. The energy difference between the threshold of this reaction (15.7 eV) and the potential energy of the heavy products $Cl + Cl^+$ (15 eV) should be split between Cl and Cl^+, thus energetic Cl^+ ion are created. The velocities of the high-energy Cl^+ ions are calculated using the collision model given by Nguyen (2006), Lim (2007) and Gudmundsson et al. (2013) according to the incident angle of the impact electron, so the velocity of the Cl^+ ions will have component parallel to the electrode and consequently lead to a secondary peak in the IAD at the surface.

Georgieva et al. (2003) found that in a dual-frequency $Ar/CF_4/N_2$ discharge, in the presence of a low-frequency source and a strong electric field, the light F^- ions are no longer confined in the bulk plasma as in high-frequency discharges. They partially respond to the instantaneous

Table 5.2: The simulation results for cases 12, 14 and 15 in order to explore the effect of adding a low-frequency source with a non-zero secondary electron emission coefficient on the discharge. (n_e, n_{Cl^+}, n_{Cl^-} and α_0 denote the density of electrons, Cl^+ and Cl^- ions and the electronegativity in the center of the discharge, respectively.)

Case	γ_{se}	P_{abs} [W]	n_{Cl}/n_g [%]	$\overline{s}_m$ [m]	T_{eff} [eV]	$\overline{V}_s$ [V]	V_{hf} [V]	V_{lf} [V]	n_e [$10^{14}m^{-3}$]	n_{Cl^+} [$10^{14}m^{-3}$]	n_{Cl^-} [$10^{16}m^{-3}$]	α_0
12	0.0	1.88	14.1	0.0067	3.47	151	270	123	7.89	4.02	6.02	76.3
14	0.2	1.95	14.5	0.0061	3.25	133	236	90	9.33	5.93	6.26	67.1
15	0.4	2.02	14.9	0.0056	2.98	119	218	86	11.0	7.98	6.63	60.3

electric field and can reach the surface. However, the much heavier CF_3^- ions cannot respond to the low-frequency source and they remain in the bulk plasma, where the only loss mechanism is the positive-negative ion recombination. In our simulation, the Cl^- ions can scarcely reach the surface and behave in the same way as CF_3^- ions in the $Ar/CF_4/N_2$ discharge.

5.2 Effect of secondary electrons

The effect of adding a low-frequency source with a non-zero secondary electron emission coefficient has been investigated by Kim and Lee (2005a) and Booth et al. (2010). The secondary electrons are found to influence the transition of the profile for the EEDF when the low-frequency current increases (Kim and Lee, 2005a) and lead to enhanced plasma heating through excitation and ionization (Booth et al., 2010). Here, we have run 2 extra cases (cases 14 and 15) with $J_{hf} = 40$ A/m^2 and $J_{lf} = 2$ A/m^2 and use case 12 already explore in section 5.1 as the blank contrast to explore the effect of adding a low-frequency source with a non-zero secondary electron emission coefficient on the discharge. The secondary electron emission coefficient is set to 0.2 and 0.4 for cases 14 and 15, respectively. Other control parameters are the same as in case 12. The simulation results are listed in table 5.2 and shown in figures 5.6 – 5.8.

According to the simulation results of cases 12, 14 and 15 and the results in section 4.3.3, the effect of secondary electrons on the discharge, whether with or without a low-frequency source, is analogous. The variation tendency of plasma parameters with increasing γ_{se} in the DF discharge shown in table 5.2 and figures 5.6 – 5.8 are similar to the variation tendency of

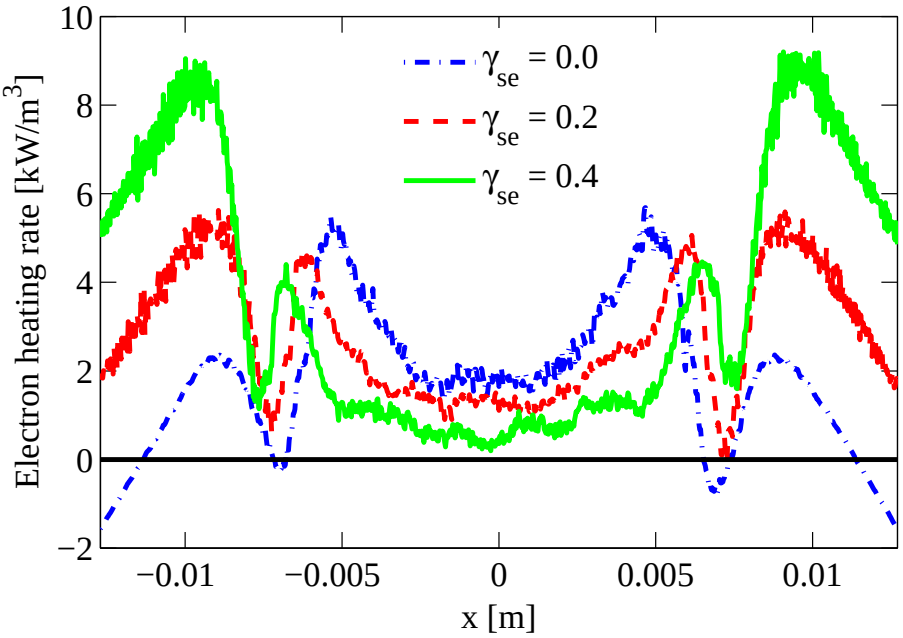

Figure 5.6: The time averaged electron heating rate profile for a dual-frequency parallel plate capacitively coupled chlorine discharge at 10 mTorr with a gap separation of 0.0254 m.

plasma parameters with increasing γ_{se} in the SF discharge shown in table 4.3 (cases 1, 8, 9 and 10) and figures 4.23 – 4.25 in section 4.3.3. However, the effect of the secondary electrons seems to be stronger in the DF discharge than in the SF discharge, which can be witnessed from the obvious transition in the heating rate profile shown in figure 5.6 and in the EEPF shown in figure 5.7. The addition of secondary electron emission amplifies the role of sheath heating due to secondary electrons accelerating through the large sheath fields (Surendra et al., 1990). The decrease of average sheath potential with increasing γ_{se} is also more obvious in the DF discharge than in the SF discharge. The intensified effect of secondary electrons in the DF discharge is possibly due to the added low-frequency source. The ions begin to respond to the instantaneous filed in the sheath and the average sheath potential increases, which shifts the IED to the high-energy region and contributes to the enhanced effect of the secondary electrons.

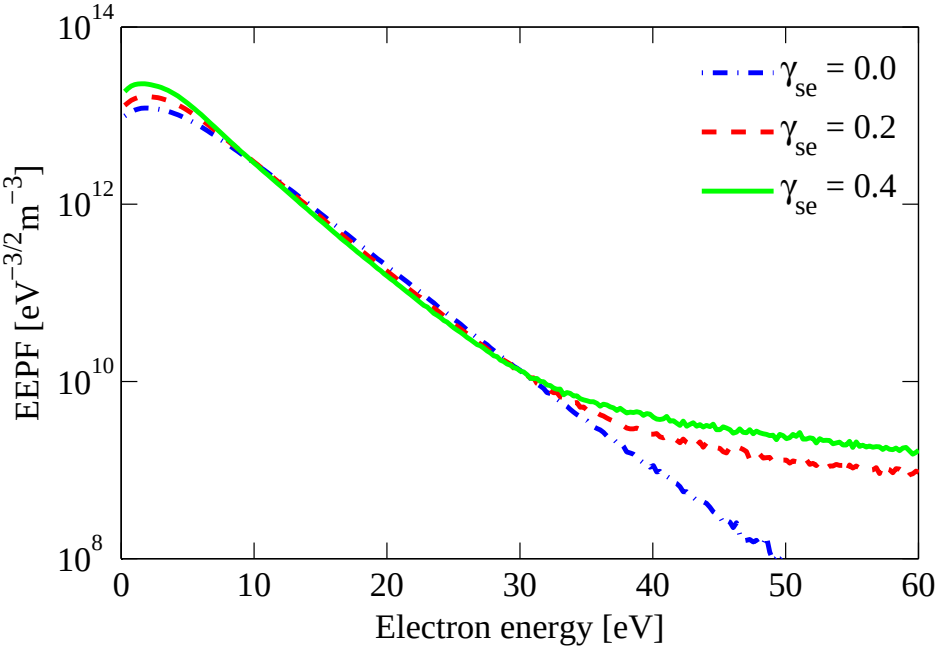

Figure 5.7: The EEPF in the center of a dual-frequency parallel plate capacitively coupled chlorine discharge at 10 mTorr with a gap separation of 0.0254 m.

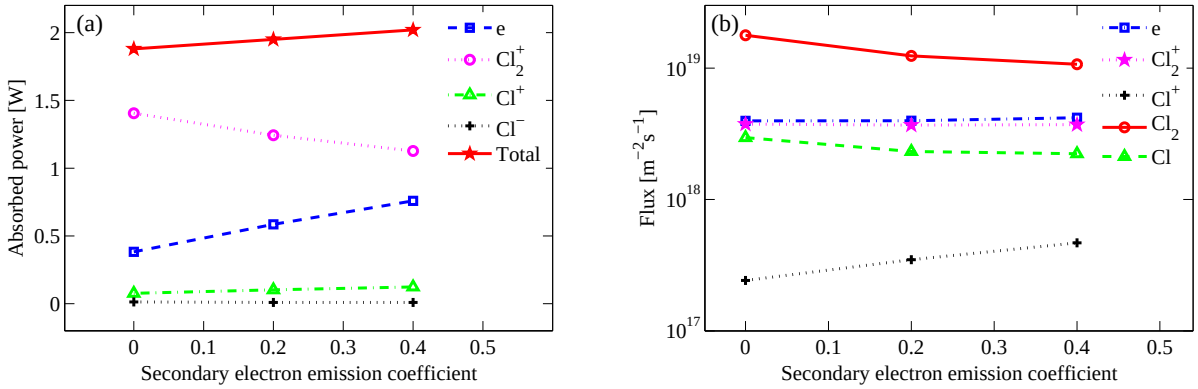

Figure 5.8: The (a) absorbed power by electrons, Cl_2^+, Cl^+ and Cl^- ions in the whole discharge volume and (b) flux of electrons, Cl_2^+ and Cl^+ ions, and high-energy ($>$ 1 eV) Cl_2 molecules and Cl atoms reaching the powered electrode for a dual-frequency parallel plate capacitively coupled chlorine discharge at 10 mTorr with a gap separation of 0.0254 m.

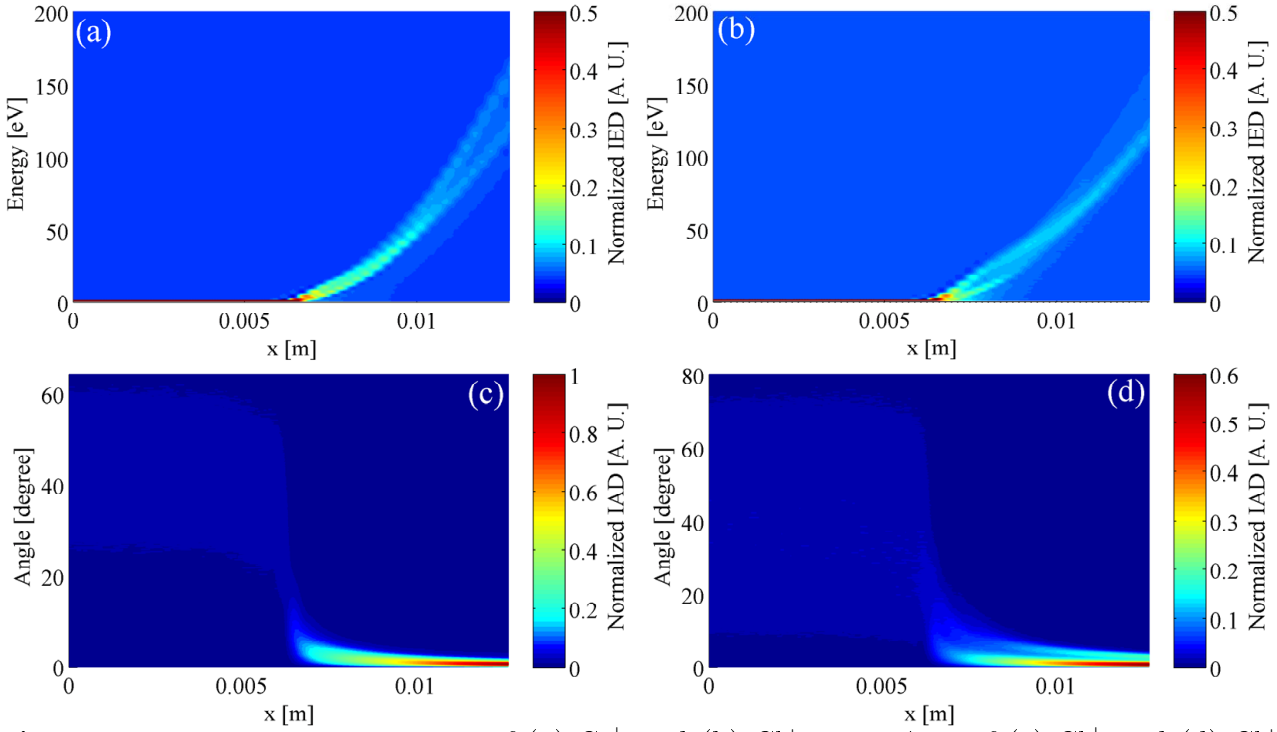

Figure 5.9: The normalized IEDs of (a) Cl_2^+ and (b) Cl^+ ions, IADs of (c) Cl_2^+ and (d) Cl^+ ions at the grounded electrode in a dual-frequency parallel-plate capacitively coupled chlorine discharge at 10 mTorr with a gap separation of 0.0254 m.

5.3 Spatial ion energy and angular distributions

In this section, we mainly focus on the spatial IEDs and IADs of Cl_2^+ and Cl^+ ions in a DF capacitively coupled chlorine discharge. We specifically explore the IEDs and IADs along the axis of the discharge explored in case 12 in section 5.1.

Figures 5.9(a) – (d) show the IEDs and IADs of Cl_2^+ and Cl^+ ions along the axis of the discharge, respectively. We only show the right hand side of the discharge due to its symmetric property. The data has been interpolated with three additional points for each data point, for visualization reasons. Figures 5.9(a) and (b) show that when the ions reach the sheath-presheath boundary, they are accelerated across the sheath towards the electrode for Cl_2^+ and Cl^+ ions, respectively. As the ions approach the electrode, the IEDs become wider and shift from single-peak to bimodal profile since the ion transit time through the sheath is significantly less than the low-frequency period and consequently the ions respond to the instantaneous

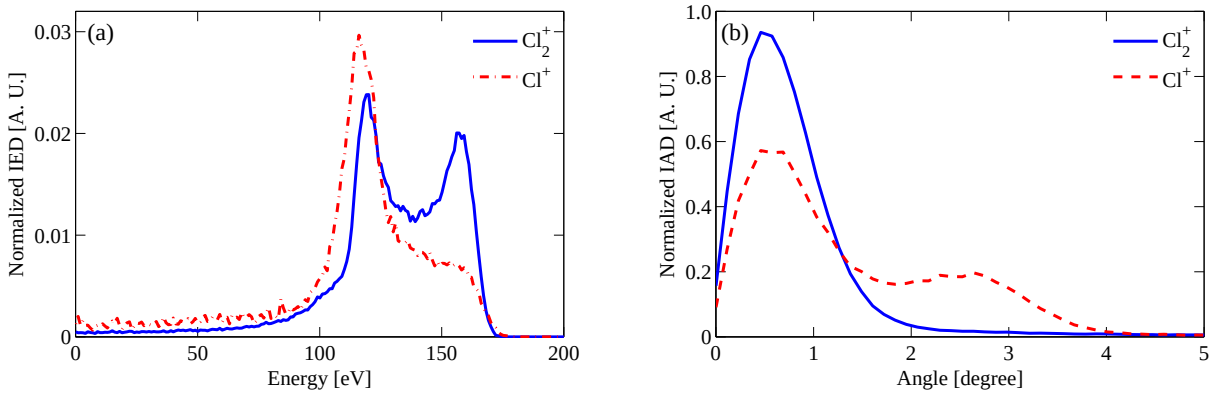

Figure 5.10: The normalized (a) IEDs and (b) IADs of Cl_2^+ and Cl^+ ions at the grounded electrode in a dual-frequency parallel-plate capacitively coupled chlorine discharge at 10 mTorr with a gap separation of 0.0254 m.

electric field. The IADs of Cl_2^+ and Cl^+ ions in figures 5.9(c) and (d) show how the ions are accumulated at small angles and the bombardment of ions is almost anisotropic at the surface, as shown in figure 5.10(b). The dominance of the low-energy peak in the IED of Cl_2^+ ions at the surface, shown in figure 5.10(a), is a result of the resistive nature and modulation effect of the sheath as demonstrated by Boyle et al. (2004). The sheath potential is at low voltage for a greater proportion of a cycle than it is at high voltage. For the IED of Cl^+ ions, however, only the low-energy peak becomes prominent as approaching the surface while the high-energy peak is very weak compared with the IED of Cl_2^+ ions. This indicates a more resistive sheath is encountered by Cl^+ ions than by Cl_2^+ ions. Moreover, figure 5.10(a) shows that the IED of Cl^+ ions at the surface has enhanced low-energy components compared with the IED of Cl_2^+ ions, which can be ascribed to charge-exchange reactions and heavy-particle collisions in the sheath region when Cl^+ ions transit it. Figure 5.10(b) shows that the IAD of Cl^+ ions at the surface has a secondary peak at about 2.7°, which is found to be caused by electron impact dissociative ionization, $e + Cl_2 \longrightarrow Cl + Cl^+ + 2e$.

Chapter 6

Conclusions and future work

6.1 Conclusions

In this study, we demonstrate a newly developed 1d-3v PIC/MCC code, oopd1, combined with a global model, for simulations of capacitively coupled chlorine discharge. Significantly revised cross section database for the collisional process in chlorine is included in this code, as well as the addition of Cl atoms, Cl^+ ions and the relevant reactions and cross sections. The agreement between the simulation results and experimentally measured data is good. Both voltage driven and current driven single-frequency capacitively coupled chlorine discharges are explored. Key parameters for the capacitively coupled chlorine discharge are explored and the effect of gas pressure, driving current, driving frequency and secondary electrons on the discharge is analyzed.

As the gas pressure is increased from 5 to 100 mTorr, the electron heating mechanism evolves from both stochastic and Ohmic heating to predominantly Ohmic heating. The electron heating outweighs the ion heating at high pressure. Also, the effective electron temperature decreases with increasing pressure in order to satisfy the particle balance. The density profile for Cl_2^+ and Cl^- ions becomes flattened in the bulk region and the electronegativity increases as the pressure

increases. The creation of Cl^+ ions in the sheath region is mainly due to non-resonant charge exchange from Cl_2^+ ions to Cl^+ ions, which is further enhanced by the increasing pressure. The creation of Cl^+ ions in the bulk region is mainly due to electron impact ionization processes. With increasing pressure, more Cl_2^+ and Cl^+ ions hit the electrode under large angles, which can heavily affect the etching process at the surface. With the increasing driving current, the EEPF shows a transition from a Druyvesteyn like to a Maxwellian like and then to a bi-Maxwellian profile, which is mainly caused by the enhanced stochastic heating in the sheath region and diminished Ohmic heating in the bulk region. As the driving frequency increases at fixed absorbed power, the displacement current increases and a lower rf voltage is required to keep the power invariant. Thus, the average sheath potential decreases, such that the IEDs of Cl_2^+ and Cl^+ ions shift to the low-energy region and the IADs of Cl_2^+ and Cl^+ ions extend to large angles. The effect of the secondary electron emission on the discharge can be witnessed mainly from the variations of the electron heating rate and the EEPF. The IEDs, IADs and neutral energy distributions show little dependence on the secondary electron emission.

Moreover, we extend our study to dual-frequency capacitively coupled chlorine discharge by adding a low-frequency current source and explore the effect of the low-frequency source on the discharge. The flux of Cl_2^+ ions to the surface increases only slightly while the average energy of Cl_2^+ ions to the surface increases almost linearly with increasing low-frequency current. This shows that it is possible to independently control the flux and energy of Cl_2^+ ions by varying the low-frequency current in a dual-frequency capacitively coupled chlorine discharge. However, the increase of the flux of Cl^+ ions with increasing low-frequency current, which is mainly due to the increased dissociation fraction of the background gas caused by extra power supplied by the low-frequency source, is undesirable.

The effect of the secondary electron emission on the discharge is found to be intensified in the dual-frequency discharge compared to the single-frequency discharge. With the addition of a low-frequency source, the ions begin to respond to the instantaneous electric field in the

sheath region, leading to bimodal profile for the IEDs of Cl_2^+ and Cl^+ ions. When transiting the sheath, the Cl^+ ions experience a more collisional sheath than the Cl_2^+ ions. The IADs of Cl_2^+ and Cl^+ ions at the surface are almost anisotropic. However, a secondary peak is found in the IAD of Cl^+ ions, which can be ascribed to dissociative ionization reactions.

6.2 Limitations

The limitations in our work mainly lie in two aspects and are stated below.

(I) The first aspect is generally due to the PIC/MCC method itself. The computational cost of the PIC/MCC simulation is relatively high compared to analytical models. The lack of data in the cross sections for the reactions is also a limitation for the PIC/MCC method. For some reactions such as recombination of positive and negative ions which can be important in chlorine discharge, we have to use rate coefficients to estimate the cross sections and this estimation is relatively crude. Besides, not all the neutrals in the discharge can be tracked as superparticles in the simulation due to the large amounts of neutrals compared with charged particles in weakly ionized plasmas. Thus, the neutrals are assumed to be the background gas in the simulation and only the high-energy neutrals are tracked in the simulation.

(II) Apart from the limitations due to the PIC/MCC method itself, the other limitation lies in the estimation of the dissociation fraction of the molecular chlorine gas. In the simulation, we need to rely on the global model calculation to estimate the density of Cl atoms in the background gas. While, global model is mainly developed for ICP rather than CCP. The proportion of the power dissipated in electron heating in ICP is much larger than in CCP. Therefore, the use of a global model will lead to overestimation of the density of Cl atoms in the discharge, especially when in the low pressure range. As the pressure decreases below 10 mTorr, most of the power is dissipated in the ion heating in the sheath region for accelerating the ions to the electrode. Meanwhile, the sheath region expands to an extent that the discharge

area is apparently divided into one bulk region and two sheath regions and the absorbed power is no loner uniformly distributed in the whole discharge area. Thus, the assumption in the global model that the power is uniformly distributed in the discharge area is invalid and the accuracy of the global model calculation cannot be guaranteed.

6.3 Future work

In this study, we primarily investigated the single-frequency capacitively coupled chlorine discharge. Only the effect of adding a low-frequency current on the discharge is explored. However, problems including the effect of the driving low frequency and the effect of the high-frequency source on dual-frequency capacitively coupled chlorine discharge have not been explored and the interaction between the high- and low-frequency sources still remains to be investigated and comprehended. Future work will probably be focused on the effect of high- and low-frequency sources (e.g., the driving current and frequency) on dual-frequency capacitively coupled chlorine discharge and explore the interaction between the two sources.

Appendix A

Symbols and abbreviations

Symbols

e	electron charge (1.602×10^{-19} C)
f	driving frequency (Hz)
i	integer
j	integer
k	rate coefficient (m^3/s)
m	mass (kg)
n	density (m^{-3})
p	gas pressure (Pa)
q	electric charge (C)
$\overline{s}_\mathrm{m}$	average sheath thickness (m)
t	time (s)
$\boldsymbol{v}$	velocity (m/s)
$\boldsymbol{x}$	displacement (m)
$\boldsymbol{B}$	magnetic induction (T)
$\boldsymbol{E}$	electric field (V/m)

$\boldsymbol{F}$	force (N)
J	current density (A/m^2)
M	mass (kg)
N	integer
P	fraction
P_{abs}	absorbed power (W)
R	random number ($0 \leq R \leq 1$)
$\mathrm{T_{eff}}$	effective electron temperature (eV)
T_{g}	gas temperature (K)
V	voltage (V)
$\overline{V}_{\mathrm{s}}$	average sheath potential (V)
α_0	electronegativity
γ_{se}	secondary electron emission coefficient
λ_{De}	electron Debye length (m)
ν	collision frequency (s^{-1})
ρ	charge density (C/m^2)
σ	cross section (m^2)
τ_{ion}	ion transit time (s)
τ_{rf}	rf period (s)
ω	radian frequency (rad/s)
ω_{pe}	electron plasma frequency (rad/s)
Δt	time step (t)
Δx	grid spacing (m)
ΔE_{i}	width of IED (eV)
$\mathcal{E}$	kinetic energy (eV)

Abbreviations

1d-3v	one dimension in spatial space and three velocity components in phase space
hf	high-frequency
lf	low-frequency
oopd1	object oriented plasma device for one dimension
rf	radio frequency
CCP	capacitively coupled plasma
CMF	center of mass frame
DF	dual-frequency
DSMC	direct simulation Monte Carlo
ECR	electron cyclotron resonance
EEDF	electron energy distribution function
EEPF	electron energy probability function
GEC	Gaseous Electronics Conference
IAD	ion angular distribution
ICP	inductively coupled plasma
IED	ion energy distribution
NAD	neutral angular distribution
NED	neutral energy distribution
PIC/DMC	particle-in-cell/dynamic Monte Carlo
PIC/MCC	particle-in-cell/Monte Carlo collision
SF	single-frequency
TRF	target rest frame

Bibliography

Abdel-Fattah, E. and H. Sugai (2003). Influence of excitation frequency on the electron distribution function in capacitively coupled discharges in argon and helium. *Japanese Journal of Applied Physics 42*(Part 1, No. 10), 6569–6577.

Ahn, S. K. and H. Y. Chang (2009). Role of low-frequency power in dual-frequency capacitive discharges. *Applied Physics Letters 95*(11), 111502.

Ali, M. A. and Y.-K. Kim (2005). Total ionization cross sections of Cl and Cl_2 by electron impact. *Surface and Interface Analysis 37*(11), 969–972.

Amanatides, E. and D. Mataras (2001). Frequency variation under constant power conditions in hydrogen radio frequency discharges. *Journal of Applied Physics 89*(3), 1556–1566.

Aydil, E. S. and D. J. Economou (1991). Multiple steady states in a radio frequency chlorine glow discharge. *Journal of Applied Physics 69*(1), 109–114.

Aydil, E. S. and D. J. Economou (1992a). Theoretical and experimental investigations of chlorine RF glow discharges I. Theoretical. *Journal of The Electrochemical Society 139*(5), 1396–1406.

Aydil, E. S. and D. J. Economou (1992b). Theoretical and experimental investigations of chlorine RF glow discharges II. Experimental. *Journal of The Electrochemical Society 139*(5), 1406–1412.

Aydil, E. S. and D. J. Economou (1993). Modeling of plasma etching reactors including wafer heating effects. *Journal of The Electrochemical Society 140*(5), 1471–1481.

Basner, R. and K. Becker (2004). Experimental absolute electron impact ionization cross-sections of Cl_2. *New Journal of Physics 6*(1), 118.

Benoit-Cattin, P. and L.-C. Bernard (1968). Anomalies of the energy of positive ions extracted from high-frequency ion sources. A theoretical study. *Journal of Applied Physics 39*(12), 5723–5726.

Bera, K., S. Rauf, and K. Collins (2011). PIC-MCC/Fluid hybrid model for low pressure capacitively coupled O_2 plasma. *AIP Conference Proceedings 1333*(1), 1027–1032.

Bi, Z., Y. Liu, W. Jiang, X. Xu, and Y. Wang (2011). A brief review of dual-frequency capacitively coupled discharges. *Current Applied Physics 11*(5, Supplement), S2–S8.

Bi, Z.-H., Z.-L. Dai, X. Xu, Z.-C. Li, and Y.-N. Wang (2009). Numerical results for the Ar and CF_4 mixture gas in a dual frequency capacitively coupled plasma using a hybrid model. *Physics of Plasmas 16*(4), 043510.

Birdsall, C. K. (1991). Particle-in-cell charged-particle simulations, plus Monte Carlo collisions with neutral atoms, PIC-MCC. *IEEE Transactions on Plasma Science 19*(2), 65–85.

Bodart, P., G. Cunge, O. Joubert, and T. Lill (2012). $SiCl_4/Cl_2$ plasmas: A new chemistry to etch high-k materials selectively to Si-based materials. *Journal of Vacuum Science and Technology A 30*(2), 020602.

Böhm, C. and J. Perrin (1993). Retarding-field analyzer for measurements of ion energy distributions and secondary electron emission coefficients in low-pressure radio frequency discharges. *Review of Scientific Instruments 64*(1), 31–44.

Booth, J. P., Y. Azamoum, N. Sirse, and P. Chabert (2012). Absolute atomic chlorine densities in a Cl_2 inductively coupled plasma determined by two-photon laser-induced fluorescence with a new calibration method. *Journal of Physics D: Applied Physics 45*(19), 195201.

Booth, J. P., G. Curley, D. Marić, and P. Chabert (2010). Dual-frequency capacitive radiofrequency discharges: effect of low-frequency power on electron density and ion flux. *Plasma Sources Science and Technology 19*(1), 015005.

Bose, A. F. (1995). *Diagnostics and Control of Plasma Etching Reactors for Semiconductor Manufacturing*. Ph.D. thesis, Swiss Federal Institute of Technology, Zurich.

Bose, F., R. Patrick, and H. P. Baltes (1994). Characterization of plasma etch processes using measurements of discharge impedance. *Journal of Vacuum Science and Technology B 12*(4), 2805–2809.

Boyle, P. C., A. R. Ellingboe, and M. M. Turner (2004). Electrostatic modelling of dual frequency rf plasma discharges. *Plasma Sources Science and Technology 13*(3), 493–503.

Brunetti, B., G. Liuti, E. Luzzatti, F. Pirani, and F. Vecchiocattivi (1981). Study of the interactions of atomic and molecular oxygen with O_2 and N_2 by scattering data. *Journal of Chemical Physics 74*(12), 6734–6741.

Calandra, P., C. S. S. O'Connor, and S. D. Price (2000). Electron-impact ionization of the chlorine molecule. *Journal of Chemical Physics 112*(24), 10821–10830.

Chang, J. P. and H. H. Sawin (1997). Kinetic study of low energy ion-enhanced polysilicon etching using Cl, Cl_2, and Cl^+ beam scattering. *Journal of Vacuum Science and Technology A 15*(3), 610–615.

Chanson, R., A. Rhallabi, M. C. Fernandez, C. Cardinaud, S. Bouchoule, L. Gatilova, and A. Talneau (2012). Global model of Cl_2/Ar high-density plasma discharge and 2-D Monte-Carlo etching model of InP. *IEEE Transactions on Plasma Science 40*(4), 959–971.

Christophorou, L. G. and J. K. Olthoff (1999). Electron interactions with Cl_2. *Journal of Physical and Chemical Reference Data 28*(1), 131–169.

Chung, T. H., L. Meng, H. J. Yoon, and J. K. Lee (1997). Two-dimensional fluid simulation of capacitively coupled RF electronegative plasmas. *Japanese Journal of Applied Physics 36*(Part 1, No. 5A), 2874–2882.

Church, M. J. and D. Smith (1978). Ionic recombination of atomic and molecular ions in flowing afterglow plasmas. *Journal of Physics D: Applied Physics 11*(16), 2199–2206.

Coburn, J. W. and H. F. Winters (1979). Ion- and electron-assisted gas-surface chemistry—An important effect in plasma etching. *Journal of Applied Physics 50*(5), 3189–3196.

Cramer, W. H. (1959). Elastic and inelastic scattering of low-velocity ions: Ne^+ in A, A^+ in Ne, and A^+ in A. *Journal of Chemical Physics 30*(3), 641–642.

Diomede, P., M. Capitelli, and S. Longo (2005). Effect of discharge voltage on capacitively coupled, parallel plate rf hydrogen plasmas. *Plasma Sources Science and Technology 14*(3), 459–466.

Donkó, Z. and Z. L. Petrović (2006). Analysis of a capacitively coupled dual-frequency CF_4 discharge. *Japanese Journal of Applied Physics 45*(10B), 8151–8156.

Donnelly, V. M., D. L. Flamm, and R. H. Bruce (1985). Effects of frequency on optical emission, electrical, ion, and etching characteristics of a radio frequency chlorine plasma. *Journal of Applied Physics 58*(6), 2135–2144.

Donnelly, V. M., D. L. Flamm, and G. Collins (1982). Laser diagnostics of plasma etching: Measurement of Cl_2^+ in a chlorine discharge. *Journal of Vacuum Science and Technology 21*(3), 817–823.

Donnelly, V. M. and A. Kornblit (2013). Plasma etching: Yesterday, today, and tomorrow. *Journal of Vacuum Science and Technology A 31*(5), 050825.

Donnelly, V. M. and M. V. Malyshev (2000). Diagnostics of inductively coupled chlorine plasmas: Measurements of the neutral gas temperature. *Applied Physics Letters 77*(16), 2467–2469.

Flamm, D. L. (1990). Mechanisms of silicon etching in fluorine- and chlorine-containing plasmas. *Pure and Applied Chemistry 62*(9), 1709–1720.

Flamm, D. L. and V. M. Donnelly (1981). The design of plasma etchants. *Plasma Chemistry and Plasma Processing 1*(4), 317–363.

Flamm, D. L. and V. M. Donnelly (1986). Time-dependent excitation in high- and low-frequency chlorine plasmas. *Journal of Applied Physics 59*(4), 1052–1062.

Franklin, R. N. and J. Snell (2000). The Boltzmann relation in electronegative plasmas: When is it permissible to use it? *Journal of Plasma Physics 64*(2), 131–153.

Franz, G. (2005). Comprehensive analysis of chlorine-containing capacitively coupled plasmas. *Journal of Vacuum Science and Technology A 23*(3), 369–387.

Franz, G. (2006). Some aspects of dissipation mechanisms in chlorine containing capacitively coupled discharges. *Journal of Vacuum Science and Technology A 24*(4), 1360–1365.

Franz, G. and M. Klick (2005). Electron heating in capacitively coupled discharges and reactive gases. *Journal of Vacuum Science and Technology A 23*(4), 917–921.

Fritioff, K., J. Sandström, D. Hanstorp, A. Ehlerding, M. Larsson, G. F. Collins, D. J. Pegg, H. Danared, A. Källberg, and A. L. Padellec (2003). Electron-impact detachment from Cl^-. *Physical Review A 68*(1), 012712.

Ganas, P. S. (1988). Electron impact excitation cross sections for chlorine. *Journal of Applied Physics 63*(2), 277–279.

Gans, T., J. Schulze, D. O'Connell, U. Czarnetzki, R. Faulkner, A. R. Ellingboe, and M. M. Turner (2006). Frequency coupling in dual frequency capacitively coupled radio-frequency plasmas. *Applied Physics Letters 89*(26), 261502.

Georgieva, V., A. Bogaerts, and R. Gijbels (2003). Numerical study of $Ar/CF_4/N_2$ discharges in single- and dual-frequency capacitively coupled plasma reactors. *Journal of Applied Physics 94*(6), 3748–3756.

Georgieva, V., A. Bogaerts, and R. Gijbels (2004). Numerical investigation of ion-energy-distribution functions in single and dual frequency capacitively coupled plasma reactors. *Physical Review E 69*(2), 026406.

Godyak, V. A., R. B. Piejak, and B. M. Alexandrovich (1992). Evolution of the electron-energy-distribution function during rf discharge transition to the high-voltage mode. *Physical Review Letters 68*(1), 40–43.

Golovitskii, A. P. (2000). Temperature dependence of an electron attachment to chlorine molecules. *Technical Physics 45*(5), 532–537.

Gote, M. and H. Ehrhardt (1995). Rotational excitation of diatomic molecules at intermediate energies: absolute differential state-to-state transition cross sections for electron scattering from N_2, Cl_2, CO and HCl. *Journal of Physics B: Atomic, Molecular and Optical Physics 28*(17), 3957–3986.

Goto, H. H., H.-D. Löwe, and T. Ohmi (1992). Dual excitation reactive ion etcher for low energy plasma processing. *Journal of Vacuum Science and Technology A 10*(5), 3048–3054.

Goto, H. H., H.-D. Löwe, and T. Ohmi (1993). Independent control of ion density and ion bombardment energy in a dual RF excitation plasma. *IEEE Transactions on Semiconductor Manufacturing 6*(1), 58–64.

Gottscho, R. A. and C. E. Gaebe (1986). Negative ion kinetics in RF glow discharges. *IEEE Transactions on Plasma Science 14*(2), 92–102.

Gregório, J. and L. C. Pitchford (2012). Updated compilation of electron-Cl_2 scattering cross sections. *Plasma Sources Science and Technology 21*(3), 032002.

Gudmundsson, J. T. (2001). On the effect of the electron energy distribution on the plasma parameters of an argon discharge: a global (volume-averaged) model study. *Plasma Sources Science and Technology 10*(1), 76–81.

Gudmundsson, J. T., A. T. Hjartarson, and E. G. Thorsteinsson (2012). The influence of the electron energy distribution on the low pressure chlorine discharge. *Vacuum 86*(7), 808–812.

Gudmundsson, J. T., E. Kawamura, and M. A. Lieberman (2013). A benchmark study of a capacitively coupled oxygen discharge of the oopd1 particle-in-cell Monte Carlo code. *Plasma Sources Science and Technology 22*(3), 035011.

Hammel, J. and J. P. Verboncoeur (2003). DC discharge studies using PIC-MCC. *Bulletin of the American Physical Society 48*(6), 66.

Hargis, P. J., K. E. Greenberg, P. A. Miller, J. B. Gerardo, J. R. Torczynski, M. E. Riley, G. A. Hebner, J. R. Roberts, J. K. Olthoff, J. R. Whetstone, R. J. V. Brunt, M. A. Sobolewski, H. M. Anderson, M. P. Splichal, J. L. Mock, P. Bletzinger, A. Garscadden, R. A. Gottscho, G. Selwyn, M. Dalvie, J. E. Heidenreich, J. W. Butterbaugh, M. L. Brake, M. L. Passow, J. Pender, A. Lujan, M. E. Elta, D. B. Graves, H. H. Sawin, M. J. Kushner, J. T. Verdeyen, R. Horwath, and T. R. Turner (1994). The Gaseous Electronics Conference radio-frequency reference cell: A defined parallel-plate radio-frequency system for experimental and theoretical studies of plasma-processing discharges. *Review of Scientific Instruments 65*(1), 140–154.

Hayes, T. R., R. C. Wetzel, and R. S. Freund (1987). Absolute electron-impact-ionization cross-section measurements of the halogen atoms. *Physical Review A 35*(2), 578–584.

Huang, S. and J. T. Gudmundsson (2013). A particle-in-cell/Monte Carlo simulation of a capacitively coupled chlorine discharge. *Plasma Sources Science and Technology 22*(5), 055020.

Huang, S. and J. T. Gudmundsson (2014a). A current driven capacitively coupled chlorine discharge. *Plasma Sources Science and Technology*. Accepted.

Huang, S. and J. T. Gudmundsson (2014b). Current driven dual frequency capacitively coupled discharge in chlorine. In *The XXII Europhysics Conference on Atomic and Molecular Physics of Ionized Gases*, Greifswald, Germany, July 15-19. Submitted.

Huang, S. and J. T. Gudmundsson (2014c). Ion energy and angular distributions in a dual-frequency capacitively coupled chlorine discharge. *IEEE Transactions on Plasma Science*. Submitted.

Huq, M. S., D. Scott, N. R. White, R. L. Champion, and L. D. Doverspike (1984). Measurements of absolute total cross sections for charge transfer and electron detachment of halide ions on chlorine. *Journal of Chemical Physics 80*(8), 3651–3655.

Joy, D. C. (1995). A database on electron-solid interactions. *Scanning 17*(5), 270–275. Data available: `http://web.utk.edu/~srcutk/htm/interact.htm`.

Karmohapatro, S. B. (1965). Charge exchange of Cl^- ions with atomic chlorine. *Journal of the Physical Society of Japan 20*(5), 839–841.

Kawamura, E., C. K. Birdsall, and V. Vahedi (2000). Physical and numerical methods of speeding up particle codes and paralleling as applied to RF discharges. *Plasma Sources Science and Technology 9*(3), 413–428.

Kawamura, E., M. A. Lieberman, and A. J. Lichtenberg (2006). Stochastic heating in single and dual frequency capacitive discharges. *Physics of Plasmas 13*(5), 053506.

Kawamura, E., V. Vahedi, M. A. Lieberman, and C. K. Birdsall (1999). Ion energy distributions in rf sheaths; review, analysis and simulation. *Plasma Sources Science and Technology 8*(3), R45–R64.

Kawano, S., K. Nanbu, and J. Kageyama (2000). Systematic simulations of plasma structures in chlorine radio frequency discharges. *Journal of Physics D: Applied Physics 33*(20), 2637–2646.

Kim, G.-H., A. M. Efremov, D.-P. Kim, and C.-I. Kim (2005). Inductively coupled Cl_2/N_2 plasma: Experimental investigation and modeling. *Microelectronic Engineering 81*(1), 96–105.

Kim, H. C. and J. K. Lee (2004). Mode transition induced by low-frequency current in dual-frequency capacitive discharges. *Physical Review Letters 93*(8), 085003.

Kim, H. C. and J. K. Lee (2005a). Dual-frequency capacitive discharges: Effect of low-frequency current on electron distribution function. *Physics of Plasmas 12*(5), 053501.

Kim, H. C. and J. K. Lee (2005b). Dual radio-frequency discharges: Effective frequency concept and effective frequency transition. *Journal of Vacuum Science and Technology A 23*(4), 651–657.

Kolorenč, P. and J. Horáček (2006). Dissociative electron attachment and vibrational excitation of the chlorine molecule. *Physical Review A 74*(6), 062703.

Kota, G. P., J. W. Coburn, and D. B. Graves (1998). The recombination of chlorine atoms at surfaces. *Journal of Vacuum Science and Technology A 16*(1), 270–277.

Kramer, J. (1986). The optogalvanic effect in a 13.56-MHz chlorine discharge. *Journal of Applied Physics 60*(9), 3072–3080.

Kratzer, M., R. P. Brinkmann, W. Sabisch, and H. Schmidt (2001). Hybrid model for the calculation of ion distribution functions behind a direct current or radio frequency driven plasma boundary sheath. *Journal of Applied Physics 90*(5), 2169–2179.

Küllig, C., K. Dittmann, T. Wegner, I. Sheykin, K. Matyash, D. Loffhagen, R. Schneider, and J. Meichsner (2012). Dynamics and electronegativity of oxygen rf plasmas. *Contributions to Plasma Physics 52*(10), 836–846.

Kurepa, M. V. and D. S. Belić (1978). Electron-chlorine molecule total ionisation and electron attachment cross sections. *Journal of Physics B: Atomic and Molecular Physics 11*(21), 3719–3729.

Kushner, M. J. (1985). Distribution of ion energies incident on electrodes in capacitively coupled rf discharges. *Journal of Applied Physics 58*(11), 4024–4031.

Kutz, H. and H.-D. Meyer (1995). Rotational excitation of N_2 and Cl_2 molecules by electron impact in the energy range 0.01–1000 eV: Investigation of excitation mechanisms. *Physical Review A 51*(5), 3819–3830.

Lafleur, T., P. Chabert, and J. P. Booth (2013). Secondary electron induced asymmetry in capacitively coupled plasmas. *Journal of Physics D: Applied Physics 46*(13), 135201.

Lee, C. and M. A. Lieberman (1995). Global model of Ar, O_2, Cl_2, and Ar/O_2 high-density plasma discharges. *Journal of Vacuum Science and Technology A 13*(2), 368–380.

Lee, J. K., N. Y. Babaeva, H. C. Kim, O. V. Manuilenko, and J. W. Shon (2004). Simulation of capacitively coupled single- and dual-frequency RF discharges. *IEEE Transactions on Plasma Science 32*(1), 47–53.

Lee, Y. T., M. A. Lieberman, A. J. Lichtenberg, F. Bose, H. Baltes, and R. Patrick (1997). Global model for high pressure electronegative radio-frequency discharges. *Journal of Vacuum Science and Technology A 15*(1), 113–126.

Levinson, J. A., E. S. G. Shaqfeh, M. Balooch, and A. V. Hamza (1997). Ion-assisted etching and profile development of silicon in molecular chlorine. *Journal of Vacuum Science and Technology A 15*(4), 1902–1912.

Lichtenberg, A. J., I. G. Kouznetsov, Y. T. Lee, M. A. Lieberman, I. D. Kaganovich, and L. D. Tsendin (1997). Modelling plasma discharges at high electronegativity. *Plasma Sources Science and Technology 6*(3), 437–449.

Lichtenberg, A. J., V. Vahedi, M. A. Lieberman, and T. Rognlien (1994). Modeling electronegative plasma discharges. *Journal of Applied Physics 75*(5), 2339–2347.

Lieberman, M. A. and A. J. Lichtenberg (2005). *Principles of Plasma Discharges and Materials Processing* (2nd ed.). Hoboken, New Jersey: John Wiley & Sons, Inc.

Lieberman, M. A. and A. J. Lichtenberg (2010). Electron heating of voltage-driven and matched dual frequency discharges. *Plasma Sources Science and Technology 19*(6), 065006.

Lim, C.-H. (2007). *The interaction of energetic charged particles with gas and boundaries in the particle simulation of plasmas.* Ph.D. thesis, University of California, Berkeley.

Lisovskiy, V. A. and Y. D. Yegorenkov (2006). Double layer onset inside the near-electrode sheath of a RF capacitive discharge in oxygen. *Vacuum 80*(5), 458–467.

Longo, S. (2006). Monte Carlo simulation of charged species kinetics in weakly ionized gases. *Plasma Sources Science and Technology 15*(4), S181–S188.

Lymberopoulos, D. P. and D. J. Economou (1994). Modeling and simulation of glow discharge plasma reactors. *Journal of Vacuum Science and Technology A 12*(4), 1229–1236.

Lymberopoulos, D. P. and D. J. Economou (1995). Spatiotemporal electron dynamics in radio-frequency glow discharges: fluid versus dynamic Monte Carlo simulations. *Journal of Physics D: Applied Physics 28*(4), 727–737.

Malyshev, M. V. and V. M. Donnelly (2000). Diagnostics of inductively coupled chlorine plasmas: Measurement of Cl_2 and Cl number densities. *Journal of Applied Physics 88*(11), 6207–6215.

Manenschijn, A. and W. J. Goedheer (1991). Angular ion and neutral energy distribution in a collisional rf sheath. *Journal of Applied Physics 69*(5), 2923–2930.

Meyyappan, M. and T. R. Govindan (1991). Modeling of electronegative radio-frequency discharges. *IEEE Transactions on Plasma Science 19*(2), 122–129.

Moran, T. F. and J. R. Roberts (1968). Collision-induced dissociation of low-kinetic-energy ions. *Journal of Chemical Physics 49*(8), 3411–3421.

Muschlitz, E. E. (1959). Elastic and inelastic collisions of low-energy negative ions in gases. In *Proceedings of the Fourth International Conference on Ionization Phenomena in Gases*, Uppsala, Sweden, August 17-21, pp. 52–56.

Nanbu, K., T. Nakagome, and J. Kageyama (1999). Detailed structure of the afterglow of radio-frequency chlorine discharge. *Japanese Journal of Applied Physics 38*(Part 2, No. 8B), L951–L953.

Nanbu, K., M. Suetani, and H. Sasaki (1999). Direct simulation Monte Carlo (DSMC) modeling of silicon etching in radio-frequency chlorine discharge. *Computational Fluid Dynamics Journal 8*(2), 257–265.

Nguyen, C. (2006). PIC-Monte Carlo collision scheme for the modeling of hydrocarbon transport at the fusion edge. Master's thesis, University of California, Berkeley.

Novikova, T., B. Kalache, P. Bulkin, K. Hassouni, W. Morscheidt, and P. Roca i Cabarrocas (2003). Numerical modeling of capacitively coupled hydrogen plasmas: Effects of frequency and pressure. *Journal of Applied Physics 93*(6), 3198–3206.

O'Connell, D. (2004). *Investigations of high voltage plasma boundary sheaths in radio-frequency discharges operated with multiple frequencies.* Ph.D. thesis, Dublin City University, Ireland.

O'Connell, D., R. Zorat, A. R. Ellingboe, and M. M. Turner (2007). Comparison of measurements and particle-in-cell simulations of ion energy distribution functions in a capacitively coupled radio-frequency discharge. *Physics of Plasmas 14*(10), 103510.

Oh, Y.-H., N.-H. Choi, and D.-I. Choi (1990). A numerical simulation of rf glow discharge containing an electronegative gas composition. *Journal of Applied Physics 67*(7), 3264–3268.

Ohtsu, Y. and H. Fujita (2004). Production of high-density capacitively coupled radio-frequency discharge plasma by high-secondary-electron-emission oxide. *Applied Physics Letters 85*(21), 4875–4877.

Olthoff, J. K. and K. E. Greenberg (1995). The Gaseous Electronics Conference RF reference cell–An introduction. *Journal of Research of the National Institute of Standards and Technology 100*(4), 327–339.

Ono, K., T. Oomori, and M. Hanazaki (1990). Plasma chemical view of magnetron and reactive ion etching of Si with Cl_2. *Japanese Journal of Applied Physics 29*(10), 2229–2235.

Ono, K., T. Oomori, M. Tuda, and K. Namba (1992). Measurements of the Cl atom concentration in radio-frequency and microwave plasmas by two-photon laser-induced fluorescence: Relation to the etching of Si. *Journal of Vacuum Science and Technology A 10*(4), 1071–1079.

Panarese, A., P. Diomede, and S. Longo (2013). Kinetic modelling of atom production and thermalization in CCRF discharges in H_2. *Plasma Sources Science and Technology 22*(4), 045017.

Park, S.-K. and D. J. Economou (1990). Analysis of low pressure rf glow discharges using a continuum model. *Journal of Applied Physics 68*(8), 3904–3915.

Peyerimhoff, S. D. and R. J. Buenker (1981). Electronically excited and ionized states of the chlorine molecule. *Chemical Physics 57*(3), 279–296.

Phelps, A. V. and Z. L. Petrović (1999). Cold-cathode discharges and breakdown in argon: surface and gas phase production of secondary electrons. *Plasma Sources Science and Technology 8*(3), R21–R44.

Rauf, S. and M. J. Kushner (1999). Nonlinear dynamics of radio frequency plasma processing reactors powered by multifrequency sources. *IEEE Transactions on Plasma Science 27*(5), 1329–1338.

Rescigno, T. N. (1994). Low-energy electron-collision processes in molecular chlorine. *Physical Review A 50*(2), 1382–1389.

Roberto, M., J. Verboncoeur, P. Verdonck, and E. Cizzoto (2006). Effects of the secondary electron emision coefficent on the generation of charged particles in RF oxygen discharge. *ECS Transactions 4*(1), 563–571.

Rogoff, G. L. (1985). Ambipolar diffusion coefficients for discharges in attaching gases. *Journal of Physics D: Applied Physics 18*(8), 1533–1545.

Rogoff, G. L., J. M. Kramer, and R. B. Piejak (1986). A model for the bulk plasma in an RF chlorne discharge. *IEEE Transactions on Plasma Science 14*(2), 103–111.

Ruf, M.-W., S. Barsotti, M. Braun, H. Hotop, and I. I. Fabrikant (2004). Dissociative attachment and vibrational excitation in low-energy electron collisions with chlorine molecules. *Journal of Physics B: Atomic, Molecular and Optical Physics 37*(1), 41–62.

Sahni, O. and C. Lanza (1976). Importance of the dependence of the secondary electron emission coefficient on E/p_0 for Paschen breakdown curves in ac plasma panels. *Journal of Applied Physics 47*(4), 1337–1340.

Schwarzenbach, W., A. A. Howling, M. Fivaz, S. Brunner, and C. Hollenstein (1996). Sheath impedance effects in very high frequency plasma experiments. *Journal of Vacuum Science and Technology A 14*(1), 132–138.

Segawa, S., M. Kurihara, N. Nakano, and T. Makabe (1999). Dependence of driving frequency on capacitively coupled plasma in CF_4. *Japanese Journal of Applied Physics 38*(Part 1, No. 7B), 4416–4422.

Sharma, S. and M. M. Turner (2013). Critical evaluation of analytical models for stochastic heating in dual-frequency capacitive discharges. *Journal of Physics D: Applied Physics 46*(28), 285203.

Shin, H., W. Zhu, L. Liu, S. Sridhar, V. M. Donnelly, D. J. Economou, C. Lenox, and T. Lii (2013). Selective etching of TiN over TaN and vice versa in chlorine-containing plasmas. *Journal of Vacuum Science and Technology A 31*(3), 031305.

Stebbings, R. F., A. C. H. Smith, and H. B. Gilbody (1963). Charge transfer between some atmospheric ions and atomic oxygen. *Journal of Chemical Physics 38*(9), 2280–2284.

Subramonium, P. (2003). *Simulation of transients and transport in plasma processing reactors.* Ph.D. thesis, University of Illinois at Urbana-Champaign.

Surendra, M. and D. B. Graves (1991a). Electron acoustic waves in capacitively coupled, low-pressure rf glow discharges. *Physical Review Letters 66*(11), 1469–1472.

Surendra, M. and D. B. Graves (1991b). Particle simulations of radio-frequency glow discharges. *IEEE Transactions on Plasma Science 19*(2), 144–157.

Surendra, M., D. B. Graves, and I. J. Morey (1990). Electron heating in low-pressure rf glow discharges. *Applied Physics Letters 56*(11), 1022–1024.

Thorsteinsson, E. G. and J. T. Gudmundsson (2010a). A global (volume averaged) model of a chlorine discharge. *Plasma Sources Science and Technology 19*(1), 015001.

Thorsteinsson, E. G. and J. T. Gudmundsson (2010b). The low pressure Cl_2/O_2 discharge and the role of ClO. *Plasma Sources Science and Technology 19*(5), 055008.

Tong, L. Z. and K. Nanbu (2006). Numerical study of dual-frequency capacitively-coupled discharges in electronegative SF_6. *Europhysics Letters 75*(1), 63–69.

Turner, M. M. (2009). Collisionless heating in radio-frequency discharges: a review. *Journal of Physics D: Applied Physics 42*(19), 194008.

Turner, M. M. and P. Chabert (2006). Collisionless heating in capacitive discharges enhanced by dual-frequency excitation. *Physical Review Letters 96*(20), 205001.

Turner, M. M. and P. Chabert (2007a). Electron heating mechanisms in dual-frequency capacitive discharges. *Plasma Sources Science and Technology 16*(2), 364–371.

Turner, M. M. and P. Chabert (2007b). Modelling of dual-frequency capacitive discharges. *Computer Physics Communications 177*(1–2), 88–92.

Vahedi, V. (1993). *Modeling and simulation of RF discharges used for plasma processing*. Ph.D. thesis, University of California, Berkeley.

Vahedi, V., C. K. Birdsall, M. A. Lieberman, G. DiPeso, and T. D. Rognlien (1993). Capacitive RF discharges modelled by particle-in-cell Monte Carlo simulation. II: comparisons with laboratory measurements of electron energy distribution functions. *Plasma Sources Science and Technology 2*(4), 273–278.

Vahedi, V., G. DiPeso, C. K. Birdsall, M. A. Lieberman, and T. D. Rognlien (1993). Capacitive RF discharges modelled by particle-in-cell Monte Carlo simulation. I: analysis of numerical techniques. *Plasma Sources Science and Technology 2*(4), 261–272.

Vahedi, V. and M. Surendra (1995). A Monte Carlo collision model for the particle-in-cell method: applications to argon and oxygen discharges. *Computer Physics Communications 87*(1–2), 179–198.

Verboncoeur, J. P., M. V. Alves, V. Vahedi, and C. K. Birdsall (1993). Simultaneous potential and circuit solution for 1D bounded plasma particle simulation codes. *Journal of Computational Physics 104*(2), 321–328.

Verboncoeur, J. P., A. B. Langdon, and N. T. Gladd (1995). An object-oriented electromagnetic PIC code. *Computer Physics Communications 87*(1–2), 199–211.

Vitale, S. A., H. Chae, and H. H. Sawin (2001). Silicon etching yields in F_2, Cl_2, Br_2, and HBr high density plasmas. *Journal of Vacuum Science and Technology A 19*(5), 2197–2206.

Španěl, P., M. Tichý, and D. Smith (1993). The reactions of positive and negative halogen ions with Cl_2 and Br_2. *Journal of Chemical Physics 98*(11), 8660–8666.

Wakayama, G. and K. Nanbu (2003). Study on the dual frequency capacitively coupled plasmas by the particle-in-cell/Monte Carlo method. *IEEE Transactions on Plasma Science 31*(4), 638–644.

Wang, S., X. Xu, and Y. Wang (2012). Numerical study of ion energy and angular distributions in dual-frequency capacitively coupled CF_4 plasmas. *Physics of Plasmas 19*(2), 023506.

Wang, S., X. Xu, and Y.-N. Wang (2007). Numerical investigation of ion energy distribution and ion angle distribution in a dual-frequency capacitively coupled plasma with a hybrid model. *Physics of Plasmas 14*(11), 113501.

Wang, Y. (2012). *Ion Energy Distributions in Collisionless and Collisional, Capacitive RF Sheath*. Ph.D. thesis, University of California, Berkeley.

Wang, Y., M. A. Lieberman, A. C. F. Wu, and J. P. Verboncoeur (2011). Verification of collisionless sheath model of capacitive rf discharges by particle-in-cell simulations. *Journal of Applied Physics 110*(3), 033307.

Wang, Y., O. Zatsarinny, K. Bartschat, and J.-P. Booth (2013). Fine-structure-resolved electron collisions from chlorine atoms in the $(3p^5)^2P^o_{3/2}$ and $(3p^5)^2P^o_{1/2}$ states. *Physical Review A 87*(2), 022703.

Wild, C. and P. Koidl (1991). Ion and electron dynamics in the sheath of radio-frequency glow discharges. *Journal of Applied Physics 69*(5), 2909–2922.

Wise, R. S., D. P. Lymberopoulos, and D. J. Economou (1995). A two-region model of a radiofrequency low-pressure, high-density plasma. *Plasma Sources Science and Technology 4*(3), 317–331.

Yan, M. and W. J. Goedheer (1999). A PIC-MC simulation of the effect of frequency on the characteristics of VHF SiH_4/H_2 discharges. *Plasma Sources Science and Technology 8*(3), 349–354.

Zhang, M., X. Cai, A. Larson, and A. E. Orel (2011). Theoretical study of dissociative recombination of Cl_2^+. *Physical Review A 84*(5), 052707.

Zhang, Y., M. J. Kushner, N. Moore, P. Pribyl, and W. Gekelman (2013). Space and phase resolved ion energy and angular distributions in single- and dual-frequency capacitively coupled plasmas. *Journal of Vacuum Science and Technology A 31*(6), 061311.

Zhu, X.-M., W.-C. Chen, S. Zhang, Z.-G. Guo, D.-W. Hu, and Y.-K. Pu (2007). Electron density and ion energy dependence on driving frequency in capacitively coupled argon plasmas. *Journal of Physics D: Applied Physics 40*(22), 7019–7023.